

Lithium and Sodium Insertion in Nanostructured Titanates

Experiments and Simulations

Kun Shen

Lithium and Sodium Insertion in Nanostructured Titanates

Experiments and Simulations

PROEFSCHRIFT

ter verkrijging van de graad van doctor
aan de Technische Universiteit Delft,
op gezag van de Rector Magnificus prof. ir. K. C. A. M. Luyben,
voorzitter van het College voor Promoties,
in het openbaar te verdedigen op maandag 17 november 2014 om 10:00 uur

door

Kun Shen

Master of Engineering in Materials Physics and Chemistry
Central South University, Changsha, China
geboren te Harbin, China

Dit proefschrift is goedgekeurd door de promotor:

Prof. dr. F. M. Mulder

Copromotor:

Dr. ir. M. Wagemaker

Samenstelling promotiecommissie:

Rector Magnificus,	Voorzitter
Prof. dr. F. M. Mulder	Technische Universiteit Delft, promotor
Dr. ir. M. Wagemaker	Technische Universiteit Delft, copromotor
Prof. dr. E. H. Brück	Technische Universiteit Delft
Dr. E. M. Kelder	Technische Universiteit Delft
Prof. dr. P.H.L.Notten	Technische Universiteit Eindhoven
Prof. dr. ir. J. E. ten Elshof	Universiteit Twente
Prof. dr. A. Schmidt-Ott	Technische Universiteit Delft
Prof. dr. S. J. Picken	Technische Universiteit Delft, Reservelid

Copyright©2014 by Kun Shen

All rights reserved. No part of the material protected by this copyright notice may be produced or utilized in any form or by any means, electronic or mechanical, including photocopying, recording or by any information storage and retrieval system, without written permission from the author.

Printed in The Netherlands by Ipskamp Drukkers

ISBN: 978-94-6259-437-1

To my parents and Hao

Contents

Chapter 1 Introduction	7
1.1 General introduction	7
1.2 Lithium ion batteries	8
1.3 Sodium ion battery	11
References	16
Chapter 2 Methods	19
2.1 Experimental techniques	20
2.1.1 Materials synthesis	20
2.1.2 Electrode preparation	20
2.1.3 Electrochemical tests	21
2.1.4 X-ray powder diffraction	23
2.2 DFT calculation	27
2.2.1 DFT theory	27
2.2.2 Average voltage calculation	28
2.2.3 Surface calculation	30
2.2.4 Cluster expansion	31
References	36
Part I Lithium ion insertion in TiO_2 anatase	39
Chapter 3 Impact of particle size on the non-equilibrium phase transition of lithium inserted anatase TiO_2	41
3.1 Introduction	42
3.2 Methods	43
3.3 Results and Discussion	45
3.3.1 Size effect on the equilibrium voltage	45
3.3.2 In-situ x-ray diffraction measurements	48
3.3.3 Proof of the existence of non-equilibrium transformation	57
3.3.4 Summary of the phase transformation stages	61
3.4 Conclusions	64
References	65
Chapter 4 Thermodynamic study of Li intercalation into Li_xTiO_2	69
4.1 Introduction	70
4.2 Methods	71
4.3 Result and discussion	73
4.3.1 Surface termination	73
4.3.2 Formation energy	76
4.3.3 Voltage comparison	81
4.4 Conclusions	86
References	87
Part II Sodium ion insertion in sodium titanate and TiO_2 anatase	89
Chapter 5 $\text{Na}_{2+x}\text{Ti}_6\text{O}_{13}$ as potential negative electrode material for Na-ion batteries	91
5.1 Introduction	92

5.2 Preparation and Methods	93
5.3 Result and discussion	97
5.3.1 Electrochemistry	97
5.3.2 X-ray diffraction	99
5.3.3 DFT	102
5.3.4 Discussion	106
5.4 Conclusion	109
References	110
Appendix	112
Chapter 6 Na insertion in TiO₂ anatase, bulk versus surface storage.....	117
6.1 Introduction	118
6.2 Experimental technique	120
6.3 Results and discussion.....	123
6.4 Conclusions	133
References	134
Summary	137
Samenvatting.....	141
Acknowledgements.....	147
Curriculum Vitae	151

Chapter 1

Introduction

1.1 General introduction

The energy transition is an enormous challenge confronting humanity in this century. Energy resources are the foundation of all activity of human beings, and have a very important strategic position in the development of the economy. However, the strong dependence on the consumption of fossil fuel leads to serious environmental issues and degradation. Although the large-scale application of fossil fuels has brought tremendous progress in social productivity, nowadays most countries share the view that the severe environmental pollution caused by the fossil fuel has a high price for both economy and society. In the United states, the combustion of fossil fuel results in more than 90% of the greenhouse gas emissions,¹⁻³ which is also the main cause of global warming. Combustion of fossil fuel also produces air pollutants, including sulfur dioxides and nitrogen oxides, which fall to earth as acid rain, causing severe ecological damage (e.g. soil acidification).⁴ In addition to the environmental issues, the growing scarcity of fossil fuel resources has traditionally been associated with civil unrest, such as the Middle East oil crisis in the 1970's. Nuclear energy remains one of the major choices for most countries

in tackling global energy shortage, but the nuclear safety remains cause for concern, especially after the catastrophe at Japan's Fukushima plant. Against this background, sustainable energies are providing an alternative energy supply which is appealing and of growing significance. Based on the information available now sustainable energies cannot only satisfy the future energy demand but they are also able to reduce the pollution to a minimum. Normally, more sustainable use of energy is promoted by two approaches: i) development of renewable energy technologies, replacing or reducing dependence on fossil fuel. Main renewable energy generation methods include solar energy, wind energy, geothermal energy and tidal power; ii) enhancement of energy efficiency, reducing the energy consumption and delivery losses. The intermittent nature of renewables makes that the stability of energy supply and also the efficient use of renewable electricity demand new energy technology developments including the efficient large scale storage of electricity⁵. Due o the excellent performance for storing electricity Li ion battery received extensive interest in the past decades. The attention was at first mainly in the electricity storage for mobile applications, but recently also for static energy storage.

1.2 Lithium ion batteries

The investigation on the electronic storage can be tracked back to the eighteenth century. Dutch scientist Pieter van Musschenbroek invented the "Leiden jar", which could store static electricity between electrodes on two sides of a glass jar. After that, the Lead-acid battery, the first type of recharge battery, was invented by French scientist Gaston Planté in 1859.^{6,7} During the following century, many other types of secondary rechargeable batteries had been developed, including Ni-Cd, and Nickel Metal Hydride (Ni-MH) batteries. Since the 1970s, the rapid development of science and technology has given rise to escalating demands for the performance of power supplies, getting smaller, cleaner, more efficient and sustainable. The

first real lithium ion battery was proposed Whittingham in 1976, reporting a reversible electrochemical reaction of layered titanium disulfide with lithium metal reaching a 2 Volt output potential at room temperature.^{8,9} Since then, many electrode compounds have been showing excellent reversibility upon lithium intercalation and high lithium storage densities at suitable potentials, such as graphite,^{1,3,10} layered MoO₃ bronzes,⁷ TiO₂ anatase,⁸ manganese spinels,¹¹ Fe(SO₄)₃,¹² and FePO₄.¹³ In the early 90's, the first commercial lithium ion battery was developed by Sony and Asahi Kaser.¹⁴ Ever since, thanks to its superior energy density, environmental benign character, and portability compared with other conventional rechargeable batteries, the lithium ion battery has become the most prevalent power source in most modern mobile devices, such as cell phone, digital camera, laptop etc.¹⁵

How does lithium battery work?

The Lithium ion battery is a secondary battery device, which consists of two kinds of intercalation compounds/materials, separated by a lithium ion conducting electrolyte. The operating principle is presented in figure 1.1. During discharge the difference in chemical potential for lithium between the negative and positive electrode drives the Li-ions from the negative electrode through the electrolyte to intercalate in the positive electrode. To ensure electric neutrality, the same amount of electrons compensating the Li-ion charges has to be transported through the external circuit because the electrolyte is electronically insulating.

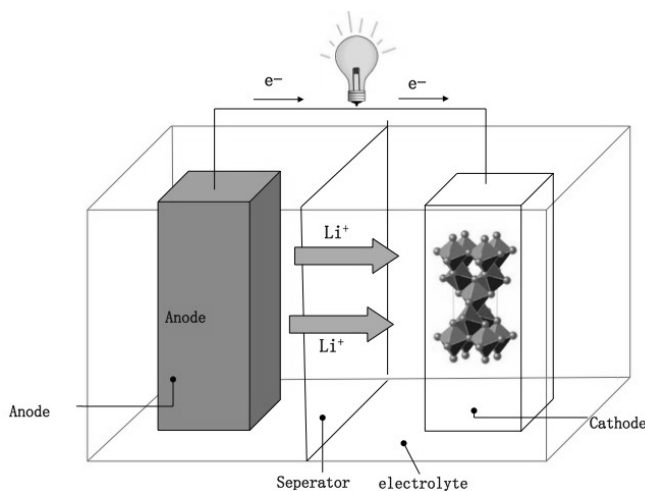


Figure 1.1 schematic picture of lithium ion battery discharge

The Li ion battery is one of the most important breakthroughs in energy storage in the last century, exhibiting many superior features compared with other secondary battery technologies (including Ni-Cd battery, Lead-acid battery etc.). The most striking advantage is the high energy density, which is closely linked to the chemical reaction in both electrodes.¹⁶ This feature makes Li ion batteries suitable to power small and mobile electric devices, up to date occupying more than a 60% share of the portable batteries market¹⁶.

However, mobile devices and (hybrid) electrical-vehicles demand increasing charge/discharge rates and energy densities, with the additional demands of high safety, long cycle life and low material costs. The charge/discharge rate is determined by the intrinsic diffusivity of Li ion in the electrode materials and the energy density by the capacity and potential difference of the electrode materials. Nanosizing has been proven to be a powerful strategy to improve battery performance. It reduces the transport distances within the solid state particles for both ions and electronic charges¹⁵. In addition the shorter reaction pathways often facilitate new types of reactions and in many materials also lead to higher capacities.^{15,17} Other potential advantages include better accommodation of the strain associated with the Li

ion intercalation due to relatively free surface expansions, and the more efficient Li exchange with electrolyte caused by the larger surface areas.^{15,18} However, the nano sword is double edged as the larger surface area of nano sized materials both increases undesirable side reactions between electrode and electrolyte and can decrease the volumetric energy densities by reduced packing densities of the nanoparticles^{15,18}.

1.3 Sodium ion battery

Lithium ion batteries exhibit excellent performance not only on the high energy density, but also with respect to long lifetimes and good cycle rate capabilities. However, the scarcity of lithium and its high cost form a potential constraint for the extensive application of Li-ion batteries technology in electric vehicles and household appliances. Sodium ion batteries were originally studied at the same time as lithium ion batteries, as Na and Li are in the same series of alkali metal elements. Owing to the huge success of lithium batteries, the attention for sodium ion batteries faded in the past decades. In the recent years, motivated by the increasingly demand for energy storage and relative scarcity of lithium resources, sodium ion batteries have however been attracting increasing attention again. The most distinct advantage of sodium ion batteries is the virtually unlimited source and low costs, as illustrated by table 1. Moreover, although the operating voltage of sodium ion batteries is approximately 0.4V lower than lithium ion batteries¹⁹ resulting in a somewhat lower energy and power density, this low voltage operation could make sodium ion electrode materials suitable for operation using aqueous electrolytes. This may be considered as a promising cheap, environmentally friendly battery concept for static energy storage. In this context $\text{Na}_{0.44}\text{MnO}_2$ has been reported to work as a potential positive electrode for aqueous electrolytes (with Na_2SO_4 as salt) demonstrating excellent cycling stability for 1000 cycles²⁰. In addition, compared to non-aqueous systems, aqueous systems are cheaper, non-flammable, less toxic, and have higher ionic conductivities.²¹

Compared with lithium ions (0.76 Å), Na ions have a larger ionic radius (1.02 Å), which upon insertion generally results in larger structural distortions of the host structure and larger diffusion barriers. This might be the prominent cause of the scarcity of reported insertion electrode materials for sodium ion batteries, especially negative electrode materials.

Table 1 Characteristics of Na and Li metals²¹

^a Purity: 98.8-99.2% min.; ^b Battery grade 99.9%; ^c S.H.E.: standard Hydrogen Electrode.

Characteristics	Na	Li
Price	0.07-0.37 ^a €kg ⁻¹	4.11-4.49 ^b €kg ⁻¹
Specific Capacity	1.16 Ahg ⁻¹	3.86 Ahg ⁻¹
Voltage vs S.H.E. ^c	-2.7V	-3.0V
Ionic radius	0.98Å	0.69Å
Melting point	97.7°C	180.5°C
Atomic mass	22.990u	6.94u

1.4 Motivation and research questions.

This thesis is divided into two parts. First, the particle size dependent phase transition of lithium inserted anatase TiO₂ is investigated both experimentally and theoretically. Secondly, the Na-ion storage in titanate compounds (Na₂Ti₆O₁₃ and nanocrystalline TiO₂ anatase) is studied as potential Na-ion negative electrodes.

Part I

Anatase TiO_2 has been reported as a promising negative electrode for Li-ion batteries due to its ability to reversibly store a large amount of Li ions resulting in excellent gravimetric and volumetric storage capacities, its chemical stability, abundance and environmental friendly properties. In the early stage the electrochemistry of bulk anatase TiO_2 was intensively studied, reporting several disadvantages, including poor ionic and electronic conductivity, and low rate capacity^{15,18}. Recently, nano-structuring was found to be a successful strategy to improve these drawbacks and provide a variety of favorable properties for energy storage^{15,18,22,23} motivating the exploration of the impact of nano sizing in anatase TiO_2 .²⁴⁻²⁷ One of the most striking features is the large impact of nano-sizing on the thermodynamics and kinetics of lithium ion insertion into anatase TiO_2 . Compared with micro sized materials, the voltage profile of nanosized anatase TiO_2 displays a much shorter plateau region.^{25,28,29} In addition, the phase transition behavior was found to depend strongly on size³⁰ indicating that the mechanism of the phase transition in nano TiO_2 anatase varies significantly from that in bulk anatase TiO_2 . This has motivated formulation of the following two questions:

(1) How does the particle size affect the phase transition behavior?

In chapter 3, a real-time characterization technique, in-situ X-ray diffraction was applied to monitor the detailed structure changes upon lithiation of different anatase TiO_2 particle sizes. The results from Rietveld refinement of the XRD patterns give insight in the two phase transition behavior, indicating a non-equilibrium process existing even at extremely low lithiation rates. Quasi-equilibrium electrochemistry measurements using the galvanostatic intermittent titration technique (GITT) was applied to study the equilibrium voltage, revealing a systematic dependence on particle size.

(2) What factors explain systematic thermodynamic property changes, that include the changing Li insertion phase behavior and decreasing equilibrium voltage when the particle

size is reduced? Is this a consequence of the increasing surface/bulk ratio, or an intrinsic phenomenon related to nanosizing?

In order to gain fundamental understanding of the the nanosizing effects first-principle calculations were performed. The results are presented in chapter 4. Nanosized TiO_2 was modeled by surface slabs having the two thermodynamically stable orientations $\{101\}$ and $\{001\}$. By using a surface cluster expansion, the phase stability at each Li composition is compared between different Li arrangements giving insight in the phase transition behavior upon particle size reduction and the impact of surfaces on the electrochemical performance.

Part II

Based on the low costs of sodium, the renewed interest in Na-ion batteries has lead to an exploration of suitable positive and negative electrode materials. In particular for the latter only few good materials have been reported, which is mainly attributed to the larger ionic size of Na ions. The use of Sodium metal as a negative electrode introduces complications such as dendrite formation, low melting point, high toxicity and interface aging.²¹ Carbon based materials, including the extensively investigated graphite and hard carbons, accommodate less Na-ions compared to Li-ions and results in high capacity fading.³¹ In addition the capacitive storage of Na-ions at the graphite surface has the disadvantage of a linear drop in the battery voltage lowering the energy density.^{32,33} Due to the competition between inversion and conversion reactions, only the 3d metal (Ti and V) oxides appear promising to achieve low voltage Na-ion insertion as required for negative electrodes.³⁴ Several promising materials have been identified including Na_xVO_2 , $\text{Na}_2\text{Ti}_3\text{O}_7$, anatase TiO_2 and $\text{Na}_2\text{Ti}_6\text{O}_{13}$.

Particularly, Rudola et al. explored Na-ion storage in $\text{Na}_2\text{Ti}_6\text{O}_{13}$ demonstrating excellent rate capacity and cycling stability. Recently, also anatase TiO_2 shows promising capacities in

particular at the nano-sized form³⁵⁻³⁷. Motivated by the promising features of $\text{Na}_2\text{Ti}_6\text{O}_{13}$ and anatase TiO_2 two questions form the basis of part II of the thesis.

(3) Is it possible to reversibly (de)insert sodium ion in $\text{Na}_2\text{Ti}_6\text{O}_{13}$ at low voltages to increase the capacity? And more fundamental questions, what are the structural changes and where does the inserting sodium ion go in $\text{Na}_2\text{Ti}_6\text{O}_{13}$?

In chapter 5, the electrochemistry of Na-ion storage in $\text{Na}_2\text{Ti}_6\text{O}_{13}$ is explored for different voltage windows. In-situ and ex-situ X-ray diffraction in combination with Density Functional Theory calculations reveal the intercalation mechanism and structural evolution, giving a consistent picture of the structural changes and electrochemical performance.

(4) What is the performance of very small nano crystalline TiO_2 , and what is the structural evolution and reversibility upon Na insertion? And how does the particle size influence that?

In chapter 6, the Na-ion storage in three different particle sizes increasing from 7nm to 130nm was prepared. Both experiment and calculations are performed to improve the understanding of the particle size effect on the Na insertion behavior in TiO_2 anatase. Distinct increase of the reversible capacity and fast degradation of the cycling stability was found when the particle size of TiO_2 anatase is reduced. X-ray diffraction on the electrode after discharge shows negligible changes on the crystalline lattice parameters, combined with overall loss of crystallinity and crystalline domain reduction. The result suggests that unlike the case for Li, for Na no solid solution nor a reversible crystalline phase transition proceed upon Na (de)insertion, but rather a severe surface restructuring occurs that enable reversible Na insertion in the resulting amorphous surface layer on the particles. DFT energy and diffusion barrier calculation are applied to model the crystalline structure and to estimate the intercalation voltage and Na ion migration barrier for a crystalline anatase.

References

- (1) Besenhard, J. O.; Fritz, H. P. *Journal of Electroanalytical Chemistry* **1974**, *53*, 329–333.
- (2) US EPA, C. C. D. *Inventory of U.S. Greenhouse Gas Emissions and Sinks: 1990-1998*; United States Environmental Protection Agency, 1998.
- (3) Guerard, D.; Herold, A. *Carbon* **1975**, *13*, 337–345.
- (4) Berresheim, H.; Whine, P. H.; D, D. D. *Chemistry and Climate of the Atmosphere*; Singh, H. B.; Van Nostrand Rheingold, Eds.; 1995.
- (5) Mulder, F. M. *Journal of Renewable and Sustainable Energy* **2014**, *6*, 033105.
- (6) *en.wikipedia.org*.
- (7) Schöllhorn, R.; Kuhlmann, R.; Besenhard, J. O. *Materials Research Bulletin* **1976**, *11*, 83–90.
- (8) Murphy, D. W.; Cava, R. J.; Zahurak, S. M.; Santoro, A. *Solid State Ionics* **1983**, *9-10*, 413–417.
- (9) Whittingham, M. S. *Science* **1976**, *192*, 1126–1127.
- (10) Whittingham, M. S. *Progress in Solid State Chemistry* **1978**, *12*, 44–99.
- (11) Thackeray, M. M.; David, W.; Bruce, P. G.; Goodenough, J. B. *Materials Research Bulletin* **1983**, *18*, 461–472.
- (12) Manthiram, A.; Goodenough, J. B. *Journal of power sources* **1989**, *26*, 403–408.
- (13) Padhi, A. K.; Nanjundaswamy, K. S.; Goodenough, J. B. *Journal of the Electrochemical Society* **1997**, *144*, 1188–1194.
- (14) Lithium-ion battery http://en.wikipedia.org/wiki/Lithium-ion_battery (accessed Dec 8, 2013).
- (15) Bruce, P. G.; Scrosati, B.; Tarascon, J.-M. *Angewandte Chemie-International Edition* **2008**, *47*, 2930–2946.
- (16) Tarascon, J. M.; Armand, M. *Nature* **2001**, *414*, 359–367.
- (17) Jiao, F.; Bruce, P. G. *Advanced Materials* **2007**, *19*, 657–660.
- (18) Aricò, A. S.; Bruce, P.; Scrosati, B.; Tarascon, J.-M.; van Schalkwijk, W. *Nature Materials* **2005**, *4*, 366–377.
- (19) Ong, S. P.; Chevrier, V. L.; Hautier, G.; Jain, A.; Moore, C.; Kim, S.; Ma, X.; Ceder, G. *Energy & Environmental Science* **2011**, *4*, 3680–3688.

- (20) Whitacre, J. F.; Tevar, A.; Sharma, S. *Electrochemistry Communications* **2010**, *12*, 463–466.
- (21) Palomares, V.; Serras, P.; Villaluenga, I.; Hueso, K. B.; Carretero-González, J.; Rojo, T. O. F. *Energy & Environmental Science* **2012**, *5*, 5884–5901.
- (22) MAIER, J. *Solid State Ionics* **2002**, *154-155*, 291–301.
- (23) MAIER, J. *Nature Materials* **2005**, *4*, 805–815.
- (24) Kavan, L.; Grätzel, M.; Rathousky, J.; Zukal, A. *Journal of Electrochemistry Society* **1996**, *143*, 394–400.
- (25) Sudant, G.; Baudrin, E.; Larcher, D.; Tarascon, J.-M. *Journal of Materials Chemistry* **2005**, *15*, 1263–1269.
- (26) Subramanian, V.; Karki, A.; Gnanasekar, K. I.; Eddy, F. P.; Rambabu, B. *Journal of power sources* **2006**, *159*, 186–192.
- (27) Kubiak, P.; Frotscher, T.; Hunsinger, N.; Hornemann, U.; Kaiser, U.; Schiller, R.; Weiss, C. K.; Landfester, K.; Wohlfahrt-Mehrens, M. *Small (Weinheim an der Bergstrasse, Germany)* **2011**, *7*, 1690–1696.
- (28) Yamada, A.; Koizumi, H.; Nishimura, S.-I.; Sonoyama, N.; Kanno, R.; Yonemura, M.; Nakamura, T.; Kobayashi, Y. *Nature Materials* **2006**, *5*, 357–360.
- (29) Kobayashi, G.; Nishimura, S.-I.; Park, M.-S.; Kanno, R.; Yashima, M.; Ida, T.; Yamada, A. *Advanced Functional Materials* **2009**, *19*, 395–403.
- (30) Wagemaker, M.; Borghols, W. J. H.; Mulder, F. M. *Journal of the American Chemical Society* **2007**, *129*, 4323–4327.
- (31) Doeff, M. M.; Ma, Y.; Visco, S. J.; De Jonghe, C. J. *Electrochem. Soc.* **1993**, *140*, L169–L170.
- (32) Alcántara, R.; Jiménez-Mateos, J. M.; Lavela, P.; Tirado, J. L. *Electrochemistry Communications* **2001**, *3*, 639–642.
- (33) Alcántara, R.; Lavela, P.; Ortiz, G. F.; Tirado, J. L. *Electrochemical and Solid State Letters* **2005**, *8*, A222.
- (34) Cabana, J.; Monconduit, L.; Larcher, D.; Palacin, M. R. *Advanced Materials* **2010**, *22*, E170–E192.
- (35) Xu, Y.; Memarzadeh Lotfabad, E.; Wang, H.; Farbod, B.; Xu, Z.; Kohandehghan, A.; Mitlin, D. *Chemical communications (Cambridge, England)* **2013**, *49*, 8973–8975.
- (36) Wu, L.; Buchholz, D.; Bresser, D.; Gomes Chagas, L.; Passerini, S. *Journal of power sources* **2014**, *251*, 379–385.
- (37) Kim, K.-T.; Ali, G.; Chung, K. Y.; Yoon, C. S.; Yashiro, H.; Sun, Y.-K.; Lu, J.; Amine, K.; Myung, S.-T. *Nano Letters* **2014**, *14*, 416–422.

Chapter 2

Methods

In this chapter, the experimental and theoretical approaches used in the thesis will be briefly described. The main techniques applied in this thesis can be divided into two types: experimental and computational. These two groups of techniques serve the same goal, and they are necessarily linked to the same topic of research in a complementary manner, which is shown in the following chapters. For instance in-situ X-ray diffraction was applied to different particle sizes TiO_2 anatase upon electrochemical lithiation to probe the phase transition mechanism. Using Density Functional Theory (DFT) calculations the phase stability and structural changes on the atomic scale in bulk structures and surface structures were revealed. The relative stability of Li configurations at different Li compositions resulted in substantial new insights regarding the particle size effects on the phase transformation that occurs upon electrochemical lithiation. In part II, the same approach applying in- and ex-situ X-ray diffraction and DFT was used to characterize the structural evolution upon Na insertion in $\text{Na}_2\text{Ti}_6\text{O}_{13}$ and anatase TiO_2 .

2.1 Experimental techniques

2.1.1 Materials synthesis

In part I, the pristine material used in the research is commercially available. TiO_2 anatase crystalline particles with three different dimensions (15 nm, 41 nm and 130 nm) were obtained from Aldrich.

In part II, the pristine material $\text{Na}_2\text{Ti}_6\text{O}_{13}$ was prepared from Na_2CO_3 and TiO_2 anatase (Aldrich) in a mass ratio 0.22:1 by ball milling in a silicon carbide crucible applying the rate of 250 rpm for 120 minutes. Subsequently, this precursor mixture was heated at 800°C in open air for 12 hours, applying a heating and cooling ramp rate of $5^\circ\text{C}/\text{min}$. X-ray diffraction analysis confirmed the presence of the crystalline $\text{Na}_2\text{Ti}_6\text{O}_{13}$ phase with less than 10% of unreacted TiO_2 anatase in the end product.

2.1.2 Electrode preparation

Electrode preparation for electrochemistry

Electrodes for the electrochemistry measurements were prepared by mixing 80 wt% active materials (TiO_2 anatase or $\text{Na}_2\text{Ti}_6\text{O}_{13}$) with 10 wt% conducting carbon black additive (ENSAQO) and 10wt% polyvinylidene fluoride (PVDF) binder in N-methylpyrrolidinone (NMP) solvent. When the well-mixed slurry achieved the appropriate viscosity, it was casted on carbon coated aluminum foil current collector using the “doctor blade” method. The casted electrodes were dried in a vacuum furnace at approximately 100°C for several days.

Electrode preparation for in-situ XRD

Self-supporting thin film electrodes were prepared for the in-situ XRD measurements. Firstly, 30 wt% polyvinylidene fluoride (Kynar Power-flex binder) and approximately same amount of dibutyl-phthalate (DBP plasticizer) were mixed in acetone. In the final step the DBP plasticizer was extracted by washing with diethyl ether. The composition mentioned in this recipe is given by assuming all DBP has been washed out. The solution was stirred until all the materials were dissolved. Secondly, 50 wt% TiO_2 anatase and 20 wt% carbon black were well mixed by 20 times ball milling for 4 minutes at 130 rpm. Thirdly, the ball-milled sample was added to the acetone solution and stirred for several hours until it reached the appropriate viscosity. Subsequently, the slurry was casted on glass by the “doctor blade” method. In the end, the prepared film was washed with diethyl ether to extract DBP plasticizer. The coated film was also dried in a vacuum furnace at around 100°C for several days.

2.1.3 Electrochemical tests

A Swagelok type cell or vacuum O-ring flange cell was used in the electrochemical measurements. The electrodes were mounted under Argon atmosphere (H_2O and $\text{O}_2 < 0.1\text{ppm}$). The prepared electrodes with a diameter of 13 mm served as positive electrode, and the same size lithium metal foil served as the negative electrode. The two electrodes were separated by glass microfiber filter (Whatman) with a few droplets of 1mol/liter LiPF_6 (EC:DMC=1:1, Novolyte) electrolyte.

For the in-situ XRD measurement, a dedicated airtight electrochemical cell with a Beryllium window on top was designed and applied for the in-situ X-ray diffraction measurements (see figure 2.1). The Beryllium window serves as X-ray transparent window and current collector. A thin aluminum foil ($2\mu\text{m}$) was used to separate the electrode from the beryllium window to avoid possible corrosion of the Beryllium. Al can be used at potentials higher than about 0.2V since at lower voltages Li will also react with the Al. The electrodes were mounted under Argon atmosphere (H_2O and $\text{O}_2 < 0.1\text{ ppm}$). The prepared self-supporting film was used as positive electrode, and the lithium metal foil was used as the negative electrode. The two electrodes were separated by glass microfiber filter (Whatman) with a few droplets of $1\text{mol/liter LiPF}_6(\text{EC}:\text{DMC } 1:1, \text{Novolyte})$ electrolyte.

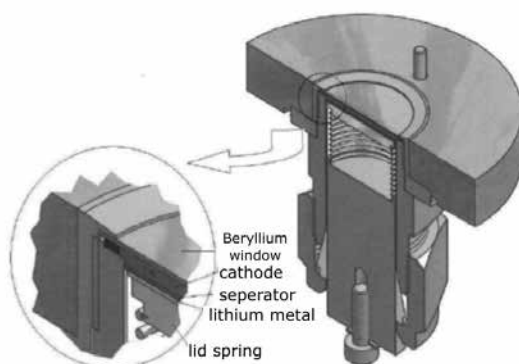


Figure 2.1 the schematic picture of the in-situ cell vertical cross-section

All the electrochemical characterization was performed by a Maccor 4300 battery cycler. For the Galvanostatic Intermittent Titration Technique (GITT), aiming at determining the equilibrium voltage profile, the cells were intermittently discharged at a rate of $C/20$ (here $1C$ is defined as the current required to fully discharge/charge the TiO_2 electrode in 1 hour assuming the maximum composition is $\text{Li}_x\text{Ti}_2\text{O}_7$) for 30 minutes with relaxation periods maintained until the voltage variation was lower than 3 mV/h or until the relaxation time exceeded 20 hours.

2.1.4 X-ray powder diffraction

In this thesis, X-ray diffraction is applied to characterize the materials structures. Diffraction of an incident X-ray beam on the crystal lattice of the sample material results in a diffracted pattern as a function of diffraction angle. By analyzing the angles, intensities, and broadening of the diffracted intensities, the unit cell dimensions and symmetry as well as the atomic positions can be determined, in this case using the Rietveld refinement implemented in GSAS¹. In addition, if the data quality allows also crystalline size and strain can be probed.

In the present research powder x-ray diffraction was applied to determine crystalline phases in battery electrodes consisting of powder particles. A powder can be considered as a polycrystalline solid, containing a large number of small crystallites, for which the powder diffraction exhibits an orientation average of all the crystallites in the detected region. All the X-ray diffractions in this thesis were performed using a Panalytical X'pert Pro X-ray diffractometer employing Cu-K α radiation.

For the ex-situ X-ray diffraction experiments, the air-sensitive electrode samples was removed from the cell and assembled in a Kapton covered airtight X-ray diffraction sample holder. All these operations were performed in a glove box under Argon atmosphere ($O_2 < 0.1$ ppm and $H_2O < 0.1$ ppm).

For the in-situ X-ray diffraction the cell preparation is described in the electrochemical section.

Basic theory

When X-rays are incident on the lattice planes of the crystal, the scattered waves will be generated from the elastic scattering interaction between the incoming X-rays and the electron

density of the sample material. The re-emitted waves originating from the periodically spaced lattice planes interfere with each other, leading to constructive interference in directions obeying Bragg's law, as shown in figure 2.2.

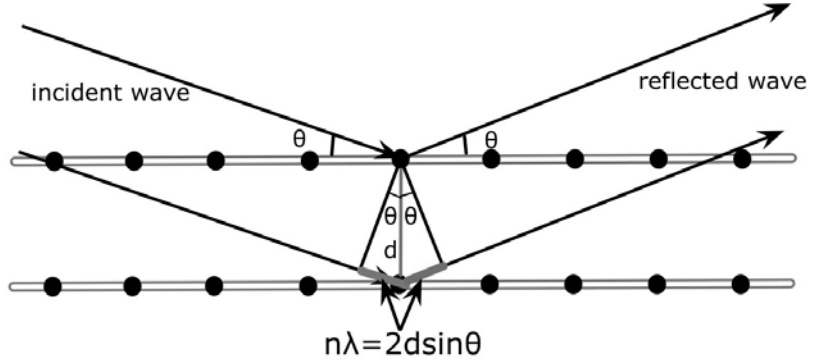


Figure 2.2 Schematic diagram of Bragg's law diffraction

Only when the scattering waves satisfy Bragg's law the constructive interference from successive crystallographic planes can occur resulting in the intensities at specific diffraction angles forming the diffraction pattern.^{2,3} Bragg's law is expressed as follows:

$$2d\sin\theta = n\lambda \quad \text{Eq. 2.1}$$

Where θ is the scattering angle, d is the crystallographic interplanar spacing, n is an integer and λ is the wavelength of the incident X-rays. For powder diffraction, we assume that the number of crystallites for each orientation is equal.

The crystallographic data of the sample can be deduced from the intensities and angles of the X-ray powder diffraction reflections.³ The peak intensities are related to the structural factor $F_{(hkl)}$ as follows:

$$I_{(hkl)} = s \cdot p_{(hkl)} \cdot L_{\theta} \cdot A_{\theta} \cdot P_{(hkl)} \cdot |F_{(hkl)}|^2 \quad \text{Eq. 2.2}$$

Where s is a scale factor, L is the Lorentz-polarization, p is the multiplicity, A is the absorption correction, and P is preferred orientation. Besides the structure factor all other are independent from the diffraction angle and the sample material, so the peak intensity is directly proportional to the square of the structural factor. The structural factor is defined as;

$$F_{(hkl)} = \sum_j f_j \exp[2\pi i(hx_j + ky_j + lz_j)] \exp[-B_j \sin^2 \theta / \lambda^2] \quad \text{Eq. 2.3}$$

Where f_j is the form factor, characterizing the strength and distribution of the scattering species; the second item of the function is the contents of the unit cell, which determines if a reflection is allowed or forbidden; the third item of the function is the temperature factor, which reflect the impact of the thermal motion of the atoms.^{3,4}

Diffraction peak profile

The shape of the diffraction peaks is determined by instrument and powder specimen induced broadening. The origin of the instrumental broadening includes non-ideal optics of the diffractometer, wavelength dispersion, sample transparency, axial divergence, flat sample effects and detector resolution. The contribution from the specimen is mainly caused by the deviations from ideal crystallinity, such as finite crystallite size and micro stain. The properties of the powder sample can be extracted by analyzing this broadening.⁵

No perfect crystal exists in the real world due to its finite size. Diffraction peak broadening is partly caused by this deviation from the perfect crystallinity. The Scherrer equation describes the relationship between the crystallite size and the line broadening⁶ and is as follows:

$$L(2\theta) = \frac{K\lambda}{B \cos \theta} \quad \text{Eq. 2.4}$$

Where K is the Scherrer constant, λ is the wavelength of the incident radiation, B is the integral breadth of the reflection at 2θ and L represents the volume weighted crystallite size. The crystallite size L is inversely proportional to peak width B.^{7,8}

The lattice strain, generally produced by phase boundaries and dislocations, is a common phenomenon observed in nanocrystalline materials. Stokes and Wilson first proposed the strain could give rise to line broadening, which can be described as followed:⁹

$$\varepsilon(2\theta) = \frac{B}{4 \tan \theta} \quad \text{Eq. 2.5}$$

Where ε represents the weighted average strain. It is worth mentioning that both crystallite size and strain vary with the diffraction angle θ , but with a different dependence, which makes it possible to discriminate the two effects by analysing the resulting angular dependence of the broadening.

Rietveld refinement

In this thesis Rietveld refinement as implemented in GSAS was applied to extract the crystal structure details from the diffraction patterns. Rietveld refinement is a method firstly proposed by Hugo Rietveld when working at the High Flux Reactor in Petten, The Netherlands. By varying parameters of the theoretical line profile, the difference between the calculated pattern and the experimental measured pattern can be minimized.

GSAS (General Structure Analysis System) is a comprehensive software package for fitting both X-ray and neutron diffraction patterns with structural models¹. With this tool, the structural details of the crystalline materials including lattice parameters, crystal phase

fractions, and domain size broadening of each phases of the sample material can be directly obtained.

2.2 DFT calculation

In this thesis, several theoretical methods have been applied to determine the thermodynamic properties of titanium oxides materials upon lithium and sodium insertion. Determination of thermodynamic properties requires the energetics of the titanium materials as a function of lithium and sodium insertion. Corresponding First-principles calculations use pseudo potentials to represent the nuclear charges and the valence electrons as input to predict the quantum state of the valence electrons by solving the electronic Schrödinger equation

$$E\Psi = \hat{H}\Psi \quad \text{Eq. 2.6}$$

In practice, the physical solution of Schrödinger equation can only be quantitatively estimated by employing physical approximations. Currently, Density Functional Theory (DFT) has been considered as the preferred means of the first-principles energy calculations.^{10,11}

2.2.1 DFT theory

DFT is a quantum mechanical modeling method to calculate accurate solutions of Schrödinger equation by employing a series of physical approximations. It has proved powerful in energy prediction and electronic structure investigation of a vast class of materials, such as solid crystal phases and molecules. The main difficulty of DFT is to describe the functional of exchange and correlation (which is not exact except for a free electron gas). The Local Density

Approximation(LDA) ^{12,13} and the Generalized Gradient Approximation(GGA) ^{14,15} are the two most widely used approximations in DFT, making the accurate calculation of physical quantities become possible.

LDA and GGA provided successful approximations for materials properties prediction, giving excellent agreement with the experimental data. However, these two approximations do not work well in all cases. Because LDA and GGA are based on the assumption of homogeneous electron gas, large error occurs in transition metal oxides which exhibit strong electron localization^{16,17}. It directly leads to underestimation of the potential of titanate oxides compounds, which have a strong electron self-interaction in the d-orbitals ^{18,19}(see chapter 4 and 5).

2.2.2 Average voltage calculation

The average intercalation voltage calculation is mainly based on a paper published in 1997 by M.K.Aydinol and co-workers.²⁰ Upon battery (dis)charging the cell voltage varies due to the interaction of Li-ions with the solid state electrode materials. For the lithium half-cell, the equilibrium voltage is determined by the Li chemical potential difference between the positive electrode and Li metal, as shown in eq 2.7²⁰

$$V(x) = -\frac{\mu_{Li}^{cathod}(x) - \mu_{Li}^{anode}}{zF} \quad \text{Eq. 2.7}$$

Where z is the electron charge transported by every lithium ion (z=1 for Li), and F is the Faraday's constant. The chemical potential of the Li metal anode is constant. So in the lithium half-cell, the cell voltage directly depends on the chemical potential of the interstitial compound. We assume that all the transported charge is the result of Li (de)intercalation,

$\Delta q = e \cdot \Delta x$. The electrical energy as a function of Li composition (from x_1 to x_2) can be estimated by the integral of the voltage times the transferred charge:²⁰

$$\begin{aligned}
 E &= \int_0^{q_{\text{tot}}} V(x) dq = - \int_0^{q_{\text{tot}}} \frac{\mu_{Li}^{\text{Cathode}}(x) - \mu_{Li}^0}{e} dq \\
 &= - \int_{x_1}^{x_2} [\mu_{Li}^{\text{cathode}} - \mu_{Li}^0] dx_{Li} \\
 &= -[G_{Li_{x_2}MO_2} - G_{Li_{x_1}MO_2} - (x_2 - x_1)G_{Li}] \\
 &= -\Delta G_r
 \end{aligned}
 \tag{Eq2.8}$$

Then the average intercalation voltage is

$$V = \frac{-\Delta G_r}{(x_2 - x_1)F}
 \tag{Eq2.9}$$

Where μ_{Li}^0 is the chemical potential of Li metal, $\mu_{Li}^{\text{IC}}(x)$ is the chemical potential of Li in the interstitial compound and e is the electronic charge.

Therefore, eq 2.9 indicates that the average intercalation voltage can be calculated if the Gibbs free energy difference between Li compositions is known.

However, the ground state free energy for each Li composition is not easy to obtain due to the site disorder of lithium ions. The energy dependence on Li disorder can be parameterized by the cluster expansion method, which will be introduced in section 2.2.4. Besides the configurational disorder, the entropy effects caused by lattice vibrations and electronic excitations also add to the Free energy, but are considered to be small and are thus neglected in the energy calculation in this thesis.²¹

According to thermodynamics

$$-\Delta G_r = \Delta E_r + P\Delta V_r - T\Delta S_r
 \tag{Eq. 2.10}$$

where ΔE_r is the total energy changes, ΔV_r and ΔS_r are the volume and entropy changes upon Li (de)intercalation respectively. The contribution from the latter two items of eq. 2.10 can be neglected, since the term $P\Delta V_r$ and $T\Delta S_r$ is several orders of magnitude smaller than ΔE_r . The average intercalation voltage can therefore be approximated by calculating the total energies difference ΔE_r between two compositions.

2.2.3 Surface calculation

Surface structure construction

In the chapter 4, nanosized lithiated Li_xTiO_2 was modeled by constructing surface slabs. The periodically repeated crystal atomic structure was separated by vacuum layers around 20 Å. The thickness of the vacuum layer is varied until the changes on surface energy are lower than 5% compared with the adjacent calculated value. In the VASP calculations, a set of infinite atomic layers separated by vacuum becomes the periodically repeated unit along the surface normal, which is schematically presented in figure 2.3. During the ionic relaxation stage, all the atoms in the system are allowed to move but the cell volume of the supercell is fixed.

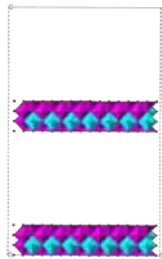


Figure 2.3 Stacking of the surface slab structure of Li_1TiO_2 structure along the $\{001\}$ direction. The blank area represents the vacuum, light blue polyhedral represents the Li octahedral, and the pink polyhedral represents the Ti octahedral, and the red atoms represents oxygen.

Wulff construction

The Wulff construction enables the determination of the equilibrium particle shape of a given crystal.²² The equilibrium shape requires that the total surface energy must be minimized at a fixed volume. For this the surface energies $E^{surf}(\hat{n})$ of various crystallographic orientations need to be calculated. The polar plot of the surface energies is performed by drawing a vector \hat{n} along the corresponding orientation, the length of which equals to $E^{surf}(\hat{n})$. Then a plane perpendicular to the orientation, passing through the end point of \hat{n} , is drawn. The Wulff construction is formed by the inner envelop of all these planes. In this thesis, the “Wulffman” software is used to generate the Wulff shape of crystals.

2.2.4 Cluster expansion

Surface cluster expansion

For the generally known Li ordering phase, the ground state energy calculation (DFT) is sufficient to determine some properties, such as the band structure and redox voltage etc. But for the Li_xMO_2 that deviates from stoichiometry, the uncertainty of Li distribution over the possible lithium sites in the host leads to a degree of disorder and a number of different energies. Besides that, at non-zero temperature, the thermal energy in the system will also result in continuous changes of the Li-vacancy arrangements in the host structure, potentially different from the ground state. It means that the energies of all possible Li-vacancy configurations need to be calculated by DFT calculation, which is practically limited by the computational time.

In the past decade, methods to solve this problem have been well developed by, among others, Ceder's group, namely cluster expansion.²³⁻²⁶ Cluster expansion is a powerful tool to construct an accurate extrapolation of total energy of any possible Li-vacancy configuration in the system based on first-principles energy calculations of a few ordered configurations. The main approach can be summarized as followed²⁷:

i) A variety of symmetry inequivalent Li-vacancy configurations over the well-defined interstitial sites of host structure are enumerated by cluster expansion formalism(see figure 2.4), the total energies of which are calculated with DFT using VASP code.

ii) By parameterizing cluster expansion over the relevant configurations with the energetic data obtained in the first step, the total energies of arbitrary Li-vacancy configurations can be accurately and rapidly extrapolated by this converged cluster expansion.

iii) This cluster expansion is then evaluated as input in the Monte Carlo simulation to calculate the thermodynamic properties of the system, such as free energy, chemical potential and phase diagram etc.

It is worthy to note that in the cluster expansion, we only consider the configurational degree of freedom associated with lithium ions hopping (Li-vacancy arrangements), but neglect the fluctuations from lattice vibration and electronic excitations, which occur in much shorter time scale.

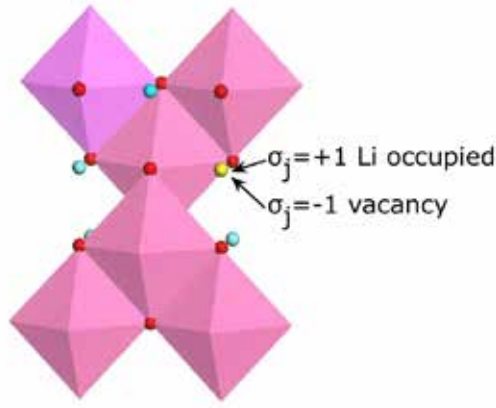


Figure 2.4 Occupation of Li sites in analogy to spin variables in the Li_xTiO_2 structure. Pink polyhedral is the TiO_6 octahedral, red atoms are oxygen and blue atoms are the lithium ions. The yellow atom represents the spin variables, the value of which is varied between +1 and -1 when this site is occupied by lithium or vacancy.

According to Ising model, we introduce a configurational variables σ_i , which is analogous to a spin variable representing whether the site i is occupied (+1) or not (-1), as shown in figure 2.4. Then

$$\vec{\sigma} = (\sigma_1, \sigma_2, \sigma_3, \dots, \sigma_i, \dots, \sigma_m) \quad \text{Eq2.11}$$

can be defined to uniquely represent a specific configuration. In practice, the called cluster function ϕ_α enables a more manageable way to specifies configurations with a polynomials function of the discrete configurational variables σ_i belonging to clusters Φ_α of sites

$$\phi_\alpha(\vec{\sigma}) = \prod_{i \in \alpha} \sigma_i \quad \text{Eq2.12}$$

where i represents the sites within the cluster Φ_α . Then the configurational energy can be expanded in the form of

$$E(\vec{\sigma}) = C_0 + \sum_{\alpha} C_{\alpha} \phi_{\alpha}(\vec{\sigma}) \quad \text{Eq2.13}$$

Where the C_0 and C_{α} are the Effective Cluster Interactions (ECI). The cluster functions $\phi_{\alpha}(\vec{\sigma})$ form a complete and orthonormal basis set in configuration space, so in principle the cluster expansion is capable of describing the configurational dependence of the total energies of the whole host crystal. However, only if the rapid convergence of Eq2.13 is guaranteed, can the cluster expansion of the energies in the host structure be of practical significance. The cluster expansion in Eq2.13 can be truncated at a cluster size limit, exceeding which the contribution on the total energy from clusters can be neglected. ECIs are then determined by fitting energetic data obtained from DFT calculations on the selected ordered configurations. Generally, the ECIs fitting is performed by implementing a linear programming technique to minimize the least squares sum²⁸

$$\sum_{i=1}^P [E_0(\vec{\sigma}) - \sum_{\alpha}^{\alpha_{\max}} C_{\alpha} \phi_{\alpha}(\vec{\sigma})]^2 \quad \text{Eq 2.14}$$

For the surface structure of Li_xTiO_2 anatase, called surface cluster expansion is performed in a and b axes, excluding the c axis along which the vacuum layers periodically repeat. A shortened set of ECI coefficients are fit to 142($\{101\}$) and 138 ($\{001\}$) accurate energies of ordered configurations by first-principle calculation, which makes it possible to rapidly calculate the total energy of any Li configuration in the host.

Thermodynamic properties

Formation energies are defined for a given Li-vacancy arrangement upon the varied x in Li_xMO_2 as follows:

$$E_{Form} = E - xE_{LiMO_2} - (1-x)E_{MO_2} \quad \text{Eq2.15}$$

Where E is the total energy of the Li-vacancy arrangements at the Li_xMO_2 composition , E_{LiMO_2} is the total energy of fully occupied Li configuration, and E_{MO_2} is the total energy of the empty host structure. Compared to these total energies, formation energies bring forward the relative phase stability^{19,27}.

The intercalation voltages of the ground states structure at 0 kelvin can be calculated by DFT as described in the previous section. However, for the structures away from the stoichiometry of the ordered ground states or at elevated temperature (not 0 K), the energetic data cannot be estimated solely based on DFT. This can be achieved by Monte Carlo simulations based on the cluster expansion approach, which enables the calculation of thermodynamic properties at finite temperatures, including the chemical potential, free energy and the phase diagram.

It is important to note that in Cluster expansion fitting, the energetic data are fitted to formation energies, which choose $LiMO_2$ and MO_2 as the reference states. While the reference states need to be changed back to the original reference states (Li in Li metal or Na in Na metal chemical potential) when we calculate the voltage curves. This can be done as follows:

$$V = -\mu(x) - (E_{LiMO_2} - E_{MO_2} - E_{Li}) \quad \text{Eq2.16}$$

Where $\mu(x)$ is the chemical potential obtained from the Monte Carlo simulations, E_{LiMO_2} , E_{MO_2} and E_{Li} have the same meaning as described above.

References

- (1) Larson, A. C. GSAS; Los Alamos National Laboratory, 1994.
- (2) Bragg, W. L.; Bragg, W. H. *Proceedings of the Cambridge Philosophical Society* **1913**, 17, 43–57.
- (3) W, M. *Crystal Structure determination*; Springer: Berlin, 2004.
- (4) Brent, F.; Howe, J. M. *Transmission electron microscopy and diffractometry of materials*; 3rd ed.; Springer: Heidelberg, 2007.
- (5) Klug, H. P.; Alexander, L. E. *X-Ray Diffraction Procedures for Polycrystalline and Amorphous Materials*; 2nd ed.; John Wiley & Sons, 1974.
- (6) Patterson, A. *Physical Review* **1939**, 56, 978–982.
- (7) Scherrer, P. *Nachr. Ges. Wiss.* **1918**, 26, 98–100.
- (8) Langford, J. I.; Wilson, A. J. C. *Journal of Applied Crystallography* **1978**, 11, 102–113.
- (9) Stokes, A. R.; Wilson, A. J. C. *Proceedings of the Physical Society* **1944**, 56, 174–181.
- (10) Hohenberg, P.; Kohn, W. *Physical Review* **1964**, 136, B864.
- (11) Kohn, W.; Sham, L. J. *Physical Review* **1965**, 140, A1133.
- (12) Ceperley, D. M. *Physical Review Letters* **1980**, 45, 566–569.
- (13) Perdew, J. P.; Wang, Y. *Physical Review B* **1992**, 45, 13244–13249.
- (14) Perdew, J. P.; Burke, K.; Ernzerhof, M. *Physical Review Letters* **1996**, 77, 3865–3868.
- (15) Perdew, J.; Burke, K.; Wang, Y. *Physical Review B* **1996**, 54, 16533–16539.
- (16) Jones, R. O. *The Li intercalation potential of LiMPO₄ and LiMSiO₄ olivines with M=Fe, Mn, Co, Ni* **1989**, 61, 689–746.
- (17) Pickett, W. *The Li intercalation potential of LiMPO₄ and LiMSiO₄ olivines with M=Fe, Mn, Co, Ni* **1989**, 61, 433–512.
- (18) Zhou, F.; Cococcioni, M.; Kang, K.; Ceder, G. *Electrochemistry Communications* **2004**, 6, 1144–1148.
- (19) Wagemaker, M.; Van der Ven, A.; Morgan, D.; Ceder, G.; Mulder, F. M.; Kearley, G. J. *Chem. Phys.* **2005**, 317, 130–136.
- (20) Aydinol, M. K.; Kohan, A. F.; Ceder, G.; Cho, K. *Physical Review B* **1997**, 56, 1354–1365.
- (21) Asta, M.; McCormack, R.; de Fontaine, D. *Physical Review B* **1993**, 48, 748–766.
- (22) Wulff, G.; Kristallogr, Z. *Mineral* **1901**, 34, 449.
- (23) Van der Ven, A.; Marianetti, C.; Morgan, D.; Ceder, G. *Solid State Ionics* **2000**, 135, 21–32.

- (24) Van der Ven, A.; Ceder, G. *Physical Review B* **1999**, *59*, 742–749.
- (25) Ceder, G.; Van der Ven, A. *Electrochim. Acta* **1999**, *45*, 131–150.
- (26) Van der Ven, A.; Aydinol, M. K.; Ceder, G.; Kresse, G.; Hafner, J. *Physical Review B* **1998**, *58*, 2975–2987.
- (27) Ven, der, A. V. *Doctoral Thesis* **2000**.
- (28) Garbulsky, G.; Ceder, G. *Physical Review B* **1995**, *51*, 67–72.

Part I

Lithium ion insertion in TiO_2 anatase

Chapter 3

Impact of particle size on the non-equilibrium phase transition of lithium inserted anatase TiO_2

Based on paper

“Impact of Particle size on the Non-equilibrium Phase Transition of Lithium Inserted Anatase TiO_2 ” K. Shen, H.Chen, F. Klaver, F. Mulder and M. Wagemaker; Chemistry of Materials, 2014, 26(4), 1608-1615

Abstract

The phase transformation behavior of anatase TiO_2 in Li-ion battery electrodes is critical for its electrode kinetics and cycle life. Here we reveal unexpected particle size dependent phase transformation behavior in TiO_2 anatase by in-situ X-ray diffraction. The equilibrium voltage measured by GITT decreases progressively with reducing the particle size which can be attributed to the difference in surface energy of the pristine and lithiated phases. Based on the evolution of domain size and phase fraction of the two phases, it is concluded that the first order phase transition proceeds by continuous nucleation upon lithium insertion. For all particle sizes the phase boundary is found to migrate under non-equilibrium conditions even during very slow (dis)charge conditions, as reflected by a distinct deviation from the Li solubility limit during the phase transformation. Remarkably, the degree of non-equilibrium condition increases with decreasing particle size, rationalized by the difference in the observed phase transition

behavior between small and large particles. The absence of phase coexistence in smaller particles in combination with the sluggish ionic transport rationalizes the better electrochemical performance of the nano structured anatase TiO_2 as compared to the micro sized material. These results suggest a very low nucleation barrier for the formation and movement of the phase boundary in combination with sluggish ionic migration. Therefore strategies to improve the rate performance of nano structured anatase TiO_2 should concentrate on improving the interstitial diffusion, for instance by appropriate doping.

3.1 Introduction

Anatase TiO_2 is a promising negative electrode for Li-ion batteries due to its ability to store a large amount of Li-ions reversibly,¹⁻⁴ its excellent gravimetric and volumetric storage capacities,^{5,6} its chemical safety and environmental friendly properties. In the last decades the electrochemistry of bulk anatase TiO_2 has been widely studied, reporting disadvantages, such as poor ionic and electronic conductivity, and low capacity retention upon high rate (dis)charge.^{7,8} Recently, nanostructured materials are found to be very promising, mitigating the disadvantages in bulk materials and providing a variety of favorable properties for electrochemical energy storage phenomena⁷⁻⁹ that are also explored in nano-sized anatase TiO_2 .¹⁰⁻¹³ One of the most striking features is the large impact of nano-sizing on the thermodynamics and kinetics of Li-ion insertion reactions in anatase TiO_2 . Nano-sizing anatase TiO_2 results in a curved open cell voltage profile with a much shorter plateau region in comparison with that of micron sized materials.^{11,14,15} The miscibility gap shifts and shrinks with decreasing particle size¹⁶ which has been suggested to be the result of interfacial strain,

the diffuse interface^{17,18} as well as surface energy effects.^{14,15} In addition it was found that the phase transformation behavior in nano anatase TiO₂ is size dependent, and its mechanism is significantly different from that in bulk anatase TiO₂. During the first order phase transition the phases appear not to coexist in nanosized particles, whereas they coexist in particles larger than 40 nm.¹⁶

The aim of this paper is to gain insight in the particle size dependent phase transition mechanism under realistic in-situ conditions. Quasi-equilibrium electrochemistry measurement using galvanostatic intermittent titration technique (GITT) was applied to study the equilibrium voltage revealing a systematic dependence on the particle size. Detailed structural changes observed by in-situ X-ray diffraction indicate a non-equilibrium condition, which explains the difference in the observed phase transition behavior between small and large particles sizes as a kinetic rather than a thermodynamic effect.

3.2 Methods

Materials.

TiO₂ anatase crystalline particles with three different dimensions (15nm, 41nm and 130nm) were obtained from Aldrich. The particle sizes were confirmed by analyzing the particle size broadening of the X-ray diffraction reflections.

Sample preparation and GITT measurements

Electrodes for the GITT measurements were prepared by mixing the TiO₂ anatase (80wt%) with conducting carbon black additive (ENSAQO, 10wt%) and polyvinylidene fluoride (PVDF) binder (10wt%) in N-Methyl-pyrrolidone (NMP). When the well-

mixed slurry achieved the appropriate viscosity, it was casted on a carbon coated aluminum foil current collector using the 'doctor blade' method. The casted electrodes were dried in a vacuum furnace at approximately 100 °C for several days. A Swagelok type cell was used for GITT measurements. The electrodes were mounted under Argon (H_2O and $\text{O}_2 < 0.1$ ppm). The prepared TiO_2 anatase electrodes with a diameter of 13mm served as positive electrode, and a similar size lithium metal foil as the negative electrode. The two electrodes were separated by glass microfiber filters (Whatman) with a few droplets of 1 mol/liter LiPF_6 (EC:DMC 1:1, Novolyte) electrolyte. Galvanostatic Intermittent Titration Technique (GITT) experiments were performed using a Maccor 4300 battery cycler. In order to obtain the equilibrium voltage evolution the cells were intermittently discharged at the rate of C/20 for 30 minutes with relaxation periods maintained until the voltage variation was lower than 3 mV/h or until the relaxation time exceeded 20 hours.

Sample preparation and in-situ X-ray diffraction

Self-supporting film electrodes were prepared for the in-situ XRD measurements. Firstly, 0.34g dibutyl-phthalate (DBP plasticizer) and 0.4g Kynar Power-flex (binder) were mixed in acetone. The solution was stirred until all the materials were dissolved. Secondly, 0.77g TiO_2 anatase and 0.17g Carbon Black (ENSAQO) were mixed by 20 times ball milling for 4 minutes at 130 rpm. Thirdly, the ball-milled sample was added to the acetone solution and stirred for several hours until it reached the appropriate viscosity. In the next step the slurry was casted on glass by doctor blading. The prepared film was washed with diethyl ether to extract the plasticizer. The amount of TiO_2 anatase active material was 54% of the total electrode weight, assuming all DBP has been washed out. The coated film was dried in a vacuum furnace around 100 °C for

several days. A dedicated airtight electrochemical cell with a Beryllium window on top was designed and applied for the in-situ X-ray diffraction measurements. A thin aluminum foil (2 μ m) was used to separate the anatase electrode from the beryllium window to avoid possible corrosion of the Beryllium. The electrodes were mounted under Argon (H_2O and $O_2 < 0.1$ ppm), the prepared self-supporting TiO_2 anatase electrodes as positive electrode, and the lithium metal foil as the negative electrode. The two electrodes were separated by glass microfiber filters (Whatman) with a few droplets of 1 Molair $LiPF_6$ (EC:DMC 1:1, Novolyte) electrolyte.

The in-situ cell was placed in a Panalytical X'pert Pro X-ray diffractometer employing Cu-K α radiation. The electrochemistry tests during in-situ XRD were performed on a Maccor 4300 battery cycler. For all particle sizes the in-situ cell was discharged at C/120. X-ray diffraction patterns were collected between 22 and 64 degrees every one hour during discharge. The refinement was performed using the Rietveld method as implemented in GSAS.^{19,20} The patterns were corrected for the X-ray absorption introduced by the Beryllium window and the Aluminum foil. The fitting parameters included the lattice parameters, crystal phase fractions, domain size broadening of each phases, and the background.

3.3 Results and Discussion

3.3.1 Size effect on the equilibrium voltage

The GITT measurements in Figure 3.1 illustrate the evolution of quasi-equilibrium voltage for the different particle sizes. A constant voltage plateau, resulting from the

well-known phase transformation from anatase to Li-titanate, is observed for different particle dimensions (130nm and 15nm), which is in good agreement with previous studies^{11,21}. Here we use $\alpha\text{-Li}_{x\alpha}\text{TiO}_2$ to denote Li-poor anatase TiO_2 ($x_\alpha \sim 0.026$ in micro anatase TiO_2 in equilibrium)⁶, and $\beta\text{-Li-titanate}$ to denote the Li-rich Li-titanate phase ($x_\beta \sim 0.55$ in micro Li-titanate in equilibrium)⁶.

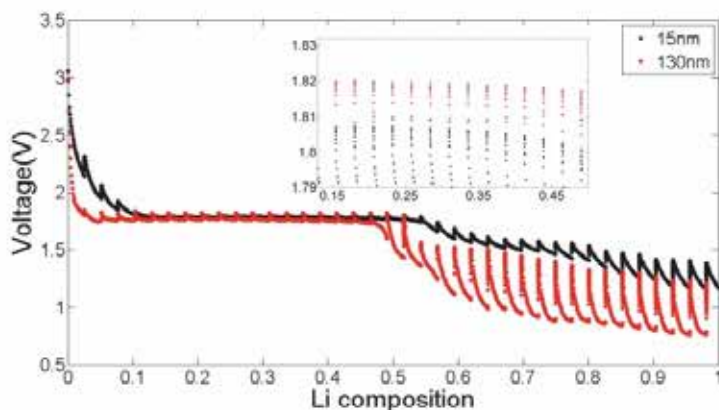


Figure 3.1. Voltage-composition profile obtained with Galvanostatic Intermittent Titration Tests (GITT) during discharge for different particle sizes. Inset: Comparison of the voltage plateau between different particle sizes; note the higher voltage for the larger particles.

There are three obvious differences in the voltage behavior between different particle sizes: (i) the onset of a second voltage plateau is observed in the 15 nm GITT voltage curve. Similar observations were reported for 7 nm anatase particles and for micro-sized anatase at elevated temperature^{22,23}. This second plateau reflects a second phase transition between orthorhombic $\beta\text{-Li-titanate}$ and tetragonal Li_7TiO_2 ,^{16,24} reaching the theoretical capacity of anatase TiO_2 . Only particles smaller than 10 nm can be

converted to the tetragonal Li_xTiO_2 phase at room temperature^{16,25} unless the insertion proceeds at elevated temperatures.²⁶ This indicates that the formation of the Li_xTiO_2 phase is kinetically hindered, most likely forming at the first 3-4 nm of the surface of the particles, as also indicated by surface sensitive XAFS,²⁷ and can be only detected for very small particle sizes^{16,25}; (ii) The Li solubility limit of $\alpha\text{-Li}_{x\alpha}\text{TiO}_2$ anatase and $\beta\text{-Li-titanate}$, at which the voltage plateau starts and ends, increases with decreasing particle size as shown in Figure 3.1 consistent with previous studies^{11,16}. The distribution of larger voltages before the voltage plateau is reached that is observed for the smaller particles can be explained by the presence of surface sites having a lower energy, hence a higher voltage. A recent first principles study quantified the surface effects of Li intercalation in spinel lithium titanium oxides.²⁸ This study reveals that, depending on the surface orientation, the near surface region provides a distribution of surface sites resulting in a distribution of voltages. Consistent with the observation in the figure these sites are responsible for the curved voltage profile in nano Li insertion storage materials; (iii) The equilibrium voltage plateau decreases with decreasing particle size, as shown in the inset of Figure 3.1 (average value 1.82V for 130 nm, and 1.807V for 15nm). This small, but interesting experimental phenomenon can be attributed to the surface energy, which contributes increasingly in the thermodynamics upon particle size reduction.²⁹ Following the prediction of Van der Ven et al.³⁰ the increase of the plateau voltage with increasing particle size indicates that the surface energy of the $\beta\text{-Li-titanate}$ is larger than that of the $\alpha\text{-Li}_{x\alpha}\text{TiO}_2$ phase. It can also be explained by the capillary effects in nano-crystalline insertion materials formulated by Maier et al.,²⁹ predicting that upon particle size reduction the growing capillary pressure increases the chemical potential of the crystallite and thereby reducing the voltage versus Li/Li^+ .

3.3.2 In-situ x-ray diffraction measurements

The observed particle size dependent electrochemical behavior suggests that also the structural evolution may depend on the particle size. To study the particle size effect on the structural changes during the phase transformation from $\alpha\text{-Li}_{x\alpha}\text{TiO}_2$ to $\beta\text{-Li}$ -titanate upon lithiation, in-situ X-ray diffraction is performed for three particle sizes (130 nm, 41 nm and 15 nm).

To trace the details of the structural evolution a low discharge rate of C/120 was applied to the pristine anatase TiO_2 electrodes. Figure 3.2 shows the X-ray diffraction patterns of the different particle sizes TiO_2 anatase upon lithiation. As expected the $\beta\text{-Li}$ titanate phase develops at the expense of the $\alpha\text{-Li}_{x\alpha}\text{TiO}_2$ phase, consistent with previous studies.³¹⁻³⁴ Although the time evolution of the diffraction patterns appears visually very similar for the different particle sizes, analysis of the Rietveld refined structure parameters reveals a number of distinct differences which will be discussed in the following sections.

The evolution of domain size and phase fraction upon lithiation

Figure 3.3a-c shows the domain size evolution of both phases for the three different particle sizes resulting from Rietveld refinement, and assuming peak broadening is solely due to the domain size. In 130 nm particles the domain size of $\alpha\text{-Li}_{x\alpha}\text{TiO}_2$ decreases significantly upon lithiation (~30% decrease), while for smaller particles the decrease in $\alpha\text{-Li}_{x\alpha}\text{TiO}_2$ domain size is much less pronounced being 16% and 6.4% for 41 nm and 15 nm particles, respectively. In 130 nm particles the domain size of the newly forming $\beta\text{-Li}$ -titanate starts at ~ 100 nm at the very early stage of lithiation, and

gradually increases upon further lithiation. For the smaller particles (15 nm and 41 nm), the domain size of β -Li-titanate starts at a value even closer to the particle size and remains almost constant upon further lithiation. For all particle sizes, the maximum domain size of the β -Li-titanate phase is smaller than the pristine anatase particle size, even when the particles are completely transformed to the β -Li-titanate phase (at the end of discharge, the domain size of the β phase is 108 nm for 130 nm, 39 nm for 41 nm, 12 nm for 15 nm). We attribute this to a small amount of strain broadening in the β -Li-titanate phase, resulting in a slightly smaller apparent domain size, that may be the result of disorder on the Li-sub-lattice. The domain size evolution in 130 nm particles qualitatively follows the expected behavior, indicating that upon lithiation the Li-rich β phase grows at the expense of the Li-poor α phase within each particle.

However, smaller particle sizes display smaller changes in the domain size evolution, being practically constant for the smallest particle size (15 nm), see Figure 3.3a. This implies that smaller particles transform particle by particle, not allowing phase coexistence within a single crystallite, in contrast to the 130 nm particles where the domain size evolution indicates that the phases coexist. However, even in the 130 nm particles the growth of the β -Li-titanate phase is restricted as illustrated by the starting domain size, ~ 100 nm, which is close to the pristine particle size.

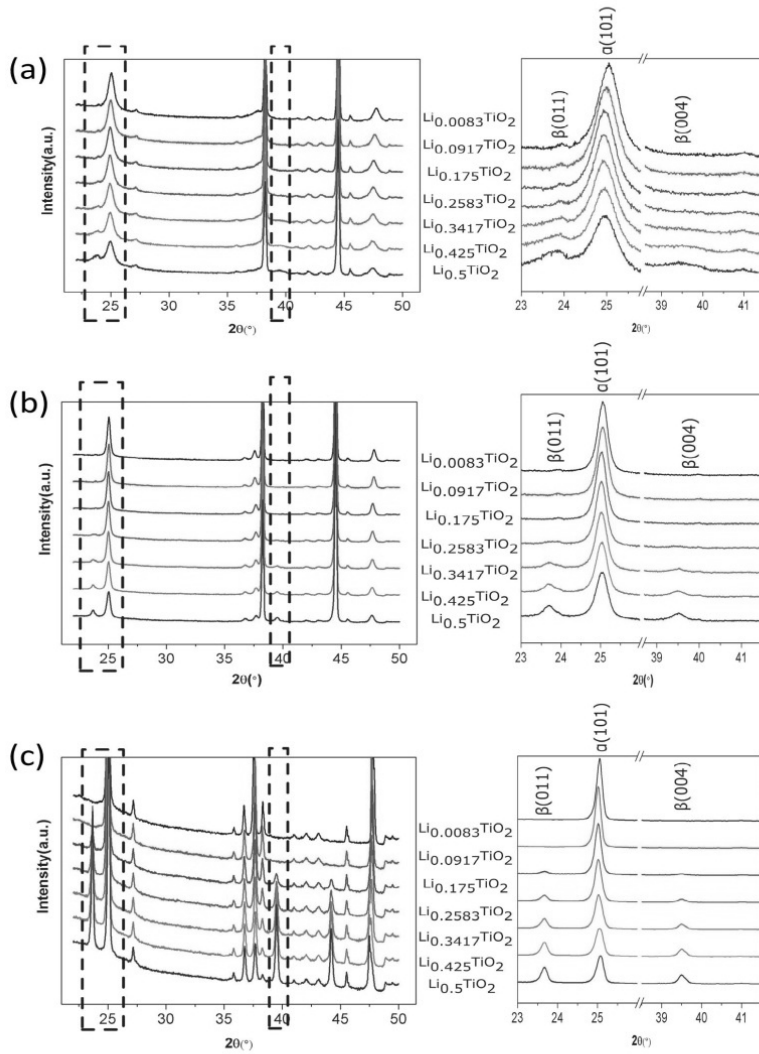


Figure 3.2. In-situ X-ray diffraction patterns of Li_xTiO_2 obtained at different states of first discharge for three particle sizes. (a) 15 nm; (b) 41 nm; (c) 130 nm.

To analyze this observation further we determined the number of β -Li-titanate nuclei as a function of the overall composition. Assuming that the β -Li-titanate phase grows as spherical domains in the anatase phase, and that the total volume of the active

material V_{total} remains constant, the number of β -Li-titanate nuclei N in the electrode can be estimated by the following equation:

$$N = \frac{PF_{\beta} \cdot V_{total}}{\frac{4}{3}\pi \left(\frac{r_{\beta}}{2}\right)^3} \quad \text{Equation 3.1}$$

Where PF_{β} is the β phase fraction and r_{β} is the domain size of β -Li-titanate, both of which are determined by the Rietveld refinement of the diffraction patterns. Figure 3.3d-f shows both the resulting number of β -Li-titanate nuclei and the β -Li-titanate phase fraction as a function of Li composition for the three particle sizes.

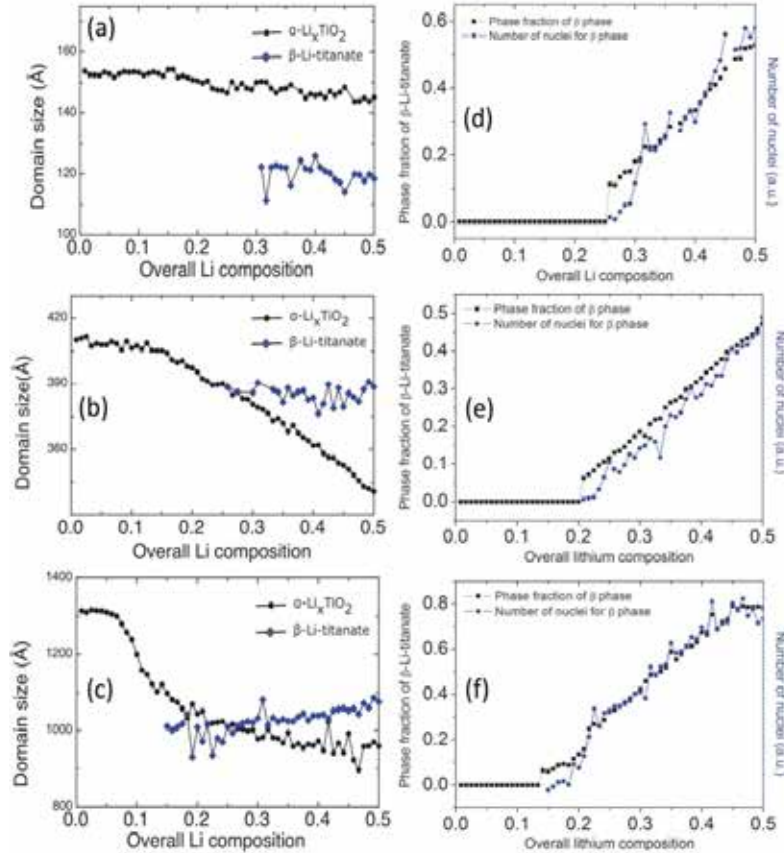


Figure 3.3. Domain size evolution of the two phases deduced from the in-situ X-ray diffraction line broadening as a function of overall lithium composition. (a) 15 nm; (b) 41 nm; (c) 130 nm. Comparison on the β phase fraction with the calculated number of β nuclei. (d) 15 nm; (e) 41 nm; (f) 130 nm

A linear increase of both the number of nuclei and the phase fraction with lithium fraction is observed for all particle sizes. This reveals that for all particle sizes the phase fraction of β -Li-titanate increases mainly via continuous nucleation of new particles rather than concurrent domain growth of the β -Li-titanate within the particles. The large initial domain size of the nucleating β -Li-titanate phase indicates that nucleation is followed by an instantaneous (on the time scale of the experiment) boundary movement. For small particles this results in an initial phase boundary movement that covers approximately the complete particle. This nucleation mechanism is sketched in Figure 3.4. This is consistent with our earlier finding that small particles avoid the presence of phase boundaries and consequently either have the α -anatase or the β -Li-titanate phase.¹⁶ Consistently, upon lithiation the phase fraction can only grow by nucleation in the multi-particle ensemble, rather than through phase boundary migration. Interestingly, increasing the particle size up to 130 nm does not fundamentally change this phase transition mechanism; the difference being that in the 130 nm particles the initial phase boundary movement, the growth of the β -Li-titanate phase, is smaller than the particle size resulting in phase coexistence. Apparently, the initial phase boundary movement is independent of the particle size, the origin of which is unclear at this stage. Upon further lithiation this is followed by growth of the β -Li-titanate phase until the complete particle is transformed. These results indicate that the observed size dependent phase transition mechanisms, single

domain particles for small particles and two phase coexistence for larger particles, is a consequence of the length scale of the initial phase boundary movement.

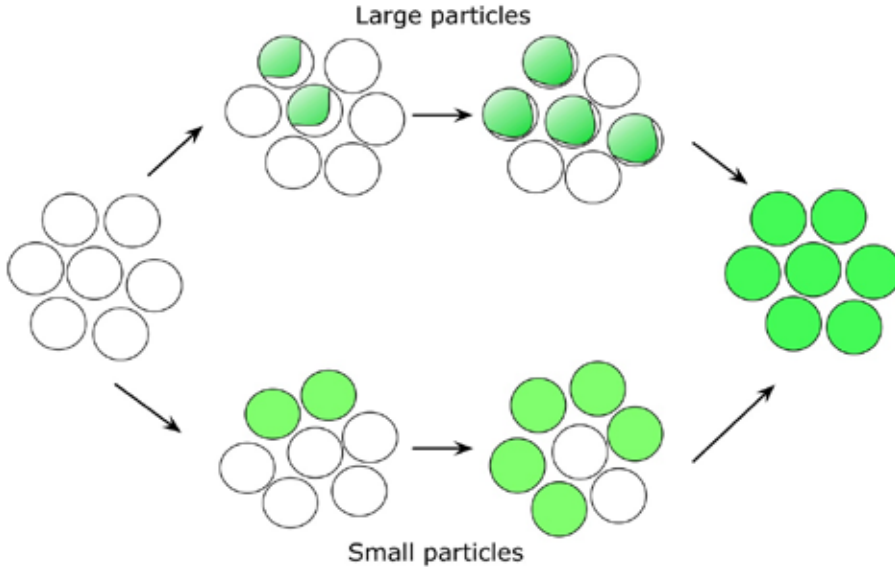


Figure 3.4. Schematic view of the sequential nucleation mechanism in TiO_2 electrodes during discharge for different particle sizes. White indicates the $\alpha\text{-Li}_x\text{TiO}_2$ phase and the green indicates the $\beta\text{-Li-titanate}$ phase.

Evolution of Li content upon lithiation

The evolution of the b -lattice parameters of the α and β phases for three particle sizes is presented in Figure 3.5a and 3.5b. Assuming the validity of Vegard's law, the Li content is linearly related to the changes in the b -lattice parameter and the real-time Li content of the $\alpha\text{-Li}_{x\alpha}\text{TiO}_2$ and $\beta\text{-Li-titanate}$ phases are deduced, as shown in Figure 3.5c and 3.5d. Compared to the unit cell volume, the b -lattice parameter ($a=b$ in the α phase due to the tetragonal symmetry) is more sensitive to the Li composition for the reason

that upon lithium ion insertion the Ti-O bonds are elongated and Ti-Ti bonds are shortened, which mainly affects the *b*-lattice parameter.⁶

Bulk thermodynamics of first order phase transitions predicts two stages in the evolution of the Li content. (i) In the single phase region, outside the miscibility gap the lithium content linearly increases with the overall composition and (ii) in the miscibility gap the two phases coexist and the lithium content remains constant. Indeed Figures 3.5c and 3.5d suggest the existence of two distinct stages in the evolution of the Li content in the α -Li_{x α} TiO₂ phase. (i) The first stage (below the solubility limit) displays an approximately linear increase of the Li content in α -Li_{x α} TiO₂ phase for all the three particle sizes. This represents the solid solution region before the first order phase transition sets in, consistent with bulk thermodynamics. (ii) In the second stage, an approximate constant Li content in the α phase is observed for 130 nm particles within the miscibility gap, also consistent with bulk thermodynamics. However, for the 41 nm and 15 nm particle sizes a significant increase in the Li content in the α -phase is observed in the miscibility gap.

Deviating even more from bulk thermodynamics is the evolution of the Li content in the β phase demonstrating a distinct increase of the Li content in β phase for all particle sizes. Least deviating from bulk thermodynamics is again the 130 nm particle size where the Li content in the β -Li-titanate starts at a value close to the expected bulk Li solubility limit reaching a constant solubility limit at slightly larger overall composition. However, for the 41 nm and 15 nm particles, an initial steep increase in Li content of β phase is observed, never reaching a constant value with increasing composition. Figure 3.5d also demonstrates that the steep increase in Li content of β phase is detected over a wider composition range in smaller particle sizes.

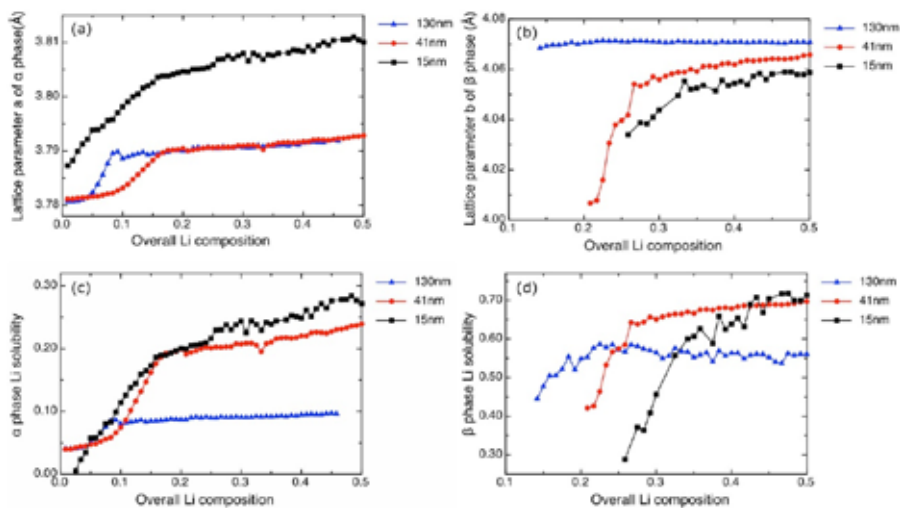


Figure 3.5(a) Lattice parameter a of α - $\text{Li}_{x\alpha}\text{TiO}_2$ as function of overall lithium composition for three particle sizes deduced from in-situ X-ray diffraction. (b) Lattice parameter b of β -Li-titanate as a function of overall lithium composition for three particle sizes deduced from in-situ X-ray diffraction. (c) lithium content of α phase as a function of overall Li composition deduced from the a -lattice parameters assuming Vegard's law for three particle sizes. (d) lithium content of β Phase as a function of overall Li composition deduced from the b -lattice parameters assuming Vegard's law for three particle sizes.

The observed increased Li solubility limits with decreasing particle size is consistent with the Li_xTiO_2 size-phase diagram determined previously.¹⁶ The dependence of the solubility limits on the overall composition, in particular observed for smaller particle sizes, is very similar to what was recently observed in LiFePO_4 .¹⁸ In LiFePO_4 this was explained by the size confinement of the lithium concentration gradient at the phase boundary (diffuse interface), which competes energetically favorable bulk compositions when particle sizes approach nano-dimensions. This leads to solubility limits that change when the phase boundary moves, and hence when the overall

composition is changed.¹⁸ However, as concluded from the largely absent domain size evolution of the β phase, Figure 3.3a-c, the phase fraction mainly increases due to the sequential nucleation of the β phase, during which the growth of the domain appears instant. Such instant domain size growth would lead to instant confinement of the diffuse interface, and hence an instant change in solubility limits and not the gradual change as observed in Figure 3.5d. We conclude that in addition to the diffusion interface confinement that may be partially responsible for the increase in lithium content, another mechanism must be present in TiO_2 anatase causing the large increase in solubility limits. A possible explanation for the observed change in lithium content is that the experiments proceed under non-equilibrium conditions, which at first appears as non-intuitive given the very low discharge rate applied (C/120). However, the instant phase boundary movement indicates an interface controlled rather than Li^+ ion diffusion controlled movement. This picture is consistent with a recent theoretical study on the thermodynamics and kinetics of lithiated anatase Li_xTiO_2 electrodes,³⁵ predicting that Li diffusion in the β phase is mainly parallel to the reaction front plane, suggesting that the Li ion diffusion between the two phases does not contribute to the growth of the β -Li-titanate phase. If the phase boundary movement is much faster than the supply of Li-ions due to diffusion, the local Li composition in the β phase will run behind the equilibrium value creating a non-equilibrium condition. Therefore, we suggest the material to be in a non-equilibrium condition in the concentration range where the lithium content in β Li-titanate increases steeply, namely $0.14 < x < 0.22$ for 130 nm, $0.20 < x < 0.26$ for 41 nm and $0.25 < x < 0.38$ for 15 nm. Upon further lithiation both phases reach their equilibrium Li-solubility values.

3.3.3 Proof of the existence of non-equilibrium transformation

Relaxation experiments were performed to prove the existence of a non-equilibrium condition in the phase transition mechanisms. For two particle sizes, 15 and 130 nm, cells were discharged at a C/120 rate to reach an overall composition and then start to rest. There are two criteria for the rest starting point determination: i) The peak of new phase (Li-titanate phase) must be clearly visible allowing the peak intensity evolution to be observed during the rest period. ii) The non-equilibrium condition is expected to occur before the Li content in Li-titanate phase reaches the equilibrium solubility limit as determined from Figure 3.5(b). Hence the starting time of the relaxation should be not later than the inflection point of Li content in Li-titanate phase. Based on these criteria $x=0.16$ for 130 nm and 0.34 for 15 nm were selected as starting point for the relaxation. After reaching these compositions the current was set to zero and in-situ X-ray diffraction was performed while relaxing towards equilibrium. If the non-equilibrium condition indeed exists at this composition, it is expected that the under-lithiated β -Li-titanate phase fraction should shrink and the α - $\text{Li}_{x\alpha}\text{TiO}_2$ phase fraction should grow during the relaxation period to be able to reach the equilibrium solid solution compositions. At the same time the solid solution in the β -Li-titanate phase should increase towards the equilibrium value, which should be reflected by the b -lattice parameter evolution. Based on the overall compositions at the start of the relaxation experiment, the equilibrium Li solubility limits indicate that in equilibrium the phase fractions of α and β phases should reach approximately 81% and 19% for 15nm, and 91% and 9% for 130nm particles, respectively. Figures 3.6a and 3.6b show the X-ray diffraction patterns in the beginning of discharge, when the discharge is stopped

and finally at the end of the relaxation. For both particle sizes the intensities of main reflections and the corresponding voltage reach a stasis after 15 hours (15nm) and 7 hours (130 nm). For both particle sizes the intensity of the β -Li-titanate Bragg reflections decrease as expected upon relaxation, and consistently the α -Li_xTiO₂ Bragg reflections grow. In particular, for 15 nm particles, the very small amount of β -Li-titanate (19%) is very difficult to detect by X-ray diffraction and almost disappears at the end of relaxation due to the large line broadening, as observed in Figure 3.6b. Applying Vegard's law to the *b*-lattice parameter of the α -Li_xTiO₂ and β -Li-titanate phases results in the expected evolution of the Li content towards the equilibrium values as observed in Figure 3.7a and 3.7b.

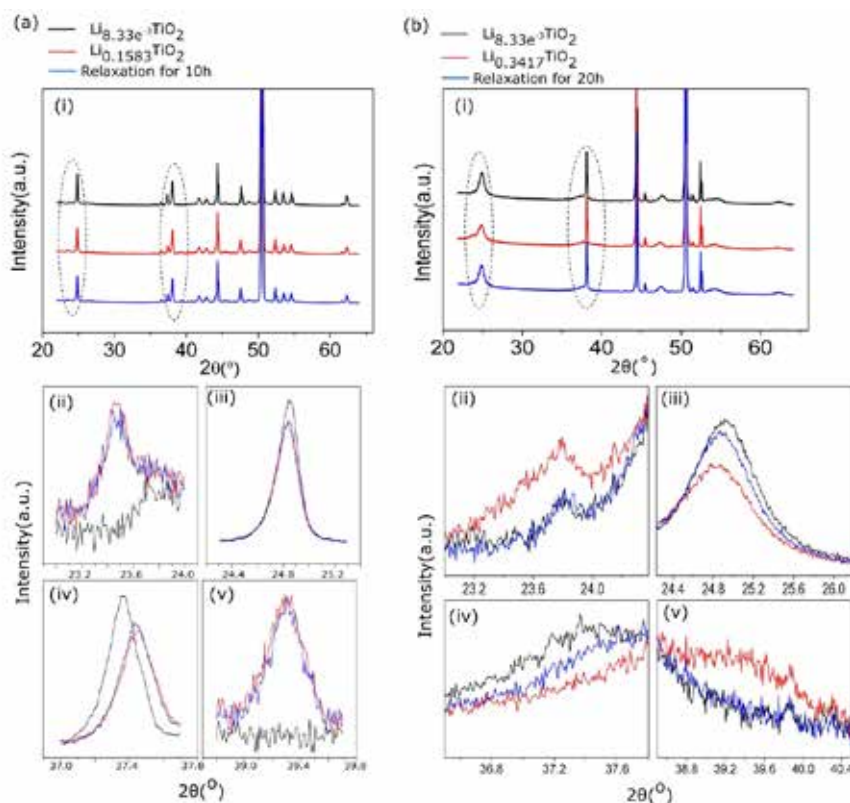


Figure 3.6. In-situ X-ray diffraction patterns of Li_xTiO_2 at different stages of discharge and relaxation (a) 130 nm and (b) 15 nm. In both Figure 3.6a and 3.6b, ii and v are Li-titanate phase, iii and iv are anatase phase. The black line represents the diffraction pattern at the initial stage of discharge ; the red line represents the last scan collected during discharge ($\text{Li}_{0.158333}\text{TiO}_2$ for 130 nm and $\text{Li}_{0.341667}\text{TiO}_2$ for 15 nm, deduced from the electrochemistry); the blue line is the scan collected when the cells stop discharge and relax for 10 hours (130 nm) and 20 hours (15 nm) respectively. In the bottom Figures the circled regions are enlarged showing the Li-titanate phase in ii and v and the anatase phase in iii and iv.

The relaxation experiments prove that the formation of the β phase proceeds under non-equilibrium conditions, even under very slow C/120 discharge conditions. The variation of the phase fractions during relaxation in the 15 nm particles is significantly larger compared to that in 130 nm particles, indicating that the 15 nm particle electrode is further out of equilibrium. This is in line with the larger Li content variations in smaller particles, which are observed in Figure 3.5, indicative for the non-equilibrium condition.

Based on the smaller diffusion distances it is against intuition that smaller particles are further away from their equilibrium condition, in particular at these very slow discharge rates. There are several explanations for this. (i) The main reason is the absence of phase coexistence within a single particle for the small particle sizes as opposed to larger particle sizes as illustrated by Figure 3.4. In larger particles intra particle transport (phase boundary movement) can reestablish the equilibrium conditions. However, the absence of phase coexistence in small particles infers that inter particle lithium transport and nucleation of the phase is required to reach the

equilibrium phase fractions and solid solution compositions. This is supported by the evolution of the domain sizes during the relaxation experiments, Figure 3.7a and 3.7b, where in 15 nm particles the domain sizes are constant whereas the anatase phase in micron particles displays a significant growth. The inter particle Li ion transport (transport over the electrode-electrolyte interface) and nucleation can be expected to require much more time³⁶ compared to intra particle transport.³⁷ (ii) Also the lower self-diffusion coefficients in smaller particle sizes, due to weaker interaction with the conduction electrons and a strongly concentration dependent diffusion coefficient³⁴, will slow down the establishment of equilibrium.

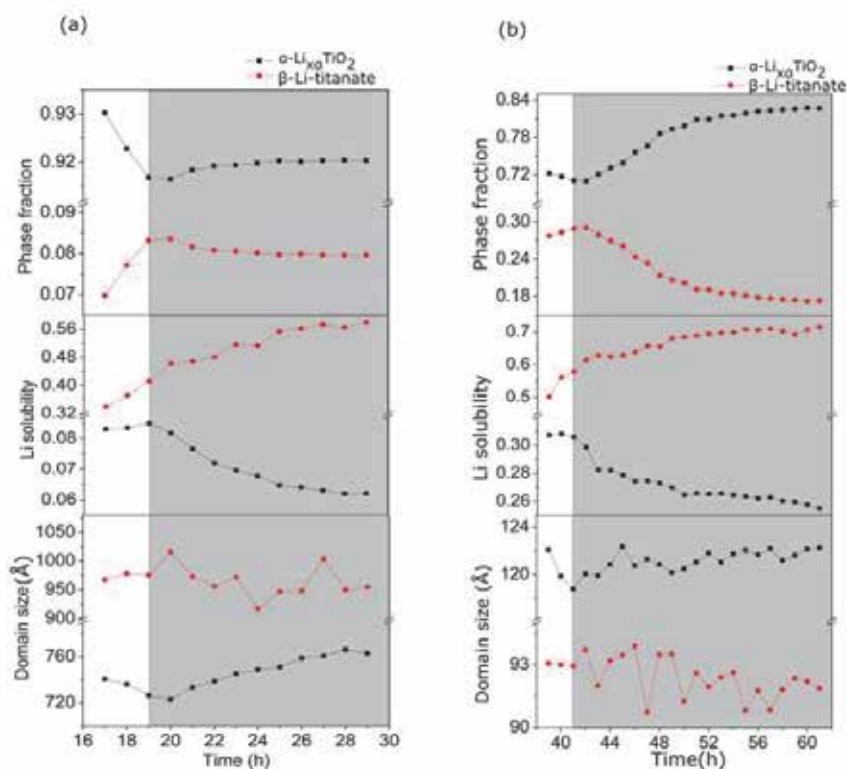


Figure 3.7. Results of Rietveld refinements of the in-situ XRD pattern collected during discharge and subsequent relaxation. (a) 130nm; (b) 15nm.

Other possible explanations include (iii) the higher solubility limit of the β phase for smaller particles and (iv) the formation of the Li_1TiO_2 phase. Starting at a specific overall composition, the larger lithium content in the β phase in smaller particles requires more Li-ion redistribution compared to larger particles. In addition, the Li_1TiO_2 phase observed in nanosized particles, is expected to form at the surface of the β -Li-titanate phase.²⁵ A small amount of Li_1TiO_2 at the β -Li-titanate surface will block further Li-ion insertion due to its poor reported Li-ion conductivity.^{16,25} Hence, it will take more time for the Li concentration in the β phase reaching its equilibrium value. A counter intuitive observation in Figure 3.7a is small phase fraction of the β phase (~ 0.08) yet having a larger domains size compared to the α phase, the latter constituting more than 90% of the total phase volume. This is the consequence of X-ray diffraction probing the average domain size of the α and β phases in all particles. For the α phase this includes the non reacted particles, for which the domain size is equal to the pristine particle size, and the small α phase domains in the reacted particles. The average of the latter leads to a smaller average particle size that the β phase in the reacted particles that covers almost the complete particles explaining the observation.

3.3.4 Summary of the phase transformation stages.

The phase transformation in anatase Li_xTiO_2 upon lithiation can be categorized into three stages, schematically illustrated in Figure 3.8. (i) The solid solution stage, during which the Li content in $\alpha\text{-Li}_{x\alpha}\text{TiO}_2$ increases until it reaches the solubility limit of $\alpha\text{-Li}_{x\alpha}\text{TiO}_2$ anatase phase, which depends on the particle size; (ii) The non-equilibrium

stage. In this stage, the β phase starts to form, and the migration of the α/β phase boundary is much faster than the diffusion of the Li-ions. Consequently, the Li concentration in the newly formed β phase is below the equilibrium value, causing the non-equilibrium conditions. Both the time-resolved Li content evolution upon lithiation and the relaxation experiments indicate that in smaller particles this leads to a larger deviation from equilibrium over a wider composition range. (iii) The final stage is the equilibrium phase transformation stage, during which the Li concentration in α and β phase equals the solubility limits and the diffusion-controlled equilibrium phase transformation proceeds in the electrode system until the whole particle is transformed.

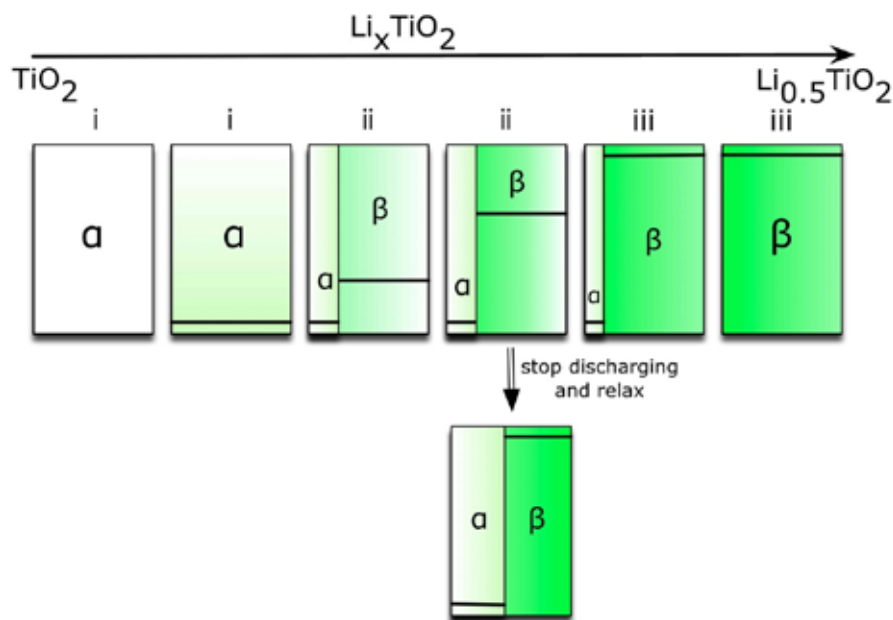


Figure 3.8. Schematic view of the phase transformation in Li_xTiO_2 upon lithiation. Roman numbers correspond to the phase transformation stages mentioned in the text; the blocks represent the individual reacted particles in the electrode. The vertical black

lines in the blocks represent the phase boundary; the distance between the horizontal black lines and the bottom of the blocks represent the Li concentration in the corresponding phase domain.

The observed non-equilibrium conditions in β - Li_xTiO_2 anatase appear to be the consequence of the interfacially-controlled phase boundary movement which is fast compared to the Li-ion diffusion in the solid state Li_xTiO_2 matrix. Interestingly, in olivine LiFePO_4 , the opposite phenomenon appears to take place as the phase transition lags behind due to the fast Li-ion diffusion.^{38,39} This fundamental difference in phase transformation behavior may be attributed to the differences in nucleation barrier and diffusion coefficient between anatase TiO_2 and olivine LiFePO_4 . According to classical nucleation theory, small interfacial energy γ and coherency strain energy E^{strain} will result in a small nucleation barrier ΔG^* .^{39,40} The experimental data of the interfacial energy and strain energy in TiO_2 anatase have not been reported, but they are estimated to be very small based on the suggested existence of a common plane between α - $\text{Li}_{x\alpha}\text{TiO}_2$ and β -Li-titanate with zero misfit strain.³⁵ This indicates that in TiO_2 anatase, nucleation is facile and phase boundary movement may be very fast compared to the relatively small self-diffusion coefficients that are in the order of 10^{-18} to $10^{-16} \text{ cm}^2/\text{s}$.³⁵ While for LiFePO_4 , the deduced from the interfacial energy⁴¹ $\gamma = 39 \text{ mJ}/\text{m}^2$ and strain energy $3200 \text{ J}/\text{mol}$, nucleation barrier is expected to be relatively high, of the order of hundreds kT at room temperature per cluster³⁹. It indicates much more difficult nucleation and phase boundary movement compared to TiO_2 . In addition, the diffusion coefficient for Li hopping in LiFePO_4 is theoretically estimated to be 10^{-8} to $10^{-7} \text{ cm}^2/\text{s}$ ⁴², several orders of magnitude larger than in Li_xTiO_2 (10^{-18} to $10^{-16} \text{ cm}^2/\text{s}$). The consequence is that in LiFePO_4 the nucleation of the first order phase transition will be

delayed with respect to the overall composition due to the fast diffusion,³⁸ or can be even avoided at high rates.^{39,43}

3.4 Conclusions

A systematical study is presented on the particle size dependent phase transformation behavior in anatase TiO_2 upon lithiation. The equilibrium voltage depends on the particle size rationalized by the surface energy contribution in the Li chemical potential of Li_xTiO_2 . The growing phase fraction of β -Li-titanate upon lithiation is mainly caused by the sequential nucleation of particles, rather than a phase reaction front movement within the particles. Remarkably, the size dependent evolution of the Li content in both phases upon lithiation indicates that the phase transition in anatase TiO_2 is a non-equilibrium process even at very slow discharge rates. This is rationalized by initially fast phase boundary movement of the Li-rich phase compared to the relatively slow Li-ion diffusion in the solid state. This is proven by relaxation experiments, which demonstrate the evolution of the phase fractions and Li content towards equilibrium. With these experiments the complex size dependent, non-equilibrium phase behavior in nanosized anatase TiO_2 is revealed. The absence of phase coexistence in smaller particles in combination with the sluggish ionic transport are the origin of the better electrochemical performance of nano structured as compared to micro sized anatase TiO_2 materials. It also suggests that strategies to improve the rate performance of anatase TiO_2 should concentrate on improving the interstitial diffusion, for instance by doping with Nb⁴⁴⁻⁴⁶ or Zn⁴⁷.

References

- (1) Bonino, F.; Busani, L.; Lazzari, M.; Manstretta, M.; Rivolta, B.; Scrosati, B. *Journal of power sources* **1981**, 6, 261–270.
- (2) Cava, R. J.; Murphy, D. W.; Zahurak, S.; Santoro, A.; Roth, R. S. *J. Solid State Chem.* **1984**, 53, 64–75.
- (3) Wagemaker, M.; Lützenkirchen-Hecht, D.; Keil, P.; van Well, A. A.; Frahm, R. *Physica B: Condensed Matter* **2003**, 336, 118–123.
- (4) Jamnik, J.; MAIER, J. *Phys. Chem. Chem. Phys.* **2003**, 5, 5215–5220.
- (5) Deng, D.; Kim, M. G.; Lee, J. Y.; Cho, J. *Energy & Environmental Science* **2009**, 2, 818–837.
- (6) Wagemaker, M.; Kearley, G. J.; Van Well, A. A.; Mutka, H.; Mulder, F. M. *J. AM. Chem. Soc.* **2003**, 125, 840–848.
- (7) Aricò, A. S.; Bruce, P.; Scrosati, B.; Tarascon, J.-M.; van Schalkwijk, W. *Nature Materials* **2005**, 4, 366–377.
- (8) Bruce, P. G.; Scrosati, B.; Tarascon, J.-M. *Angewandte Chemie-International Edition* **2008**, 47, 2930–2946.
- (9) MAIER, J. *Nature Materials* **2005**, 4, 805–815.
- (10) Kavan, L.; Grätzel, M.; Rathousky, J.; Zukal, A. *J. Electrochem. Soc.* **1996**, 143, 394–400.
- (11) Sudant, G.; Baudrin, E.; Larcher, D.; Tarascon, J.-M. *Journal of Materials Chemistry* **2005**, 15, 1263–1269.
- (12) Subramanian, V.; Karki, A.; Gnanasekar, K. I.; Eddy, F. P.; Rambabu, B. *Journal of power sources* **2006**, 159, 186–192.
- (13) Kubiak, P.; Froehlich, T.; Husing, N.; Hornmann, U.; Kaiser, U.; Schiller, R.; Weiss, C. K.; Landfester, K.; Wohlfahrt-Mehrens, M. *Small (Weinheim an der Bergstrasse, Germany)* **2011**, 7, 1690–1696.
- (14) Yamada, A.; Koizumi, H.; Nishimura, S.-I.; Sonoyama, N.; Kanno, R.; Yonemura, M.; Nakamura, T.; Kobayashi, Y. *Nature Materials* **2006**, 5, 357–360.
- (15) Kobayashi, G.; Nishimura, S.-I.; Park, M.-S.; Kanno, R.; Yashima, M.; Ida, T.; Yamada, A. *Advanced Functional Materials* **2009**, 19, 395–403.
- (16) Wagemaker, M.; Borghols, W. J. H.; Mulder, F. M. *Journal of the American Chemical Society* **2007**, 129, 4323–4327.
- (17) Burch, D.; Bazant, M. Z. *Nano Letters* **2009**, 9, 3795–3800.

- (18) Wagemaker, M.; Singh, D. P.; Borghols, W. J. H.; Lafont, U.; Haverkate, L.; Peterson, V. K.; Mulder, F. M. *Journal of the American Chemical Society* **2011**, *133*, 10222–10228.
- (19) Larson, A. C. GSAS; Los Alamos National Laboratory, 1994.
- (20) Toby, B. H. *Journal of Applied Crystallography* **2001**, *34*, 210–213.
- (21) Ohzuku, T.; Kodama, T.; Hirai, T. *J. Power Sources* **1985**, *14*, 153–166.
- (22) Zachau-Christiansen, B.; West, K.; Jacobsen, T.; Atlung, S. *Solid State Ionics* **1988**, *28-30*, 1176–1182.
- (23) Watson, B. J. M.; W, G. *Physical Review B* **2010**, *53-6*, 694–700.
- (24) Wagemaker, M.; Simon, D. R.; Kelder, E. M.; Schoonman, J.; Mulder, F. M. *Physica B: Condensed Matter* **2004**, *350*, E995–E998.
- (25) Borghols, W. J. H.; Lutzenkirchen-Hecht, D.; Haake, U.; van Eck, E. R. H.; Mulder, F. M.; Wagemaker, M. *Physical chemistry chemical physics : PCCP* **2009**, *11*, 5742.
- (26) Macklin, W. J.; Neat, R. J. *Solid State Ionics* **1992**, *53-56*, 694–700.
- (27) Wagemaker, M.; Lutzenkirchen-Hecht, D.; van Well, A. A.; Frahm, R. *J. Phys. Chem. B* **2004**, *108*, 12456–12464.
- (28) Ganapathy, S.; Wagemaker, M. *ACS NANO* **2012**, *6*, 8702–8712.
- (29) Maier, J. *Angewandte Chemie-International Edition* **2013**, *52*, 4998–5026.
- (30) Van der Ven, A.; Wagemaker, M. *Electrochemistry Communications* **2009**, *11*, 881–884.
- (31) Wagemaker, M.; van de Krol, R.; Kentgens, A. P. M.; Van Well, A. A.; Mulder, F. M. *Journal of the American Chemical Society* **2001**, *123*, 11454–11461.
- (32) Krol, R. V. D.; Goossens, A.; Meulenkaamp, E. A. *J. Electrochem. Soc.* **1999**, *146*, 3150–3154.
- (33) Murphy, D. W.; Cava, R. J.; Zahurak, S. M.; Santoro, A. *Solid State Ionics* **1983**, *9-10*, 413–417.
- (34) Wagemaker, M.; Borghols, W. J. H.; van Eck, E. R. H.; Kentgens, A. P. M.; Kearley, G. J.; Mulder, F. M. *Chemistry (Weinheim an der Bergstrasse, Germany)* **2007**, *13*, 2023–2028.
- (35) Belak, A. A.; Wang, Y.; Van der Ven, A. *Chemistry of Materials* **2012**, *24*, 2894–2898.
- (36) Ganapathy, S.; van Eck, E. R.; Kentgens, A. P.; Mulder, F. M.; Wagemaker, M. *Chemistry-a European Journal* **2011**, *17*, 14811–14816.
- (37) Wagemaker, M.; Kentgens, A. P. M.; Mulder, F. M. *Nature* **2002**, *418*, 397–399.
- (38) Sharma, N.; Guo, X.; Du, G.; Guo, Z.; Wang, J.; Wang, Z.; Peterson, V. K. *Journal of the American Chemical Society* **2012**, *134*, 7867–7873.

- (39) Malik, R.; Zhou, F.; Ceder, G. *Nature Materials* **2011**, *10*, 587–590.
- (40) Porter, D. A.; Easterling, K. E.; Sherif, M. Y. *Phase Transformation in Metals and Alloys*; 3rd ed.; CRC Press, 2009.
- (41) Cogswell, D. A.; Bazant, M. Z. *ACS NANO* **2012**, *6*, 2215–2225.
- (42) Morgan, D.; Van der Ven, A.; Ceder, G. *Electrochemical and Solid State Letters* **2004**, *7*, A30–A32.
- (43) Bai, P.; Cogswell, D. A.; Bazant, M. Z. *Nano Letters* **2011**, *11*, 4890–4896.
- (44) Sheppard, L. R.; Bak, T.; Nowotny, J. J. *Phys. Chem. B* **2006**, *110*, 22447–22454.
- (45) Archana, P. S.; Jose, R.; Jin, T. M.; Vijila, C.; Yusoff, M. M.; Ramakrishna, S. *Journal of the American Ceramic Society* **2010**, *93*, 4096–4102.
- (46) Fehse, M.; Cavaliere, S.; Lippens, P. E.; Savych, I.; Iadecola, A.; Monconduit, L.; Jones, D. J.; Rozière, J.; Fischer, F.; Tessier, C.; Stievano, L. *J. Phys. Chem. C* **2013**, *117*, 13827–13835.
- (47) Ali, Z.; Cha, S. N.; Sohn, J. I.; Shakir, I.; Yan, C.; Kim, J. M.; Kang, D. J. *Journal of Materials Chemistry* **2012**, *22*, 17625–17629.

Chapter 4

Thermodynamic study of Li intercalation into Li_xTiO_2

The role of surface orientation and particle size

Abstract

Using DFT first-principles calculations and applying a surface cluster expansions the impact of particle size and surface orientation on the lithium ion insertion in anatase TiO_2 is studied. The calculated formation energies for bulk and surface structures suggest that the energetic favorable Li sites in $\text{Li}_{0.5}\text{TiO}_2$ titanate phase depend significantly on the surface orientation. For Li compositions below $\text{Li}_{0.5}\text{TiO}_2$, the calculated equilibrium voltage curves upon Li-ion insertion have a good agreement with the experimental results. The results show that the difference in voltage between the different surface orientations is due to the Li-O and Ti-O bond length in the surface region. For Li compositions above $\text{Li}_{0.5}\text{TiO}_2$ the calculated voltages are not consistent with experimental observations, which is suggested to be the consequence of using stoichiometric surface slabs. The presence of excess oxygen at the surface termination results in a distinct increase of the intercalation voltage for small particles, consistent with experimental observations.

4.1 Introduction

Over the past two decades, nano-structured materials have been of great interest in the field of electrochemical energy storage owing to their potentially better properties such as energy and power density compared to their bulk equivalents^[1-3] The origin of the difference in storage properties between bulk and nanosized electrode materials is due to the changes in thermodynamic properties, i.e. miscibility gap,^[4-6] chemical potentials,^[7] and phase transition mechanism^[8].

In particular nano-structured anatase has been subjected to size dependent studies revealing significant changes in electrochemical and thermodynamic properties: (i) Nanosizing brings significant improvement in the capacity (reaching the theoretically maximum LiTiO_2 composition for nanostructured TiO_2 compared to $\text{Li}_{0.5}\text{TiO}_2$ for bulk TiO_2) due to formation of the LiTiO_2 phase suggested to occur at the near surface region^[8,9]; (ii) Nanosizing results in a curved open cell voltage profile with a much smaller plateau region in comparison with bulk materials, indicating a reduced miscibility gap^[5,7] and/or surface storage effects^[5] ^[6,10,11] (iii) The equilibrium voltage decreases progressively with the reduction of particle size, which is explained by the larger role of surface energies upon nanosizing^[12,13] (see chapter 3).

In addition to size, also the particle shape appears to be relevant for the electrochemical performance. Recent experimental studies show that the $\{001\}$ facets of anatase TiO_2 exhibit much better rate performance compared to the thermodynamically more stable $\{101\}$ facets.^[14]

Aiming at understanding of these particle size and shape dependent properties, a first principles study of the surface effect on the thermodynamic properties of lithiated anatase TiO_2 is presented. Nanosized TiO_2 is modeled by surface slabs with the two most stable surface orientations $\{101\}$ and $\{001\}$ applying periodic boundary conditions. The phase stability is compared between different Li arrangements in nanosized and bulk TiO_2 anatase as function

of composition. This achieved by applying a cluster expansion fit to a finite number of formation energies determined by DFT calculations. Based on the cluster expansion fit the lithium configuration and composition can be determined given a fixed chemical potential and temperature as implemented in Monte Carlo simulations. In this way the impact of the surface on the Li-ion insertion is investigated by first-principle calculations.

4.2 Methods

The energies of the different Li configurations were minimized to the ground state by fully relaxing the atomic positions, unit cell dimensions and shape in the gradient-corrected exchange correlation functional (GGA) approximation in density functional theory calculations as implemented in the plane wave code VASP. A cut-off energy of 400 eV was chosen for the energy calculation. In order to ensure the total energies converged within 10^{-4} eV per formula unit, we used a $5 \times 7 \times 1$ k-point mesh for the (101) surface slab, and $7 \times 3 \times 1$ k-point mesh for (001) surface slab. For the supercell configurations, the k-point meshes were automatically transformed to ensure an equivalent density in reciprocal space as for the unit cell of the corresponding slabs. All calculations were performed non-magnetically because spin polarized calculations introduce negligible changes in the energies.

In order to determine the phase stability of different phases at a finite temperature, accurate free energies are required of all Li-vacancy configurations over the octahedral interstitial sites of anatase TiO_2 . In this study, we neglect the entropy contribution from lattice vibrations and electronic excitations, and only consider the configurational degree of freedom associated with Li-vacancy configurations. The cluster expansion approach is a powerful tool to construct an accurate extrapolation of the total energy of any possible Li-vacancy configuration in the system based on first principle energy calculation of relatively few ordered configurations. We

constructed cluster expansions for Li configurations for {101} two unit cell slabs and {001} two unit cell slabs to describe the configuration dependence of ground state energies over the Li concentration between 0 and 1. The occupation variables are assigned to be +1 or 0 when the site is occupied by Li or vacant respectively. Subsequently, the configuration freedom can be described by cluster functions defined as the products of occupation variables. In principle, the cluster functions are capable of describing all the possible configurations in the host system based on a complete and orthonormal basis in the configuration space. Finally the configurational energy is rigorously expanded in terms of these cluster functions.

$$E(\vec{\sigma}) = C_0 + \sum_{\alpha} C_{\alpha} \phi_{\alpha}(\vec{\sigma}) \quad \text{Equation 4.1}$$

Where the coefficient C_0 and C_{α} is the Effective Cluster Interactions (ECI), which are a series of constants to describe the dependence of the energy of a specific structure on the Li-configurations. In practice, the equation can be truncated by neglecting contributions from larger, less frequent occurring clusters. Therefore a restricted set of ECI coefficients is fitted to the energies of 84 bulk, 142 {101} and 138 {001} Li configurations determined by DFT. This makes it possible to rapidly evaluate the total energy of any Li configuration in the host within a good approximation, as is required to determine the thermodynamics of Li insertion. For the fit, the root mean square deviation from the DFT energies is 56 meV for bulk Li_xTiO_2 , 30 meV for the {101} direction and 60 meV for the {001} direction per TiO_2 formula unit.

Thermodynamic properties at finite temperatures (such as free energy, chemical potential, and the phase diagram) are predicted by applying Monte Carlo simulations on the cluster expansion as described in chapter 2. For the bulk and both surface orientations, we used a 6x6x6 supercell for the Monte Carlo simulations. For each temperature and chemical potential, 500 Monte Carlo passes are performed, the first 100 of which are equilibration steps performed before averaging.

4.3 Result and discussion

4.3.1 Surface termination

Previous first-principle studies on surface energies, reveal that the Wulff shape of TiO_2 anatase exists two facet orientations $\{001\}$ and $\{101\}$ ^[15]. More than 94% of the Wulff shape comprises the $\{101\}$ facet consistent with the experimental observations^[16](see figure 4.1) .

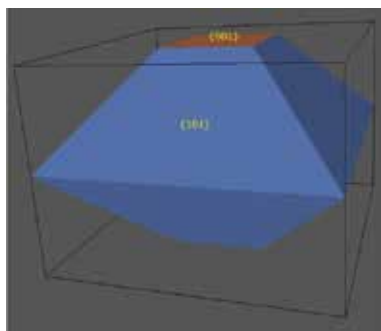


Figure 4.1 the wulff shape of TiO_2 anatase crystal, based on the calculated surface energy data from ref. [15]

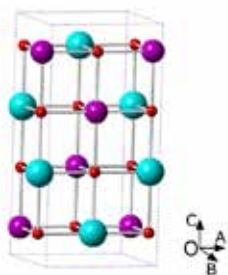


Figure 4.2 The structure of the tetragonal LiTiO_2 unit cell. Light blue atoms are lithium, red atoms are oxygen, and purple atoms are titanium.

Figure 4.2 shows the fully relaxed LiTiO_2 anatase structure, with lattice parameters $a=b=4.074\text{\AA}$, $c=8.498\text{\AA}$, which differ 1% from the experimental values^[9]. For a given Miller index, the surface

structures are constructed by cleaving the fully relaxed LiTiO_2 anatase. The surface termination is determined by the following criteria. i) the stoichiometry should be preserved after cleaving. For both $\{101\}$ and $\{001\}$ surfaces, the stoichiometry is always preserved in a slab having twice the thickness of a unit cell, independent of the position of the surface termination; ii) The stacking of the Ti-O plane should be symmetrical with respect to a plane parallel to the slab positioned in the middle of the slab^[4]. Thereby, the surfaces on both sides of the slab are equivalent. The surface terminations that meet this criteria belong to “type 2” according to the definition from Tasker,^[17] which have no dipole moment along the normal direction of the surface.

Based on the above two criteria, the number of potential planes for the surface termination is significantly reduced. For the $\{101\}$ orientation, both surface termination planes $(0.5, y, z)$ and $(0, y, z)$ meet the above criteria (see Figure 4.3a and b respectively), the difference being that the $(0.5, y, z)$ plane breaks 2 Li-O bonds and one Ti-O_6 octahedra while the $(0, y, z)$ plane breaks five Ti-O octahedra. The surface structure cleaved at $(0.5, y, z)$ is expected to give a lower surface energy^[4], which is confirmed by the calculation results, and is therefore selected. Applying the same criteria for the $\{001\}$ orientation leads to one possible surface termination due to the tetragonal symmetry in this direction, as shown in figure 4.3.

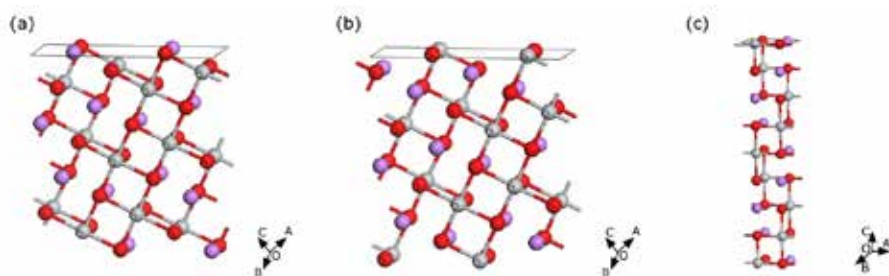


Figure 4.3 (a) and (b) The two possible surface terminations of relaxed structures of bulk LiTiO_2 along the $\{101\}$ direction; (c) The only possible surface termination of the relaxed structure of bulk LiTiO_2 along the $\{001\}$ direction. Purple atoms represent lithium, red oxygen and grey titanium.

With the selected surface terminations thin periodic slabs are built by introducing a vacuum layer (20 Å) to eliminate the spurious interaction between the repeated slabs in the periodic models.

In principle, the thickness of the atomic layers should be determined by the convergence test on the surface energies. However, since the surface cluster expansion will be applied on the slabs in the subsequent step, the total number of possible Li-vacancy configurations should be restricted to a practical amount. Under this criterion, the maximum number of the repeated unit cells is 2 for the {101} direction and 1 for the {001} direction. For both orientations, the lattice parameters of the cells are fixed while all atoms in the slab are allowed to relax due to the limited thickness of the atomic layers, see Figure 4.4.

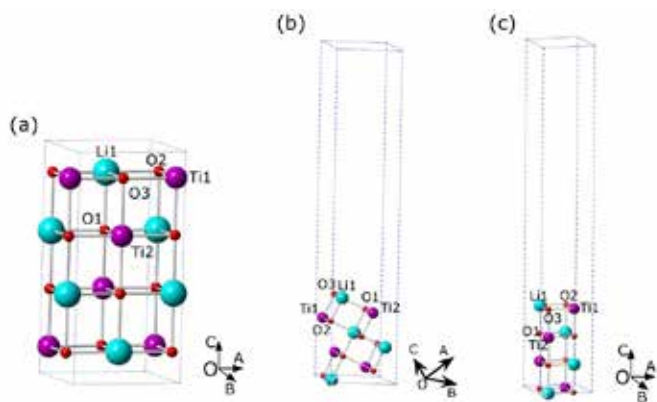


Figure 4.4 Fully relaxed structures that serve as the primitive cells for the surface cluster expansion. (a) bulk LiTiO_2 anatase. (b) {101} LiTiO_2 anatase surface slab. (c) {001} of LiTiO_2 anatase surface slab.

To compare the stability of the different Li-vacancy configurations over the octahedral Li interstitial sites of Li_xTiO_2 anatase the surface cluster expansion is performed for both the {101} and {001} slabs. In addition, the bulk cluster expansion of Li_xTiO_2 anatase is also performed,

the results of which are consistent with published work from Belak et al.^[18] The latter work demonstrates that for bulk TiO₂ anatase the single unit cell does not represent the energetics of the system correctly due to the high symmetry.^[18,19] Therefore, the maximum primitive cell for the surface cluster expansions is also chosen to be a double unit cell in the a and b directions, while for the bulk cluster expansion, doubling the unit cell in three dimensions was applied.

4.3.2 Formation energy

For bulk and the two surface orientations the formation energies of all the symmetry inequivalent Li-vacancies configurations are calculated using DFT. As for bulk anatase^[5,6,18,20], a strong long-range interaction was found in the initial stage of Li intercalation into the TiO₂ anatase surface slabs. Therefore, it is necessary to include Li configurations at dilute compositions into the phase stability comparison (For {101} at Li_{0.0625}TiO₂ and for {001} at Li_{0.03125}TiO₂ and Li_{0.0625}TiO₂). This determines the maximum cluster size in the expansion used.

The formation energy of different Li configurations referenced to the energies of the empty (TiO₂) and fully occupied (LiTiO₂) slabs are shown in Figure 4.5. The convex hull was constructed by connecting the configurations with the lowest formation energies. The formation energy calculation of bulk Li_xTiO₂ confirms the stability of the specific Li ordering at Li_{0.5}TiO₂ composition (see figure 4.6a), which has been recently.^[18,19] This configuration is characterized by edge-sharing pairs of LiO₆ octahedra, which is indicated by the translucent blue octahedra in the center of the structure shown in Figure 4.5(a). Also the surface slabs with the {101} and {001} orientations display the lowest formation energy for the Li_{0.5}TiO₂ composition,^[7,18,19] but different Li configuration was observed in {101} surface slab.

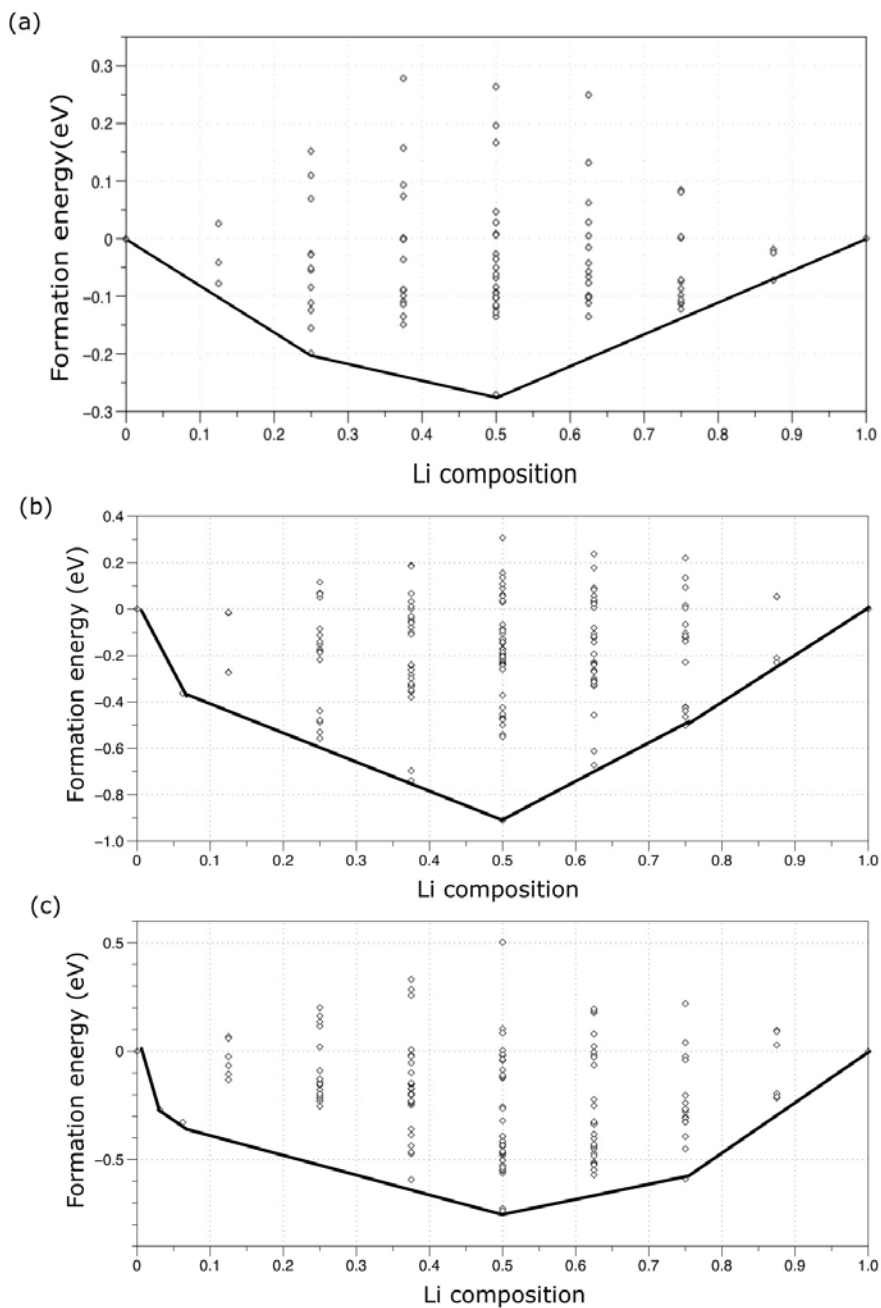


Figure 4.5 (a) The formation energy based on the VASP calculations of different Li-vacancy configurations over the octahedral sites of Li_xTiO_2 in (a) bulk anatase, (b) $\{101\}$ surface slab, and (c) the $\{001\}$ surface slab.

Figure 4.6(b) shows surface slabs of various Li-vacancy configurations in the 1×1 and $2\times 1\times 1$ supercell of $\text{Li}_{0.5}\text{TiO}_2$ along the $\{101\}$ direction with increasing formation energies. The structure xxii, in which all Li atoms are located in the center of the slab, has the highest formation energy, while the structure i, with all Li at surface layers has the lowest formation energy. This indicates that the $\text{Li}_{0.5}\text{TiO}_2$ $\{101\}$ surface slab is most stable segregation of Li ions into surface layers in such a way that the Li ions are two-fold coordinated to oxygen atoms by Coulomb interaction. In the most stable $\text{Li}_{0.5}\text{TiO}_2$ $\{101\}$ surface configuration along the $\{101\}$ direction, the fully coordinated Ti_i and O_2 display the most distinct outward relaxation, also observed in the $\{101\}$ surface structure of pure TiO_2 anatase^[8,15]. This triggers shorter Ti-O and Li-O bond lengths along the surface normal and a larger angle of the O-Ti-O and O-Li-O bonds. Furthermore, the four-fold coordinated Li_i moves inward by 0.044 Å resulting in a larger angle of the O-Li-O bond (107.08°).

For the $\{001\}$ orientation the two similar configurations at $\text{Li}_{0.5}\text{TiO}_2$, shown in Figure 4.6(c), have a comparable lowest formation energy. These two configurations have a similar Li-vacancy ordering as compared to the bulk ordered $\text{Li}_{0.5}\text{TiO}_2$ phase as predicted by Belak^[18] and Morgan.^[19] In the $2\times 1\times 1$ super cell of this configuration one Li ion resides in every OAOB plane. This allows paired Li ions to be located in adjacent edge sharing O6 octahedra, resulting in an energy favorable Li-O coordination^[19].

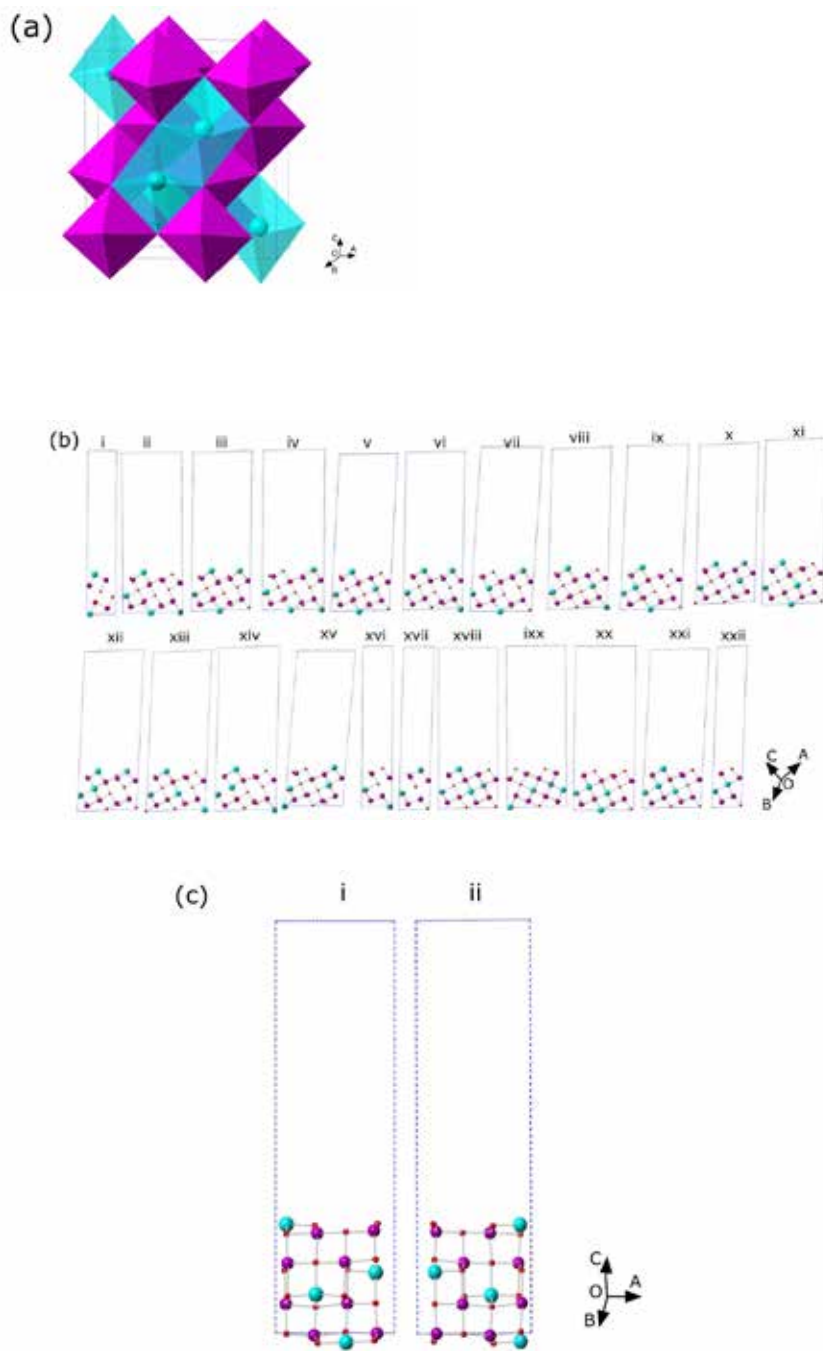


Figure 4.6. (a) The ordered Li configuration of the $\text{Li}_{0.5}\text{TiO}_2$ compositions having the lowest formation energy. (b) Li configurations in the $\{101\}$ slab with increasing formation energies from

left to right. (c) The two Li configurations in the {001} slab with increasing formation energies from left to right. Lithium atoms and lithium octahedra: light blue, oxygen atoms: red, titanium atoms and titanium octahedra: purple. In (a) oxygen atoms are not displayed for clarity.

Because only one Ti-O and one Li-O bond are interrupted by the vacuum layers, the Li-O Coulomb interaction between the adjacent Li octahedra's plays a dominant role in the phase stability^[14,19]. However, the discontinuity of the crystal structure caused by the vacuum still has influence on the atomic relaxation. Compared with the Li-ordered phase of $\text{Li}_{0.5}\text{TiO}_2$ in bulk anatase, the five-fold coordinated Li at the surface layer of the {001} surface structure displays less contraction along $\langle 010 \rangle$ direction and more expansion along $\langle 001 \rangle$ direction in the Li-O distance, which is due to the outward relaxation of the under-coordinated Li ions. This leads to a larger Li-Li distance between the neighboring Li occupied octahedra in the {001} surface structure. To counteract such Li-Li expansion, similar as the bulk $\text{Li}_{0.5}\text{TiO}_2$ ordered phase^[15,19], the Li-O bonds for the fully coordinated Li along both $\langle 010 \rangle$ and $\langle 001 \rangle$ undergo contraction, but change less. The finding that the two most stable {001} $\text{Li}_{0.5}\text{TiO}_2$ configurations have a comparable formation energy indicates that the Li arrangement has a marginal impact on the magnitude of formation energy. This may indicate that in practice the Li arrangement may be disordered in the {001} surface slab. For compositions $x < 0.5$ in Li_xTiO_2 only the dilute composition $x = 0.0625$ is located on the convex hull for both surface orientations {101} and {001}. This suggests that for compositions between $x = 0.0625$ and 0.5 the formation energy can be minimized by phase separating into the dilute composition $\text{Li}_{0.0625}\text{TiO}_2$ and the $\text{Li}_{0.5}\text{TiO}_2$ titanate structures. For Li composition compositions $x > 0.5$ in Li_xTiO_2 , additional ground state structures are identified at $x = 0.75$, again for both {101} and {001} surface orientations. The $\text{Li}_{0.75}\text{TiO}_2$ {101} ground state is realized by adding one Li ion in each middle layer (the 2nd and 3rd layers) of the ground state $\text{Li}_{0.5}\text{TiO}_2$ {101} surface slab, while the $\text{Li}_{0.75}\text{TiO}_2$ {001} ground state is realized by adding one Li ion in each surface layers (the 1st and 4th layers) of the ground state

$\text{Li}_{0.5}\text{TiO}_2$ {001} structure. As a consequence, the ground state structures of the $\text{Li}_{0.75}\text{TiO}_2$ slabs in {101} and {001} directions have very similar Li arrangements.

4.3.3 Voltage comparison

The first approach to predict the voltage profile is to use the differences between the ground state structures positioned on the convex hull referenced to metallic Li^[16,21]. This implies that entropy contributions are neglected resulting in a 0 K voltage profile. Calculated voltage profiles for both bulk and the Li_xTiO_2 surface slabs are shown in Figure 4.7 (a). With the temperature increasing, the configurational entropy arising from long or short range disorder of lithium ions cannot be disregarded. To model this a cluster expansion is performed on bulk and surface slab configurations providing an effective approach to parameterize the dependence of the Free energy on the site disorder. Using a Monte Carlo approach the Free energy of the possible configurations can be evaluated at each chemical potential, which reference to Li-metal gives the voltage profile. The cluster expansion based calculated voltage profiles at 10 K and 300 K are shown in figure 4.6 (b) and 4.6 (c) The dilute structures could not be fitted accurately in the cluster expansion, leading to the absence of the fast drop of the voltage curve in the low Li composition range. This is responsible for the appearance of small voltage steps at $x = 0.25$ at 10K representing the relative stability of these ordered phases in the bulk and the surface slabs. With increasing temperature the shape of voltage the small distinct steps are smoothened.

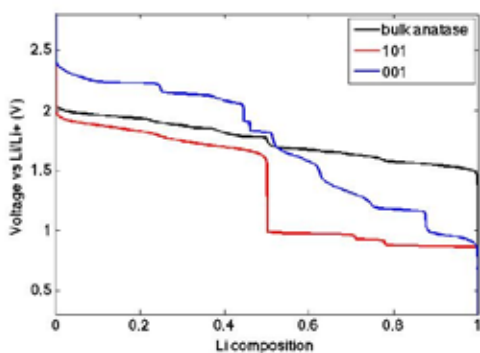
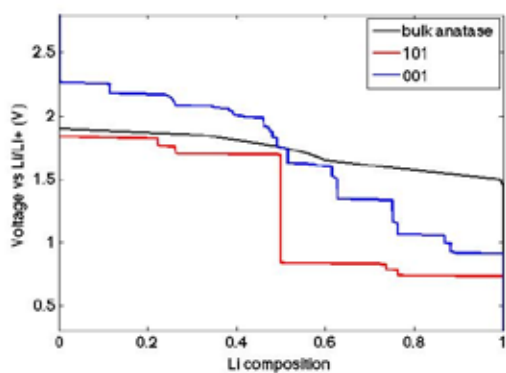
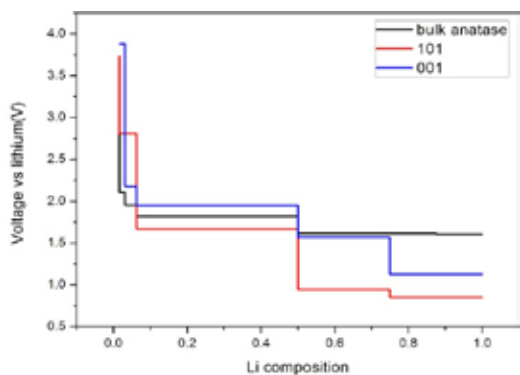


Figure 4.7 (a) The calculated voltage profile based on the ground state energies as a function of lithium composition for both surface slabs and bulk anatase; the calculated voltage profile based on the Monte Carlo cluster expansion simulation vs lithium composition at (b)10k and (c)300k

The surface slabs not only allow to study the influence of surface orientation on the equilibrium intercalation voltage, it also gives insight in the impact of particle size on the lithium insertion in anatase TiO_2 . Being the most dominating facet of the equilibrium TiO_2 anatase (more than 94% according to Wulff construction^[9,15,22]), the {101} surface slab properties will increasingly become apparent with decreasing particle sizes.

As indicated above the voltage calculation based on the cluster expansion does is unable to represent the energetics at dilute concentrations. For this reason we focus on the voltage curve based on the ground state energies (Figure 4.5) as shown in Figure 4.7 (a).

The evolution of the voltage with composition in Figure 4.7 (a) can be divided into three stages:

i) $0 < x < 0.0625$. The dilute composition region where both surface orientations {001} and {101} display a higher voltage compared to that of bulk anatase. This is consistent with GITT experimental findings where it was observed that smaller particles have slightly higher voltage at dilute lithium compositions (Figure 3.1, Chapter three). The origin of this is the lower energy of lithium sites at the surface allowing more relaxation compared to bulk sites, initiating the lithiation at the surface.^[10]

ii) $0.0625 < x < 0.5$. The absence of ground states outside the convex hull in this composition range for bulk and surface slabs results in a constant voltage plateau, reflecting the well-known phase transition from tetragonal lithium poor Li_xTiO_2 to the orthorhombic $\text{Li}_{0.5}\text{TiO}_2$ Li-titanate phase. The larger voltage calculated for bulk anatase compared to the 6 Å {101} surface slab is qualitatively in a good agreement with GITT measurements (see chapter 3). The atomic structures of the $\text{Li}_{0.5}\text{TiO}_2$ compositions in bulk, the {101} slab, and in the {001} slab relax during the DFT calculations such that the Li-O and Ti-O bond length of the Li and adjacent Ti occupied octahedras have a linear relationship with the voltage, as observed when comparing Figure 4.6 (a) with Table 1.

Table 1 Bond length variation within the ground state relaxed structures at the composition of $\text{Li}_{0.5}\text{TiO}_2$ of bulk, {101} surface and {001} surface. Atom labels refer to Figure 3.

Bond	Bond length bulk(Å)	Bond length {101}(Å)	Bond length {001}(Å)
Li1-O1	2.614	2.059	3.112
Ti1-O3	2.063	2.036	2.184
Ti1-O2	1.963	2.004	1.951
Ti2-O1	1.964	2.03	1.943

iii) $0.5 < x < 1$. Additional voltage steps are observed at $x = 0.75$ for both surface slabs, caused by the ground state at this composition. In this stage, both the {101} and {001} surface slabs have a lower voltage than the bulk structure up to the end composition LiTiO_2 . This calculation result indicates that the LiTiO_2 phase is thermodynamically more stable to form in bulk compared to the surface of the {101} surface slab. This is in contrast to what has been suggested based on experiments where the LiTiO_2 was suggested to occur at the surface of nano sized particles.^[4,8,9] Moreover, although with large kinetic barriers to reach equilibrium also in chapter three higher Li insertion potentials are found for smaller particles at the composition range of $0.5 < x < 1$, as shown in figure 3.1.

A potential explanation of this discrepancy may be the influence of the surface termination on the surface energetics of the surface slabs. As described above, the lowest surface energy was found for the {101} TiO_2 anatase surface slab with a corrugated oxygen-rich arrangement (see figure 4.4 (b)). It suggests that oxygen contributes to the stability of the surface, leading to lower energy and hence higher voltage according to the Nernst equation, which is also confirmed by a recent theoretical study in the surface lithium insertion into spinel $\text{Li}_4\text{Ti}_5\text{O}_{12}$.^[10]

Further, oxygen addition at this surface is possible at the under-coordinated Ti atoms (Ti_2) exposed to vacuum. Adding oxygen at these surface sites results in a large increase in voltage of 4.4 V vs Li/Li^+ for the $\text{Li}_4\text{Ti}_4\text{O}_{10}$ composition of the {101} surface slab. The origin of this excessively high voltage may be the large over stoichiometry resulting from the oxygen addition at the surface slabs ($\text{Li}_4\text{Ti}_4\text{O}_{10}$ versus $\text{Li}_4\text{Ti}_4\text{O}_8$). To model smaller over stoichiometry cell thicker {101} surface slabs were constructed (approximately 6.5 Å versus 20 Å). This results in an over stoichiometry of $\text{Li}_{48}\text{Ti}_{48}\text{O}_{104}$ versus stoichiometric $\text{Li}_{48}\text{Ti}_{48}\text{O}_{96}$ and an insertion voltage of 1.918 V, indeed smaller than for over stoichiometric $\text{Li}_4\text{Ti}_4\text{O}_{10}$ but still larger than the experimentally observed result of approximately 1.5 V in chapter 3. This indicates that even thicker surface slabs, comparable to the experimental particle sizes, which becomes computationally challenging, may result in a voltage larger than the bulk insertion voltage in closer agreement with the experimental results. At present we conclude that the oxygen termination may be responsible for the larger stability of the LiTiO_2 composition at the {101} surface potentially explaining the observed larger Li insertion voltage for smaller particles (Figure 3.1, chapter 3) In addition as the voltage at LiTiO_2 is increasing the oxygen over stoichiometry will also lead to distinct rise on the voltage at the second stage ($0.0625 < x < 0.5$), which has risen to 1.918V for {101} $\text{Li}_{48}\text{Ti}_{48}\text{O}_{104}$ surface slab.

To neutralize the charge from the over stoichiometric oxygen, extra Li capacity will be produced. With the higher voltage at the low Li content region (1st stage) more preferable Li sites are created at such composition region than after the voltage plateau starts (the 2nd and 3rd stage). Furthermore, the proportion of the excess Li should increase when the particles become smaller due to the larger over stoichiometry ($\text{Li}_{1+0.333}\text{Ti}_1\text{O}_{2+0.1667}$ for 20Å cell, $\text{Li}_{1+1}\text{Ti}_1\text{O}_{2+0.5}$ for 6.5Å cell). Therefore, the voltage plateaus are expected to shift towards higher Li composition with particle size decreasing, which has a good agreement with the previous investigation ^[2,7] and the evolution of the equilibrium for different particle sizes studied in chapter three.

In addition, kinetic factors may play a role in the LiTiO_2 phase formation in nano Li_xTiO_2 particles. Experimental^[8,9] and theoretical studies^[18] indicate that the formation of the LiTiO_2 phase at the surface of the particles hinders Li-ion diffusion, as discussed in Chapter 3. Thermodynamically, bulk Li_xTiO_2 particles may be able to convert completely to the LiTiO_2 phase, but the poor diffusivity through the LiTiO_2 could limit the transformation to the a few nanometer at the surface of the particles.^[18] In nano the materials this leads to a detectable fraction of LiTiO_2 , however, in bulk material the fraction of the few nanometer LiTiO_2 surface layers is difficult to detect.

4.4 Conclusions

In this chapter the Li intercalation in bulk and surface structures of Li_xTiO_2 are systematically investigated by DFT and thermodynamic calculations. We find that i) the formation energy of all symmetry non-equivalent Li configurations in both $\{101\}$ and $\{001\}$ surface orientations is minimal at $x=0.5$. The Li configuration of the ground state structures of the $\{001\}$ surface at $x=0.5$ are similar to that in bulk $\text{Li}_{0.5}\text{TiO}_2$. In contrast, for the $\{101\}$ surface, segregation of Li ions is predicted at the surface, which is attributed to the under coordinated oxygen enrichment in the surface layers. ii) The difference in voltage, based on the ground state formation energies, between bulk and the surface slabs, assuming the latter is representative for nano-sized materials, is qualitatively consistent with experimental observations. The origin for this phenomenon is the Li-O and Ti-O distances in the surface layers. iii) When the Li composition exceeds $\text{Li}_{0.5}\text{TiO}_2$, the calculations qualitatively deviate from experimental observations. The DFT prediction is that the formation of the LiTiO_2 is favorable in bulk anatase, rather than at the surface. To reconcile the experimentally observed higher potentials for smaller particles an explanation based on non-stoichiometric oxygen rich surface slabs are suggested.

References

- [1] P. Kubiak, T. Froschl, N. Husing, U. Hormann, U. Kaiser, R. Schiller, C. K. Weiss, K. Landfester, M. Wohlfahrt-Mehrens, *Small (Weinheim an der Bergstrasse, Germany)* **2011**, 7, 1690.
- [2] J.-Y. Shin, D. Samuelis, J. Maier, *Advanced Functional Materials* **2011**, 21, 3464.
- [3] J.-H. Kim, K. Zhu, J. Y. Kim, A. J. Frank, *Electrochimica Acta* **2013**, 88, 123.
- [4] L. Wang, F. Zhou, Y. S. Meng, G. Ceder, *Physical Review B* **2007**, 76, DOI 10.1103/PhysRevB.76.165435.
- [5] A. Yamada, H. Koizumi, S.-I. Nishimura, N. Sonoyama, R. Kanno, M. Yonemura, T. Nakamura, Y. Kobayashi, *Nature Materials* **2006**, 5, 357.
- [6] G. Kobayashi, S.-I. Nishimura, M.-S. Park, R. Kanno, M. Yashima, T. Ida, A. Yamada, *Advanced Functional Materials* **2009**, 19, 395.
- [7] G. Sudant, E. Baudrin, D. Larcher, J.-M. Tarascon, *Journal of Materials Chemistry* **2005**, 15, 1263.
- [8] M. Wagemaker, W. J. H. Borghols, F. M. Mulder, *Journal of the American Chemical Society* **2007**, 129, 4323.
- [9] W. J. H. Borghols, D. L. u tzenkirchen-Hecht, U. Haake, E. R. H. van Eck, F. M. Mulder, M. Wagemaker, *Physical chemistry chemical physics : PCCP* **2009**, 11, 5742.
- [10] S. Ganapathy, M. Wagemaker, *ACS NANO* **2012**, 6, 8702.
- [11] M. Wagemaker, F. M. Mulder, *Accounts of chemical research* **2013**, 46, 1206.
- [12] J. Maier, *Angewandte Chemie-International Edition* **2013**, 52, 4998.
- [13] A. Van der Ven, M. Wagemaker, *Electrochemistry Communications* **2009**, 11, 881.
- [14] C. H. Sun, X. H. Yang, J. S. Chen, Z. Li, X. W. Lou, C. Li, S. C. Smith, G. Q. M. Lu, H. G. Yang, *Chemical communications (Cambridge, England)* **2010**, 46, 6129.
- [15] M. Lazzeri, A. Vittadini, A. Selloni, *Physical Review B* **2001**, 63, 155409.
- [16] L. Kavan, M. Grätzel, S. E. Gilbert, C. Klemen, H. J. Scheel, *J. AM. Chem. Soc.* **1997**, 118, 6716.
- [17] P. W. Tasker, *Journal of Physics C: Solid State Physics* **1979**, 12, 4977.
- [18] A. A. Belak, Y. Wang, A. Van der Ven, *Chemistry of Materials* **2012**, 24, 2894.
- [19] B. J. Morgan, G. W. Watson, *The Journal of Physical Chemistry Letters* **2011**, 2, 1657.
- [20] B. J. Morgan, G. W. Watson, *Physical Review B* **2010**, 82, 144119.

- [21] M. K. Aydinol, A. F. Kohan, G. Ceder, K. Cho, *Physical Review B* **1997**, 56, 1354.
- [22] H. G. Yang, C. H. Sun, S. Z. Qiao, J. Zou, G. Liu, S. C. Smith, H. M. Cheng, G. Q. Lu, *Nature* **2008**, 453, 638.

Part II

Sodium ion insertion in sodium titanate and

TiO₂ anatase

Chapter 5

$\text{Na}_{2+x}\text{Ti}_6\text{O}_{13}$ as potential negative electrode material for Na-ion batteries

Based on paper

" $\text{Na}_{2+x}\text{Ti}_6\text{O}_{13}$ as Potential Negative Electrode Material for Na-ion Batteries", K. Shen and M. Wagemaker; Inorganic Chemistry, 2014, 53(16), 8250-8256

Abstract

Na-ion batteries provide one of the most promising alternatives for Li-ion batteries due to the high abundance and low cost of Na. The strongly electro positive character of Na enables almost comparable cell potentials. Here we show that by lowering the cut-off voltage from 0.3 V to 0 V vs Na/Na⁺ the capacity of the $\text{Na}_2\text{Ti}_6\text{O}_{13}$ negative electrode material can be enhanced from 49.5 mAh/g ($\text{Na}_{2+x}\text{Ti}_6\text{O}_{13}$) to a promising 196 mAh/g ($\text{Na}_{2+4}\text{Ti}_6\text{O}_{13}$) for at least 10 cycles, after which it gradually reduces. To understand the structural changes in-situ X-ray diffraction is performed and compared with Density Functional Theory calculations. A consistent picture of the evolution in lattice parameters and Na-ion positions is presented. The results show that Na-ion intercalation in the $\text{Na}_{2+x}\text{Ti}_6\text{O}_{13}$ host structure is limited to $\text{Na}_{2+2}\text{Ti}_6\text{O}_{13}$ and proceeds through a solid solution reaction. Only small changes in lattice parameters promote that the insertion reaction is highly reversible. Further increasing the Na composition below 0.3 V

appears to lead to loss in crystallinity, which in combination with Solid Electrolyte Interface formation is suggested to be the origin of the gradually reducing reversible capacity.

Keywords: Na-ion batteries, Na-intercalation, $\text{Na}_2\text{Ti}_6\text{O}_{12}$, solid solution

5.1 Introduction

The demand for renewable energy resources has initiated the search for high performance and cost effective battery systems. Li-ion batteries have the highest energy densities making them in particular suitable for mobile devices. However, considering applications where energy density is less important, for instance in static storage devices, the high cost of lithium ion batteries is an important concern. This has resulted in a growing interest in other battery systems such as Na-ion batteries. The Na-ion battery is one of the most promising alternatives due to its high abundance, low cost, and high cell potential. In the past decades, research on Na-ion batteries has been initiated in parallel with Li-ion battery research,¹⁻⁶ however the success of the later has largely diverted attention away from Na-ion batteries. Renewed interest in Na-ion batteries is motivated by the virtually unlimited Na resources and low costs.^{7,8} In general, the operating voltage of Na-ion batteries is about 0.4 V lower compared to Li-ions batteries, resulting in a somewhat lower but still large energy and power density.⁹ Compared with Li-ions (0.76 Å), the larger ionic radius of Na-ions (1.02 Å) often leads to larger structural distortions and barriers for diffusion in host structures.⁹ This is most likely the reason why only a few insertion electrode materials are reported displaying reversible Na-ion uptake, negative electrode materials being in particular scarce. Sodium metal as a negative electrode introduces complications such as dendrite formation, low melting point and interface aging.⁸ Graphite and hard carbons, extensively investigated as a negative electrode, have much lower specific capacities and result in larger capacity fading compared to application in Li-ion

batteries.¹⁰⁻¹² In addition, the capacitive storage of Na-ions at the graphite surface has the disadvantage of a linear drop in the battery voltage lowering the energy density.¹³ Due to the competition between inversion and conversion reactions only the 3d metal (Ti,V) oxides appear promising for low voltage Na-ion insertion.¹⁴ Na_xVO₂ was found to react reversibly around 1.5V.^{15,16} At the same potential, amorphous TiO₂ nanotubes and nanocrystalline TiO₂ anatase demonstrated a specific capacity of ~150mAh/g.¹⁷⁻²⁰ A reversible storage capacity of 200 mAh/g was achieved in Na₂Ti₃O₇ applying a cutoff voltage 0 V vs Na/Na⁺.²¹ Recently, Rudola et al. explored Na-ion storage in the structurally similar Na₂Ti₆O₁₃ compound, demonstrating a reversibly uptake of 1 Na-ion per formula unit (49.5 mAh/g) by a solid solution mechanism at an average potential of 0.8 V when Na₂Ti₆O₁₃ vs Na/Na⁺ is cycled between 2.5 V and 0.5 V.²²

Motivated by the higher storage capacities of the similar Na₂Ti₃O₇ material, the present study explores Na-ion storage in Na₂Ti₆O₁₃ at low voltages. In-situ and ex-situ X-ray diffraction in combination with Density Functional Theory (DFT) calculations reveal the intercalation mechanism, giving a consistent picture of the structural changes and electrochemical performance of this promising Na-ion negative electrode.

5.2 Preparation and Methods

Materials synthesis

Na₂Ti₆O₁₃ was prepared by ball milling Na₂CO₃ (Aldrich) and TiO₂ anatase (Aldrich) in a mass ratio 0.22:1 in a silicon carbide crucible applying a 250 rpm rate for 120 minutes. Subsequently, this precursor mixture was heated at 800 °C in open air for 12 hours, applying a heating and cooling ramp rate of 5 °C /min. X-ray diffraction analysis confirmed the crystalline Na₂Ti₆O₁₃ phase indexed with the monoclinic C2/m space group and a crystallite size of approximately 80

nm. Additionally a small amount of approximately 5%, of unreacted TiO_2 anatase and trace amounts (less than 1%) of $\text{Na}_2\text{Ti}_3\text{O}_7$ and Na_2CO_3 were identified, the latter explaining the presence of unreacted TiO_2 .

Electrode preparation

For the electrochemical tests and ex-situ X-ray diffraction measurements electrodes were prepared by mixing the active $\text{Na}_2\text{Ti}_6\text{O}_{13}$ material with the Polyvinylidene fluoride (PVDF) binder (Aldrich) and carbon black (ENSAQO) in the weight ratio 8:1:1 using N-Methyl-2-pyrrolidone (NMP) (Aldrich) as solvent. The well-mixed slurry was coated on carbon coated aluminum foil by doctor blading followed by 100 °C overnight drying .

For the in-situ X-ray diffraction measurements self-supporting electrode films were prepared. PVDF (0.42g) and DBP (Di Butyl Phthalate) (0.34g) were dissolved in acetone. The active material $\text{Na}_2\text{Ti}_6\text{O}_{13}$ (0.7g) and conductive additive carbon black (ENSAQO)(0.28g) were well mixed and added in the PVDF and DBP solution. The slurry was casted on glass by doctor blading. After drying the electrode film was washed with diethyl ether in order to dissolve DBP. Finally the coatings were dried at 100 °C overnight.

Electrochemistry

Electrochemical tests were carried out in Swagelok type electrochemical cells. The $\text{Na}_2\text{Ti}_6\text{O}_{13}$ electrodes were (dis)charged versus Sodium metal with 1M NaClO_4 in propylene carbonate serving as electrolyte and a cotton micro fiber separator (Whatman). The cells were assembled in a glove box under Argon atmosphere ($\text{O}_2 < 0.1$ ppm and $\text{H}_2\text{O} < 0.1$ ppm). The (dis)charge cycling tests were performed at C/10 rate (4 mA/g) at room temperature with a MACCOR S4000 cycler.

X-ray diffraction

In-situ and ex-situ X-ray diffraction was performed using a Panalytical X'pert Pro X-ray diffractometer employing Cu-K α radiation in the range 10-130 degree and 10-100 degree respectively. For the ex-situ X-ray diffraction characterization, the Na₂Ti₆O₁₃ vs Na/Na⁺ cell was discharged to 0V and the positive electrode was removed from the cell and assembled in a Kapton covered airtight X-ray diffraction sample holder. All these operations were performed in a glove box under Argon atmosphere (O₂ < 0.1 ppm and H₂O < 0.1 ppm).

In-situ X-ray diffraction was performed in a home designed airtight electrochemical cell with a Beryllium window acting as current collector largely transparent for X-rays. The airtight electrochemical cell was assembled in a glove box under Argon atmosphere (O₂ < 0.1 ppm and H₂O < 0.1 ppm) with sodium metal as negative electrode, cotton micro fiber as separator (Whatman) and 1M NaClO₄ in propylene carbonate serving as electrolyte. A thin aluminum foil (2 μ m) was used to restrict X-ray absorption losses and to separate the Na₂Ti₆O₁₃ electrode from the Beryllium foil window to avoid potential corrosion of the Beryllium. In-situ XRD data was restricted to a cutoff voltage of 0.3 V because cycling to ~0V in the in-situ cell leads, even of the presence of the 2mm Al foil, to corrosion of the Be and potential leaking of the cell. For this reason ex-situ XRD experiments were performed below 0.3 V. Compared to conventional electrodes, this special in-situ configuration leads to no significant changes in the voltage and capacity at the low currents applied, indicating the diffraction data collected from this in-situ cells represents the electrochemistry of the conventional electrodes. For in-situ measurement diffraction patterns were collected during the galvanostatic (dis)charge using a MACCOR S4000 cycler. For the C/10 (dis)charge rate a collection time of 1 hour was used to obtain reasonable time resolution following the structural evolution at C/10 rate in combination with patterns having enough statistics to be refined. The consequence is that each pattern

represents an average of the structural evolution during 1 hour. The X-ray diffraction patterns were refined using the Rietveld refinement method as implemented in GSAS.²³

DFT calculations

The $\text{Na}_{2+x}\text{Ti}_6\text{O}_{13}$ structures were geometrically optimized by applying the gradient-corrected exchange correlation functional (GGA) to density functional theory calculations as implemented in the plane wave code VASP²⁴⁻²⁶. Spin-polarization was not considered. All structures were fully relaxed to the ground state. A cut-off energy of 400 eV and appropriate k -point grid was chosen to ensure that total energies converged within 10^{-4} eV per formula unit. DFT Molecular dynamics simulations were performed on $\text{Na}_{2+4}\text{Ti}_6\text{O}_{13}$ unit cell for 3 ps with time step of 2 fs at two temperatures (300 K and 400 K).

5.3 Result and discussion

5.3.1 Electrochemistry

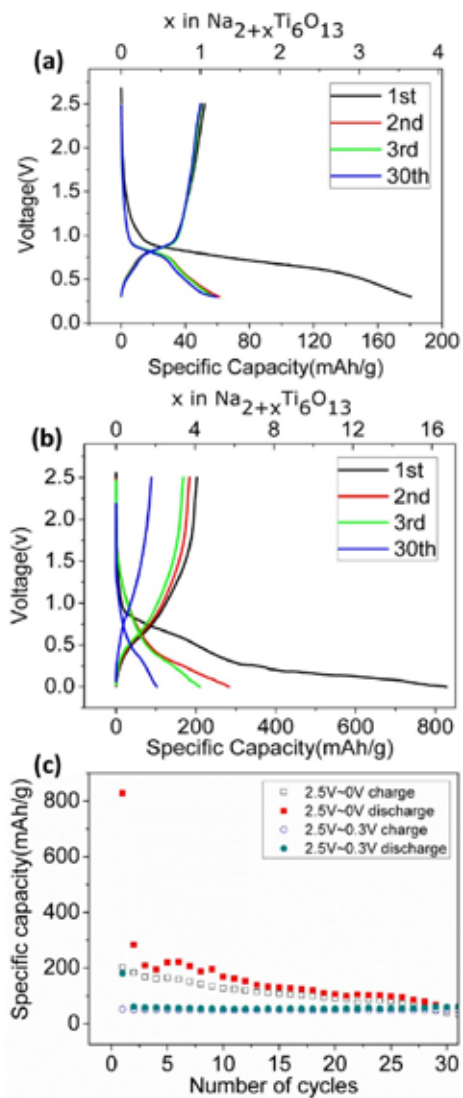


Figure 5.1. Electrochemical characterization of $\text{Na}_2\text{Ti}_6\text{O}_{13}$ vs Na/Na^+ . (a) First three cycles and the 30th cycle of the Galvanostatic (dis)charging of $\text{Na}_2\text{Ti}_6\text{O}_{13}$ at C/10 rate (0.005 A/g) down to 0.3V vs

Na/Na⁺. (b) First three cycles and the 30th cycle of the Galvanostatic (dis)charging of Na₂Ti₆O₁₃ at C/10 rate (0.005 A/g) down to 0.0 V vs Na/Na⁺. (c) Specific capacity as a function of the number of cycles at C/10 rate.

Figure 5.1a and b illustrate the impact of the cutoff voltage on the voltage-capacity profile of Na₂Ti₆O₁₃ versus sodium metal at C/10 rate (1C is defined as the current required to fully discharge/charge the Na₂Ti₆O₁₃ electrode in 1 hour assuming the maximum composition is Na₃Ti₆O₁₃). Upon reducing the cutoff voltage from 0.3 V to 0 V three distinct changes are observed: (i) When a cutoff voltage of 0.3 V is applied a reversible voltage plateau-like feature appears around 0.8 V. This is replaced by a more gradual voltage decrease when the cut-off voltage is set to 0 V. (ii) Both the first discharge capacity and the initial reversible capacity at a cutoff voltage of 0 V are four times larger compared to that at 0.3 V cutoff voltage. To rule out the contribution of carbon black and PVDF additive to the capacity, blank cells containing only carbon black and PVDF were prepared. Comparison with the Galvanostatic tests of the blank cells demonstrates that for the first discharge, carbon and PVDF contribute in total 75% to the capacity for both cut-off voltages, which is mainly irreversible as it contributes less than 10% to the reversible capacity for the subsequent cycles. Besides, the effect of the small residual TiO₂ anatase on the capacity is also evaluated by the electrochemistry test (see appendix). Therefore, based on the electrochemical measurements, we conclude that Galvanostatic cycling between 2.5 V and 0.3 V leads to the reversible intercalation of one additional sodium ion in the structure (Na₃Ti₆O₁₃), while Galvanostatic cycling between 2.5 V and 0 V leads to the reversible reaction of four additional sodium ions in the structure (Na₆Ti₆O₁₃). (iii) Figure 5.1c shows that cycling between 2.5 V and 0.3 V leads to excellent capacity retention after 30 cycles amounting to more than 95% of the initial charge capacity (disregarding the first cycle). By lowering the cutoff voltage to 0 V the capacity is larger but the reversible capacity retention

drops to approximately 75% over 30 cycles. To reveal the origin of the larger capacity and poor capacity retention when the material is cycled down to 0 V cutoff voltage, in-situ, ex-situ diffraction and DFT calculations were performed.

5.3.2 X-ray diffraction

In-situ X-ray diffraction measurements have been performed to investigate the structural changes of the $\text{Na}_2\text{Ti}_6\text{O}_{13}$ electrode material upon cycling between 2.5 and 0.3 V. In addition ex-situ XRD patterns were collected at 2.5 V, 0.3 V and 0 V to reveal the structural changes in the low potential region (0 V cutoff). Excellent reversibility of the structural changes above 0.3 V is confirmed by the reversible evolution of the Bragg peaks recorded during the charge, shown in Figure 5.2. The irreversible capacity observed during the in-situ diffraction measurement in Figure 5.2 is due to the first cycle irreversible capacity loss of the carbon and PVDF present in the electrodes discussed above.

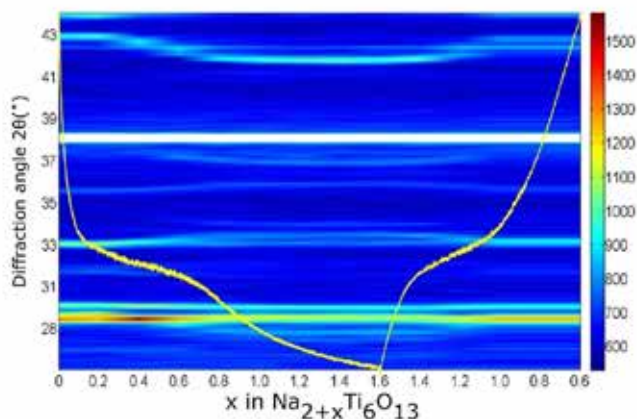


Figure 5.2. The evolution of in-situ X-ray diffraction patterns as a function of Na composition.

The yellow line represents the voltage profile down to 0.3 V, as function of intercalated Na

composition. The sodium composition x in $\text{Na}_{2+x}\text{Ti}_6\text{O}_{13}$ is estimated by the capacity measured by the galvanostatic electrochemistry.

X-ray diffraction of the prepared $\text{Na}_2\text{Ti}_6\text{O}_{13}$ material confirms the monoclinic C2/m space group having a 3-D tunnel structure in which the initially present Na-ions reside, as shown in Figure 5.3. The lattice parameters of the structure are $a=15.10\text{\AA}$, $b=3.75\text{\AA}$, $c=9.16\text{\AA}$ and $\beta=99.15^\circ$ consistent with previous studies²⁷⁻²⁹. In-situ X-ray diffraction patterns collected at various sodium compositions between $x=0$ and $x=1$ in $\text{Na}_{2+x}\text{Ti}_6\text{O}_{13}$ are shown in Figure 5.4a. The continuous shift of the original $\text{Na}_2\text{Ti}_6\text{O}_{13}$ $\{60-1\}$ and $\{40-4\}$ reflections indicate a gradual change in lattice parameters, which is consistent with the structural study on sodium intercalation into $\text{Na}_2\text{Ti}_6\text{O}_{13}$.²² The $\{020\}$ reflection splits into two reflections indexed as $\{020\}$ and $\{80-1\}$ where the $\{020\}$ reflection intensity weakens. The same phenomenon is observed for the $\{402\}$ reflection at lower angle. Remaining in the same space group this is the consequence of the significant increase of the c lattice parameter and β .

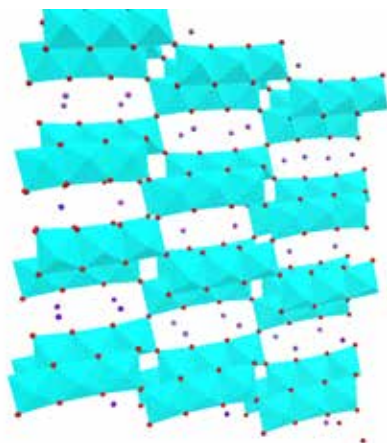


Figure 5.3. The monoclinic crystal structure of $\text{Na}_2\text{Ti}_6\text{O}_{13}$ displaying the tunnels in which the Na-ions reside. Purple spheres represent sodium ions, red spheres represent oxygen, and cyan polyhedrons represent the Ti-O octahedra.

Electrochemical discharging from 0.3 V to 0 V indicates that three additional sodium ions may be intercalated per unit formula reaching the $\text{Na}_6\text{Ti}_6\text{O}_{13}$ composition. Comparing the ex-situ XRD results at 0.3 V and 0 V reveals that the main Bragg reflections {310}, {402}, {60-1}, {40-4} of $\text{Na}_2\text{Ti}_6\text{O}_{13}$ continue shifting (see Figure 5.4b) demonstrating that also in the low potential region (0.3 V~0 V) a solid solution reaction leads to gradual unit cell expansion. Even at 0 V the structure can still be indexed with the same monoclinic space group as the pristine $\text{Na}_2\text{Ti}_6\text{O}_{13}$ phase. In addition, it is observed that the reflections decrease in intensity and increase in width. This may indicate that the crystallinity and/or crystallite size of $\text{Na}_2\text{Ti}_6\text{O}_{13}$ reduces significantly upon Na-ion addition below 0.3 V.

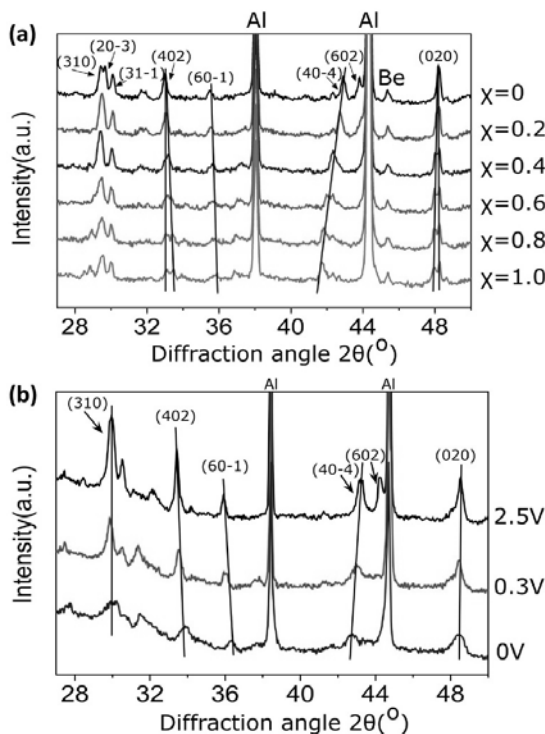


Figure 5.4. (a) Evolution of in-situ X-ray diffraction patterns of the $\text{Na}_{2+x}\text{Ti}_6\text{O}_{13}$ (x indicating the additional Na composition) electrode during the second discharge between 2.5V and 0.3V. (b) Ex-

situ X-ray diffraction patterns at 2.5 V, 0.3 V and 0 V for the $\text{Na}_{2+x}\text{Ti}_6\text{O}_{13}$ cycling between 2.5 V and 0 V.

5.3.3 DFT

X-ray diffraction reveals a solid solution reaction, however, not the Na-ion positions and occupancy in the $\text{Na}_{2+x}\text{Ti}_6\text{O}_{13}$ structure. Density Functional Theory calculations were used to predict the structure and average voltage of reduced phases at various compositions.

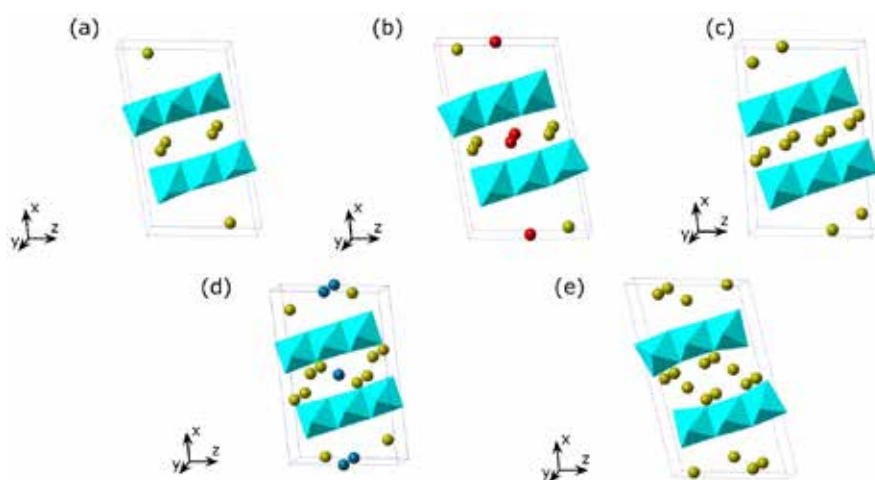


Figure 5.5. The DFT predicted monoclinic crystal structures of $\text{Na}_{2+x}\text{Ti}_6\text{O}_{13}$. (a) $\text{Na}_2\text{Ti}_6\text{O}_{13}$, (b) $\text{Na}_{2+1}\text{Ti}_6\text{O}_{13}$, (c) $\text{Na}_{2+2}\text{Ti}_6\text{O}_{13}$, (d) $\text{Na}_{2+3}\text{Ti}_6\text{O}_{13}$, (e) $\text{Na}_{2+4}\text{Ti}_6\text{O}_{13}$. Yellow spheres represent sodium ions 4i sites, red spheres represent sodium 2d sites, dark blue spheres represent sodium 2c sites and cyan polyhedrons represent the Ti-O octahedra.

By evaluating the ground state energy of all possible sodium configurations in the $\text{Na}_{2+x}\text{Ti}_6\text{O}_{13}$ unit cell at every composition ($x=0,1,2,3$ and 4), insight can be gained in the structural

evolution. Potential Na-ion sites were identified using DFT molecular dynamics simulations and Fourier density difference maps from the diffraction. Using DFT all potential positions were relaxed to the ground state and subsequently the total energies were calculated. The configuration with the lowest energy at each concentration is expected to occur upon actual Na intercalation, thereby only considering the configurational degree of freedom associated with Na-vacancy configurations in a single unit cell and neglecting the entropy contribution from lattice vibrations and electronic excitations. The DFT determined structures are shown in Figure 5.5, the structural details of which are listed in table S.I.1.

Compared to $\text{Na}_2\text{Ti}_6\text{O}_{13}$, the lowest energy configuration of $\text{Na}_{2+1}\text{Ti}_6\text{O}_{13}$, shown in Figure 5.5b, has in very small changes in the Ti-O structure. The inserting Na-ions are located on the 2d sites in the middle of the tunnel next to the already present Na-ions occupying the 4i sites. This position leads to a smaller nearest Na-Na distances (decreasing from 3.745 Å to 2.878 Å). This sodium insertion of the tunnels also shortens the nearest Na-O distance from 2.632 Å to 2.469 Å. Increasing the composition from $\text{Na}_{2+1}\text{Ti}_6\text{O}_{13}$ to $\text{Na}_{2+2}\text{Ti}_6\text{O}_{13}$ is realized by migration of the Na-ions from the 2d sites to adjacent 4i sites in the same plane as the already occupied 4i positions, further decreasing the nearest Na-Na distance to 2.482 Å and nearest Na-O distances to 2.241 Å. Upon further sodium intercalation, exceeding $\text{Na}_{2+2}\text{Ti}_6\text{O}_{13}$, the original intercalated sodium ions migrate from close to the center of the tunnels towards the edge of the Ti-O tunnel, forming half “Na-O octahedral” units, and the new Na-ions insert into 2c sites located in the center of the tunnel as shown in Figure 5.5d and 5.5e. The nearest Na-O distance continuously decreases as the Na composition increases, from 2.149 Å to 2.130 Å and as a consequence, the original nearest Na-Na distance is increased 2.607 Å in $\text{Na}_{2+3}\text{Ti}_6\text{O}_{13}$ to 2.649 Å in $\text{Na}_{2+4}\text{Ti}_6\text{O}_{13}$ indicating that the Na-Na distance is becoming too small leading to increasing repulsive Coulomb forces. The evolution of the lattice parameters suggests a variation of the shape of the 3D Ti-O tunnel upon Na insertion, resulting from the competition between the

attractive Coulomb force (between the Na-ions and oxygen forming the tunnels) and the repulsive Coulomb force (between the inserted Na-ions).

A Bond Valence Sum (BVS) analysis³⁰ was performed to evaluate the structural stability of the predicted Na inserted structures. The BVS value is estimated by $V = \sum v_i$ and the individual bond valences v_i are calculated from the observed bond lengths R_i by $v_i = \exp(\frac{R_0 - R_i}{b})$ where $R_0=1.803$ and $b=0.37$ was used for the Na-O bond³⁰, the results of which are added to Table S.I.1. If the BVS value of the insertion site is significantly larger than the formal valence of the Na-ion this indicates that the Na-ion is too large to fit the interstitial site. Only one Na-ion, 2c site in $\text{Na}_{2+3}\text{Ti}_6\text{O}_{13}$, results in a significantly larger BVS value (+1.5169) compared to the formal valence (+1) of the Na-ion. R_0 and b are empirically determined constants, depending on the local coordination shell, especially for mobile ions in alkali chalcogenides³¹. Considering this, the BVS value possibly reduces to +1.1668 using a modified R_0 and b ³¹. We therefore conclude that all Na-ions in the DFT modeled structures are potentially chemically stable.

For comparison with the experimental electrochemical results, the intercalation voltages at different Na compositions are estimated based on the ground state energy of the most stable configurations according to:

$$V(x) = -\frac{E_{\text{Na}_{2+3}\text{Ti}_6\text{O}_{13}} - E_{\text{Na}_2\text{Ti}_6\text{O}_{13}} - x \cdot E_{\text{Na}}}{x \cdot e} \quad \text{Equation. 5.1}$$

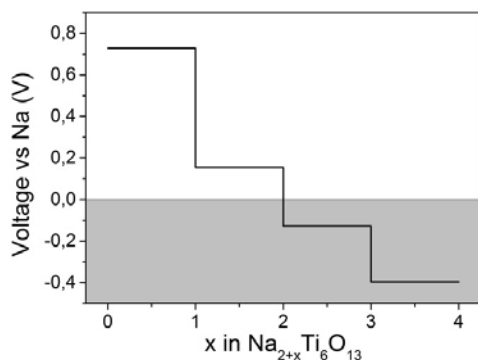


Figure 5.6. Calculated insertion voltage profile based on the DFT ground state energies as function of the sodium composition.

The calculated average voltages in Figure 5.6 show that, as expected, increasing the Na compositions lowers the voltage (in this case referenced to Na-metal Na/Na^+) which is correlated to the evolution of the Na-O distance. The calculated average intercalation voltage of 0.728 V between $x=0$ and $x=1$ in $\text{Na}_{2+x}\text{Ti}_6\text{O}_{13}$ is in good agreement with the experimentally observed reversible voltage of approximately 0.8 V for these compositions, see Figure 5.1a. The underestimation of the potential by GGA is typical for transition metal oxides and the result of the self-interaction in the d-orbitals³². The predicted average voltage between the $x=1$ and $x=2$ compositions is approximately 0.15 V indicating that these compositions are not formed above 0.3 V, consistent with the observations in Figure 5.1a. The DFT results in Figure 5.6 predict that the maximum composition that can be achieved at 0 V vs Na/Na^+ is $\text{Na}_{2+2}\text{Ti}_6\text{O}_{13}$. Increasing the composition from $x=3$ to 4 results in negative voltages implying that these compositions will not be formed in practice and that $\text{Na}_{2+2}\text{Ti}_6\text{O}_{13}$ is the upper limit for sodium insertion in bulk $\text{Na}_{2+x}\text{Ti}_6\text{O}_{13}$. However, electrochemical cycling down to 0 V after the first cycle, shown in Figure 5.1b, suggests a reversible composition up to $x=4$ (~200 mAh/g), albeit degrading over several cycles, see Figure 5.1c. This capacity is not due to carbon and PVDF because this does contribute significantly to the total capacity after the first cycle (see Figure S.I.1). The $x=4$ composition is in contradiction with the DFT calculations that predict the maximum

composition (leading to positive voltages vs Na/Na⁺) of x=2. Apparently, at these low voltages a different storage mechanism sets in as discussed below.

5.3.4 Discussion

Using the most stable Na_{2+x}Ti₆O₁₃ configuration from DFT as input for the Rietveld refinement of the XRD pattern results in a good fit, shown in Figure 5.7, implying minimal changes in the atomic positions and lattice parameters indicating that DFT predicts the structure accurately. The unit cell dimensions of Na_{2+x}Ti₆O₁₃ determined from the Rietveld refinement are shown in Table 5.1 and the atomic positions are given in table S.I.1. The small volume expansion (1%) between the original Na₂Ti₆O₁₃ and the Na_{2+x}Ti₆O₁₃ compositions suggests that mechanical failure of the material will not play a significant role, which is consistent with the excellent cycling stability observed above 0.3 V in Figure 5.1.

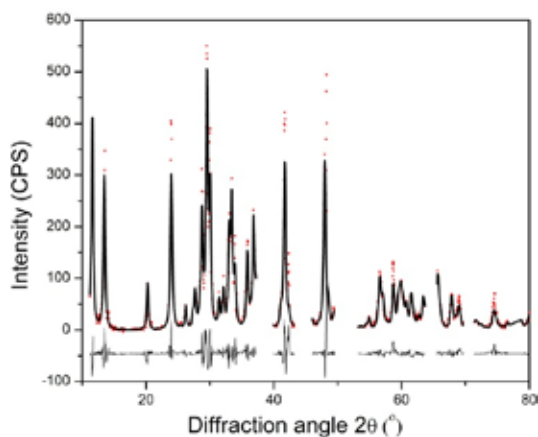


Figure 5.7. Rietveld refinement of the in-situ X-ray diffraction pattern of Na_{2+x}Ti₆O₁₃ after the second discharge. Red symbols represent the experimental data, the solid line represents the Rietveld refinement, and at the bottom the difference between observed and calculated intensities is shown. The refined parameters include lattice parameters, atomic positions, a broadening

parameter and the temperature factor. The peaks from aluminium and beryllium have been excluded. The average agreement index parameters are $R_p=4.1\%$ and $R_{wp}=5.5\%$.

Due to the severe broadening of the diffraction reflections in the low potential region, it is difficult to obtain a satisfying fit of the XRD patterns below 0.3 V. Nevertheless, the lattice parameters can be accurately determined by the positions of diffraction peaks. The results indicate that the unit cell expansion continues in the low potential region between 0.3 V to 0 V (see Table 5.1). Assuming Vegard's law, the intercalated sodium composition is calculated for the material cycled to 0 V. The resulting sodium composition at 0 V is $\text{Na}_{2+2.11}\text{Ti}_6\text{O}_{13}$ consistent with the upper limit determined by DFT ($\text{Na}_{2+x}\text{Ti}_6\text{O}_{13}$). The comparison between the observed XRD pattern at 0V and the simulated diffraction patterns using the DFT structures at $x=2,3,4$ in $\text{Na}_{2+x}\text{Ti}_6\text{O}_{13}$, presented in Figure S.I.2, indicates best agreement with the $x=2$ DFT predicted structure. This is consistent with the bulk composition $x=2.11$ derived from the lattice parameters using Vegard's law, indicating that at 0 V vs Na/Na^+ the bulk composition is close to $x=2$.

Table 5.1. Lattice parameters of $\text{Na}_{2+x}\text{Ti}_6\text{O}_{13}$ collected at various sodium compositions. The composition for the sample A is estimated by the capacity resulting from the electrochemistry in Figure 5.1, and the composition of sample B is estimated assuming Vegard's law between $x=0$ and $x=1$.

	a	b	c	β	Cell volume	x in $\text{Na}_{2+x}\text{Ti}_6\text{O}_{13}$
Original	15.11	3.746	9.175	99.037	512.74	0
Sample A at $x=1$	14.88	3.757	9.415	100.587	517.35	1
Sample B at 0V	15.00	3.778	9.364	100.056	522.51	2.11

Comparing the $\text{Na}_{2+1}\text{Ti}_6\text{O}_{13}$ and $\text{Na}_{2+2}\text{Ti}_6\text{O}_{13}$ structures in Figure 5.5b and 5.5c Na addition leads to migration of the 2d site towards the adjacent 4i site resulting in minor lattice changes (0.98 %), also in good agreement with the XRD results in Table 5.1 (0.99 %).

Upon further sodium insertion (exceeding $\text{Na}_{2+2}\text{Ti}_6\text{O}_{13}$) the BVS value (see table S.1 in appendix) increases significantly from $\text{Na}_{2+2}\text{Ti}_6\text{O}_{13}$ to $\text{Na}_{2+3}\text{Ti}_6\text{O}_{13}$ implying a lack of space in the 3D tunnel structure for the inserted Na-ions making these structures unlikely to form in reality, consistent with DFT that predicts a negative voltage vs Na/Na^+ . When the cell is charged to ~0 V, the diffraction peaks irreversibly decrease in intensity and increase in width. This may be a sign of effective loss in particle size and/or crystallinity, potentially responsible for the poor reversibility at low voltages. This may indicate that part of the total capacity at 0 V is due to a reaction of Na at the surface of $\text{Na}_2\text{Ti}_6\text{O}_{13}$. For instance higher Na insertion compositions at the surface may lead to strain or structural disorder, factors that both lead to diffraction line broadening. In addition, the poor reversibility could be the result of side reactions. Several comprehensive studies on structural evolution and electrochemical behavior of Na-inserted hard carbon cycled to 0 V demonstrate the formation of the solid electrode/electrolyte interface (SEI) on the surface of the electrode^{13,33}. The continuous growing SEI on the surface of hard carbon, caused by the continuous decomposition of the NaClO_4 -PC electrolyte upon cycling, is suggested to be the main reason of the capacity fading in carbonaceous materials with NaClO_4 -PC after 30 cycles³⁴. Although the study of SEI formed on transition metal oxides materials is absent up to date, we anticipate that electrolyte reduction and decomposition may also take place at the $\text{Na}_2\text{Ti}_6\text{O}_{13}$ surface. Further efforts should be directed towards optimizing the electrolyte as was recently achieved for Na insertion in anatase using NaPF_6 in EC:PC³⁴.

Also in the similar $\text{Na}_2\text{Ti}_3\text{O}_7$ structure reported recently²¹ two thirds of the Ti^{4+} states are converted to the Ti^{3+} states in the same voltage window (from 2.5V to 0V) resulting in a similar reversible capacity (~200mAh/g). In addition, the cycling stability of $\text{Na}_2\text{Ti}_3\text{O}_7$ is excellent

when the cut-off voltage is increased from 0.01V to 0.1V³⁵. However, as the sodium 2e sites in Na₂Ti₃O₇ have already been fully occupied in the pristine Na₂Ti₃O₇ structure, more structural rearrangements are required to accommodate additional sodium in Na₂Ti₃O₇ compared to Na₂Ti₆O₁₃. Most likely this is the reason why, upon sodium intercalation in Na₂Ti₃O₇, new reflections appear at the expense of the original main reflections, indicating a phase transition, while in Na₂Ti₆O₁₃ a solid solution mechanism is observed.

5.4 Conclusion

In conclusion, by lowering the cutoff voltage Na₂Ti₆O₁₃ to 0 V a promising reversible capacity of nearly 200 mAh/g is found accompanied with minor structural changes following a predominantly solid solution mechanism. This makes Na₂Ti₆O₁₃ a promising negative electrode material for Na-ion batteries as compared to other titanium oxide materials such as TiO₂ anatase^{19,20,22,32,36} and Na₄Ti₅O₁₂³⁷. However, the challenge is to extend the reversible capacity over more cycles which may be achieved by electrolytes resulting in a more stable SEI. DFT predicts that the voltage region around 0.8 V vs Na/Na⁺ corresponds to the intercalation of the sodium ions at the 2d sites in the tunnel and that only two sodium ions are able to intercalate in the structure of Na₂Ti₆O₁₃ above 0 V vs Na/Na⁺. Further Na addition is suggested to be react at the surface of Na₂Ti₆O₁₃ potentially responsible for the observed loss in crystallinity and/or decrease in particle size.

References

- (1) Whittingham, M. S. *Progress in Solid State Chemistry* **1978**, *12*, 44–99.
- (2) Nagelberg, A. S.; Worrell, W. L. *Journal of Solid State Chemistry* **1979**, *29*, 345–354.
- (3) Molenda, J.; Delmas, C.; Hagenmuller, P. *Solid State Ionics* **1983**, *9&10*, 431–436.
- (4) Delmas, C.; Braconnier, J.-J.; Fouassier, C.; Hagenmuller, P. *Solid State Ionics* **1981**, *3-4*, 165–169.
- (5) Tarascon, J. M.; Hull, G. W. *Solid State Ionics* **1986**, *22*, 85–96.
- (6) Abraham, K. M. *Solid State Ionics* **1982**, *7*, 199–212.
- (7) Chevrier, V. L.; Ceder, G. *Journal of the Electrochemical Society* **2011**, *158*, A1011–A1014.
- (8) Palomares, V.; Serras, P.; Villaluenga, I.; Hueso, K. B.; Carretero-González, J.; Rojo, T. *O. F. Energy & Environmental Science* **2012**, *5*, 5884–5901.
- (9) Ong, S. P.; Chevrier, V. L.; Hautier, G.; Jain, A.; Moore, C.; Kim, S.; Ma, X.; Ceder, G. *Energy & Environmental Science* **2011**, *4*, 3680–3688.
- (10) Alcántara, R.; Jiménez-Mateos, J. M.; Lavela, P.; Tirado, J. L. *Electrochemistry Communications* **2001**, *3*, 639–642.
- (11) Stevens, D. A.; Dahn, J. R. *Journal of the Electrochemical Society* **2000**, *147*, 1271–1273.
- (12) Wenzel, S.; Hara, T.; Janek, J. U. R.; Adelhelm, P. *Energy & Environmental Science* **2011**, *4*, 3342–3345.
- (13) Komaba, S.; Murata, W.; Ishikawa, T.; Yabuuchi, N.; Ozeki, T.; Nakayama, T.; Ogata, A.; Gotoh, K.; Fujiwara, K. *Advanced Functional Materials* **2011**, *21*, 3859–3867.
- (14) Cabana, J.; Monconduit, L.; Larcher, D.; Palacin, M. R. *Advanced Materials* **2010**, *22*, E170–E192.
- (15) Didier, C.; Guignard, M.; Denage, C.; Szajwaj, O.; Ito, S.; Saadoune, I.; Darriet, J.; Delmas, C. *Electrochemical and Solid State Letters* **2011**, *14*, A75–A78.
- (16) Hamani, D.; Ati, M.; Tarascon, J.-M.; Rozier, P. *Electrochemistry Communications* **2011**, *13*, 938–941.
- (17) Xiong, H.; Slater, M. D.; Balasubramanian, M.; Johnson, C. S.; Rajh, T. *The Journal of Physical Chemistry Letters* **2011**, *2*, 2560–2565.
- (18) Xu, Y.; Memarzadeh Lotfabad, E.; Wang, H.; Farbod, B.; Xu, Z.; Kohandehghan, A.; Mitlin, D. *Chemical communications (Cambridge, England)* **2013**, *49*, 8973–8975.

- (19) Wu, L.; Buchholz, D.; Bresser, D.; Gomes Chagas, L.; Passerini, S. *Journal of power sources* **2014**, *251*, 379–385.
- (20) Kim, K.-T.; Ali, G.; Chung, K. Y.; Yoon, C. S.; Yashiro, H.; Sun, Y.-K.; Lu, J.; Amine, K.; Myung, S.-T. *Nano Letters* **2014**, *14*, 416–422.
- (21) Senguttuvan, P.; Rousse, G.; Seznec, V.; Tarascon, J.-M.; Palacin, M. R. *Chem. Mater.* **2011**, *23*, 4109–4111.
- (22) Rudola, A.; Saravanan, K.; Devaraj, S.; Gong, H.; Balaya, P. *Chemical communications (Cambridge, England)* **2013**, *49*, 7451–7453.
- (23) Larson, A. C. GSAS; Los Alamos National Laboratory, 1994.
- (24) Blöchl, P. E. *Physical Review B* **1994**, *50*, 17953–17979.
- (25) Kresse, G.; Furthmüller, J. *Physical Review B* **1996**, *54*, 11169–11186.
- (26) Kresse, G.; Joubert, D. *Physical Review B* **1999**, *59*, 1758–1775.
- (27) Pérez-Flores, J. C.; García-Alvarado, F.; Hoelzel, M.; Sobrados, I.; Sanz, J.; Kuhn, A. *Dalton Transactions* **2012**, *41*, 14633–14642.
- (28) Torres-Martínez, L. M.; Juárez-Ramírez, I.; Del Ángel-Sánchez, K.; Garza-Tovar, L.; Cruz-López, A.; Del Ángel, G. *Journal of Sol-Gel Science and Technology* **2008**, *47*, 158–164.
- (29) Andersson, S.; Wadsley, A. D. *Acta Crystallographica* **1962**, *15*, 194–201.
- (30) Brown, I. D.; Altermatt, D. *Acta Crystallogr B Struct Sci* **1985**, *41*, 244–247.
- (31) Adams, S. *Acta Crystallogr B Struct Sci* **2001**, *57*, 278–287.
- (32) Zhou, F.; Cococcioni, M.; Kang, K.; Ceder, G. *Electrochemistry Communications* **2004**, *6*, 1144–1148.
- (33) Gotoh, K.; Ishikawa, T.; Shimadzu, S.; Yabuuchi, N.; Komaba, S.; Takeda, K.; Goto, A.; Deguchi, K.; Ohki, S.; Hashi, K.; Shimizu, T.; Ishida, H. *Journal of power sources* **2013**, *225*, 137–140.
- (34) Ponrouch, A.; Marchante, E.; Courty, M.; Tarascon, J.-M.; Palacin, M. R. *Energy & Environmental Science* **2012**, *5*, 8572–8583.
- (35) Rudola, A.; Saravanan, K.; Mason, C. W.; Balaya, P. *Journal of Materials Chemistry A* **2013**, *1*, 2653–2662.
- (36) Lindström, H.; Södergren, S.; Solbrand, A.; Rensmo, H.; Hjelm, J.; Hagfeldt, A.; Lindquist, S.-E. *J. Phys. Chem. B* **1997**, *101*, 7710–7716.
- (37) Woo, S. H.; Park, Y.; Choi, W. Y.; Choi, N. S.; Nam, S.; Park, B.; Lee, K. T. *Journal of the Electrochemical Society* **2012**, *159*, A2016–A2023.

Appendix

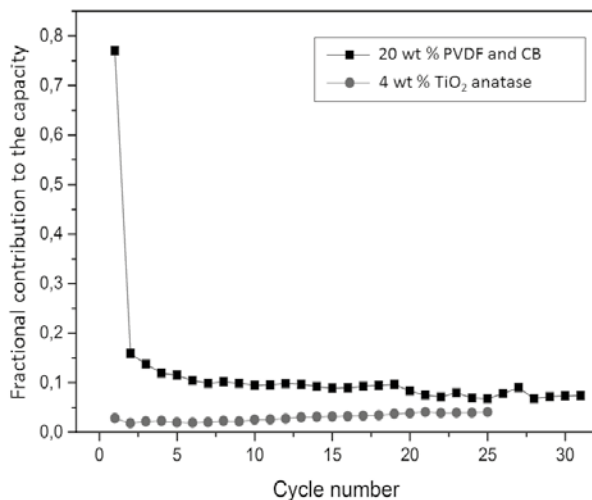


Figure S.I.1. Black symbols: Electrodes with only conductive carbon and PVDF were prepared demonstrating that the fractional contribution from carbon and PVDF to the capacity drops below 10 after a few cycles. Red points indicate the capacity contribution from the residual TiO₂ anatase upon cycling.

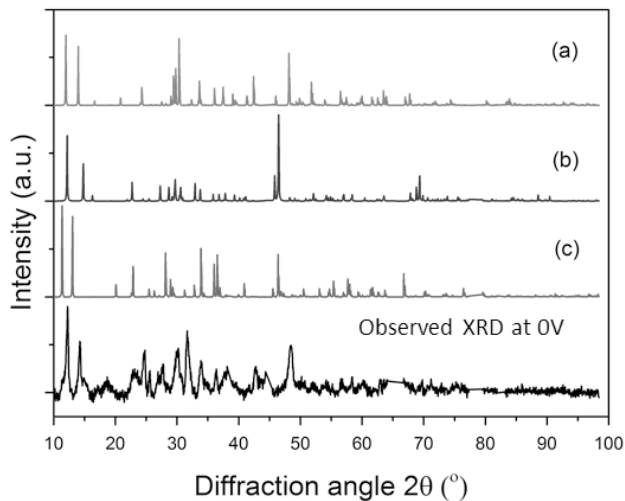


Figure S.I.2 Comparison between the observed XRD pattern at 0V (electrochemically $x=4$, structurally $x=2$ in $\text{Na}_{2+x}\text{Ti}_6\text{O}_{13}$) and the simulated patterns using the DFT determined

structures at the composition (a) $\text{Na}_{2+2}\text{Ti}_6\text{O}_{13}$, (b) $\text{Na}_{2+3}\text{Ti}_6\text{O}_{13}$ and (c) $\text{Na}_{2+4}\text{Ti}_6\text{O}_{13}$. Best agreement is between the observed XRD pattern at 0V and DFT predicted $\text{Na}_{2+3}\text{Ti}_6\text{O}_{13}$.

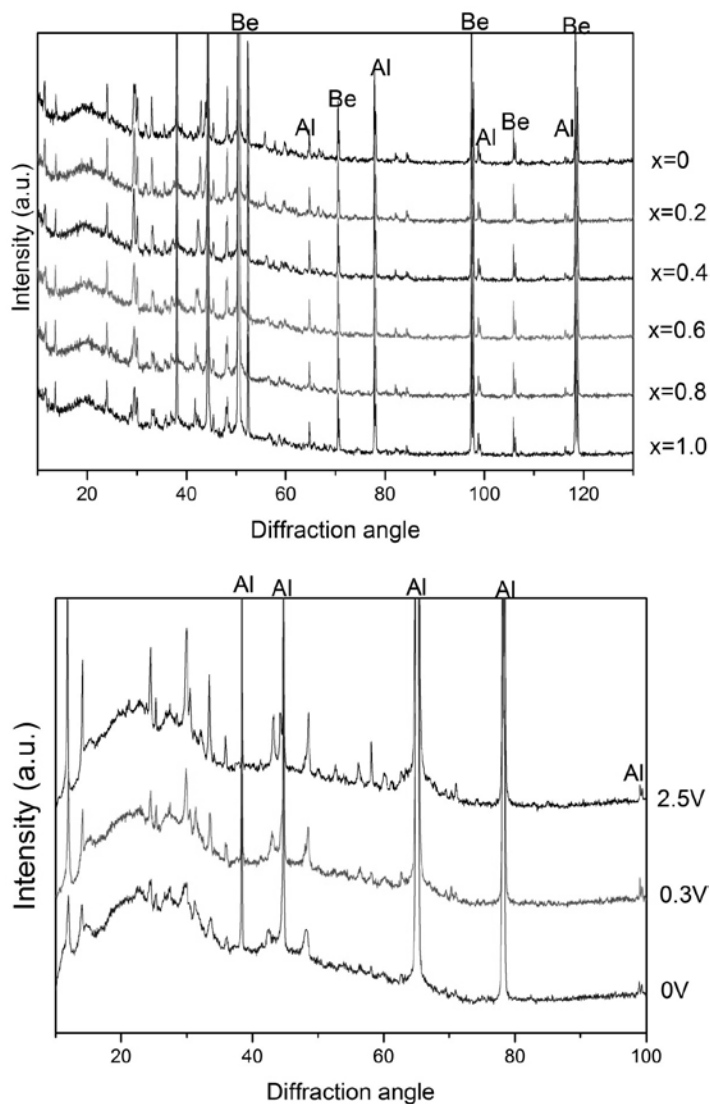


Figure S.I.3. Top: Full in-situ XRD patterns collected during charge down to 0.3 V. Bottom: Ex-situ XRD patterns at 0.3 V and 0.0 V. Al and Be indicate the reflections due to the Aluminum and Beryllium current collector respectively.

Table S.I.1. $\text{Na}_{2+1}\text{Ti}_6\text{O}_{13}$ structure data determined from Rietveld refinement of the XRD pattern. The $\text{Na}_{2+2}\text{Ti}_6\text{O}_{13}$, $\text{Na}_{2+3}\text{Ti}_6\text{O}_{13}$ and $\text{Na}_{2+4}\text{Ti}_6\text{O}_{13}$ structures are DFT predicted. The BVS values are the results from the bond valence sum calculations.

$\text{Na}_{2+1}\text{Ti}_6\text{O}_{13}$, $a=14.880077\text{\AA}$, $b=3.756987\text{\AA}$, $c=9.414455\text{\AA}$, $\beta=100.587^\circ$, space group $c12/m1$. The average agreement index parameters are $R_p=4.1\%$ and $R_{wp}=5.5\%$. The refined isotropic thermal parameter $U_{iso}=0.012$.

Atom	Wkckoff	X	Y	Z	Multiplicity	BVS	occupancy
Na	4i	0.471714	0	0.189316	4	0.4468	1
Na	2d	0.5	0	0.5	2	0.3613	1
Ti	4i	0.119377	0	0.090748	4		1
Ti	4i	0.157138	0	0.436824	4		1
Ti	4i	0.223410	0	0.759997	4		1
O	4i	0.267934	0	0.278369	4		1
O	4i	0.071513	0	0.298388	4		1
O	4i	0.316272	0	0.583704	4		1
O	4i	0.110748	0	0.63282	4		1
O	4i	0.35545	0	0.88871	4		1
O	4i	0.16508	0	0.91469	4		1
O	2a	0	0	0	2		1

$\text{Na}_{2+2}\text{Ti}_6\text{O}_{13}$ $a=14.997621\text{\AA}$, $b=3.777726\text{\AA}$, $c=9.36428\text{\AA}$, $\beta=100.0562^\circ$, space group $c12/m1$

Atom	Wyckoff	X	Y	Z	Multiplicity	BVS	Occupancy
Na	4i	0.39985	0	0.10096	4	0.4945	1
Na	4i	0.48686	0	0.35214	4	0.5470	1
Ti	4i	0.11119	0	0.13091	4		1
Ti	4i	0.17046	0	0.45888	4		1
Ti	4i	0.24572	0	0.78124	4		1
O	4i	0.24291	0	0.24899	4		1

O	4i	0.06391	o	0.33062	4	1
O	4i	0.30781	o	0.55833	4	1
O	4i	0.12736	o	0.64296	4	1
O	4i	0.3859	o	0.85395	4	1
O	4i	0.18233	o	0.9461	4	1
O	2a	o	o	o	2	1

$\text{Na}_{2+3}\text{Ti}_6\text{O}_{13}$ $a=14.588\text{\AA}$, $b=4.061\text{\AA}$, $c=9.207\text{\AA}$, $\beta=95.62^\circ$, space group $c12/m1$

Atom	Wyckoff	X	Y	Z	Multiplicity	BVS	Occupancy
Na	4i	0.37237	o	0.11524	4	1.0087	1
Na	4i	0.52434	o	0.28964	4	0.8653	1
Na	2c	0.5	0.5	0.5	2	1.5169	1
Ti	4i	0.11743	o	0.11	4		1
Ti	4i	0.18658	o	0.4433	4		1
Ti	4i	0.24563	o	0.75719	4		1
Ti	4i	0.24477	o	0.76777	4		1
O	4i	0.24666	o	0.24304	4		1
O	4i	0.07323	o	0.30852	4		1
O	4i	0.31204	o	0.56707	4		1
O	4i	0.133750	o	0.6272	4		1
O	4i	0.37361	o	0.87396	4		1
O	4i	0.18135	o	0.9348	4		1
O	2a	o	o	o	2		1

$\text{Na}_{2+4}\text{Ti}_6\text{O}_{13}$ $a=15.96\text{\AA}$, $b=4.006\text{\AA}$, $c=9.336\text{\AA}$, $\beta=104.16^\circ$, space group $c12/m1$

Atom	Wyckoff	X	Y	Z	Multiplicity	BVS	Occupancy
Na	4i	0.50979	o	0.14589	4	0.6966	1

Na	4i	0.59395	o	0.53331	4	0.7916	1
Na	4i	0.44976	0.5	0.27757	4	1.1547	1
Ti	4i	0.12978	o	0.079	4		1
Ti	4i	0.186	o	0.41638	4		1
Ti	4i	0.24395	o	0.7765	4		1
O	4i	0.24628	o	0.23852	4		1
O	4i	0.08293	o	0.27569	4		1
O	4i	0.30321	o	0.58517	4		1
O	4i	0.1446	o	0.5934	4		1
O	4i	0.36449	o	0.9199	4		1
O	4i	0.16849	o	0.90194	4		1
O	2a	o	o	o	2		1

Chapter 6

Na insertion in TiO₂ anatase, bulk versus surface storage

Abstract

The particle size dependent electrochemical Na-ion storage in TiO₂ anatase is investigated by electrochemistry and X-ray diffraction. Reducing the particle size from 130 to 40 and 7 nm results in an increase in reversible capacity leading to 170 mAh/g for 7 nm particles during the first cycles reducing thereafter. X-ray diffraction on the reduced (Na-ion inserted) electrodes after several discharge and charge cycles shows negligible changes in lattice parameters suggesting Na-ion insertion does not occur significantly. In contrast, DFT calculations predict that the maximum composition NaTiO₂ (capacity 334mAh/g) should be achieved at an average voltage of approximately 0.3 V vs Na/Na⁺. However, the high energy barrier for Na diffusion between sites (~0.84 eV) appears to prevent Na-ion insertion. This indicates that the electrochemical observed Na-ion storage is due an X-ray diffraction amorphous surface formation reaction, consistent with the higher capacities of smaller particle sizes. Therefore strategies to improve the electrochemical performance of Na storage in nano structured TiO₂ anatase should focus on the phase resulting after the surface reconstruction, and also electrolyte stability.

6.1 Introduction

Na-ion batteries provide one of the most promising alternatives for Li-ion batteries due to the high abundance and low cost of Na. The strongly electro positive character of Na enables almost comparable cell potentials. In the past decades, research on Na-ion batteries has been initiated in parallel with Li-ion battery research,¹⁻⁶ however the success of the later has largely diverted attention away from Na-ion batteries. Renewed interest in Na-ion batteries is motivated by the virtually unlimited Na resources and associated low costs.^{7,8} In general, the operating voltage of Na-ion batteries is about 0.4 V lower compared to Li-ions batteries, resulting in a somewhat lower but still large energy and power density.⁹ In addition, compared with Li-ions (0.76 Å), the larger ionic radius of Na-ions (1.02 Å) often leads to larger structural distortions and barriers for diffusion in host structures.⁹ This is most likely the reason why only a few insertion electrode materials are reported displaying reversible Na-ion uptake, negative electrode materials being in particular scarce. Sodium metal as a negative electrode introduces complications such as dendrite formation, low melting point and interface aging.⁸ Graphite and hard carbons, extensively investigated as a negative electrode, have much lower specific capacities and result in larger capacity fading compared to Li-ions.¹⁰⁻¹² In addition, the capacitive storage of Na-ions at the graphite surface has the disadvantage of a linear drop in the battery voltage lowering the energy density.¹³ Due to the competition between inversion and conversion reactions the 3d metal (Ti,V) oxides appear promising for low voltage Na-ion insertion.¹⁴ Na_xVO_2 was found to react reversibly around 1.5V.^{15,16} A reversible storage capacity of 200 mAh/g was achieved in $\text{Na}_2\text{Ti}_3\text{O}_7$ at an insertion voltage close to 0.3 V and cutoff voltage 0 V vs Na/Na^+ .¹⁷ The structurally similar $\text{Na}_2\text{Ti}_6\text{O}_{13}$ compound demonstrates a highly reversibly uptake of 1 Na ion per formula unit (49.5 mAh/g)¹⁸ which can be increased to almost 200 mAh/g by lowering to voltage towards 0 V vs Na/Na^+ albeit with a degrading capacity over ten's of cycles (see chapter 5).

Anatase TiO_2 is an extensively investigated negative electrode material for lithium ion batteries, exhibiting large reversible capacity¹⁹⁻²¹ and excellent gravimetric and volumetric storage capacities^{22,23}, with the disadvantage of having a relatively high potential versus Li/Li^+ as negative electrode. Na storage in TiO_2 anatase materials has been reported in different nanostructured morphology types, including amorphous nanotubes²⁴, nanocrystals²⁵ and carbon coated nanorods²⁶. High rate capacity (104 mAh/g at 10C rate)²⁶ and good reversibility (150mAh/g after 100 cycles)²⁶ have been obtained. These capacities are well below that obtained for lithium insertion nano-structured TiO_2 anatase¹⁹⁻²³ and unlike Li-ion storage, substantial Na-ion storage is mainly reported in nanostructured anatase TiO_2 suggesting bulk Na-ion storage is limited. An early study, combining electrochemistry and quantum chemical calculations, however, report comparable diffusion barriers for Li and Na-ions in bulk anatase.²⁷

To resolve this discrepancy and gain more insight in the possibilities to use anatase TiO_2 materials as negative electrode in Na-ion batteries we study the impact of particle size on the Na-ion insertion in TiO_2 anatase. Galvanostatic cycling tests are performed on three TiO_2 anatase particle sizes, 7, 40 and 130 nm, and ex-situ X-ray diffraction is applied on fully reduced electrodes to characterize the structure changes upon Na insertion. DFT energy and activation barrier calculation are applied to model the reduced structure and estimate the intercalation voltage and Na ion migration barriers. This combination of techniques gives insight in the role of surface versus bulk Na storage and the potential use of anatase TiO_2 as negative electrode for Na-ion batteries.

6.2 Experimental technique

Materials preparation

130 nm, and 40 nm TiO_2 particles were obtained from Aldrich. For 7 nm TiO_2 anatase particles, deionized water was added to the mixture of titanium isopropoxide and anhydrous acetone under stirring in an ice bath as reported by Borghols et al²⁸. The resulting white precipitate, amorphous TiO_2 , was filtered out and washed multiple times with anhydrous acetone before drying overnight at 50 °C. To obtain nanocrystalline anatase the amorphous TiO_2 anatase was heated to 250 °C in 10 minutes in open air and annealed for 4 hours. The material was further dried in a vacuum furnace at 80 °C for a week. The crystalline structure and particle size of the final product was confirmed using TEM (see figure 6.1) and X-ray diffraction, revealing tetragonal anatase with a crystalline size of approximately 7 nm.

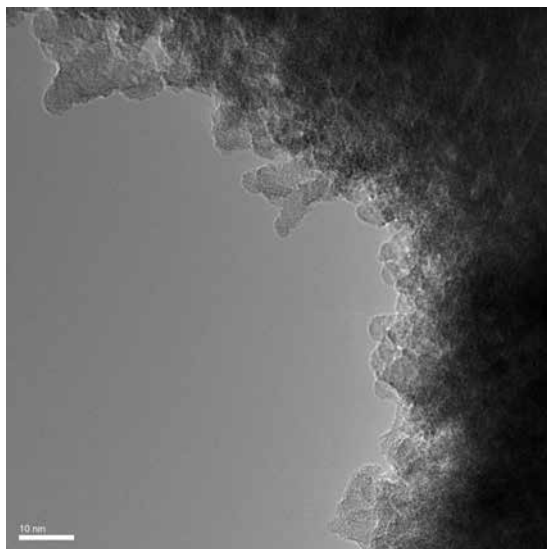


Figure 6.1 High resolution TEM micrograph of nano-crystalline TiO_2 anatase

Electrode preparation

For 130 nm and 40 nm anatase TiO_2 , the electrodes used for electrochemistry measurements and X-ray diffraction were prepared from a mixture of 80 wt% TiO_2 anatase, 10 wt% polyvinylidene fluoride binder (Aldrich) and 10 wt% carbon black (ENSAQO, Aldrich) using N-Methyl-pyrrolidone (Aldrich) as solvent. For the 7 nm particles, the weight ratio was revised to 70:20:10 respectively. The well-mixed slurries were doctor bladed on carbon coated aluminum foil and dried in a fume hood overnight and then placed in a vacuum furnace at approximately 100 °C for several days.

Electrochemical experiments

Galvanostatic charge-discharge cycling tests were performed at C/10 rate using a MACCOR S4000 cycler. Sodium metal was used as counter electrode for the anatase TiO_2 electrode. The two electrodes were separated by a porous cotton microfiber (Whatman). 1M NaClO_4 in propylene carbonate was served as electrolyte. All cells were assembled with air tight flange cells in a glove box under argon atmosphere ($\text{H}_2\text{O} < 0.1$ ppm and $\text{O}_2 < 0.1$ ppm).

X-ray diffraction

X-ray diffraction characterization was carried out using a Panalytical X'pert Pro diffractometer equipped with a Cu-K_α tube. The diffraction patterns were collected on TiO_2 electrodes that were reduced to 0 V vs Na/Na^+ and on electrodes that were oxidized after reduction to 2.8V. The electrodes were placed in Kapton airtight sample holders designed to perform XRD. All sample preparations were carried out in argon atmosphere in glove box ($\text{H}_2\text{O} < 0.1$ ppm and $\text{O}_2 < 0.1$ ppm) to prevent reactions with air and moisture.

Density Functional Theory

The Na_xTiO_2 structures were geometrically optimized to their ground state by relaxing the unit cell size, shape and the atom positions. The structural relaxation and total energy calculations were performed using the gradient-corrected exchange correlation functional to density functional theory simulations, as implemented in the VASP *ab-initio* calculations package. A cut-off energy of 400 eV and appropriate k -point grid was determined by a convergence test on the total energies, the criterium of which was set to reach energy changes less than 10^{-4} eV per formula unit. The nudged elastic band (NEB) method as implemented in the VASP code was used to estimate the activation energy barriers for Na hopping between adjacent octahedral interstitial sites. A $2 \times 2 \times 1$ supercell of pure TiO_2 anatase (doubling along both the a and the b directions) was applied for the energy barrier calculation, where first the end-states were relaxed to the ground state. All the energy barrier calculations were performed with constant unit cell dimensions and shape. The negligible changes on the NEB calculation results for a larger supercell ($2 \times 2 \times 2$) confirms that the size of the supercell ($2 \times 2 \times 1$) is sufficiently adequate to remove the Na-Na self interaction effect from the periodically repeated cells on the activation barrier.

6.3 Results and discussion

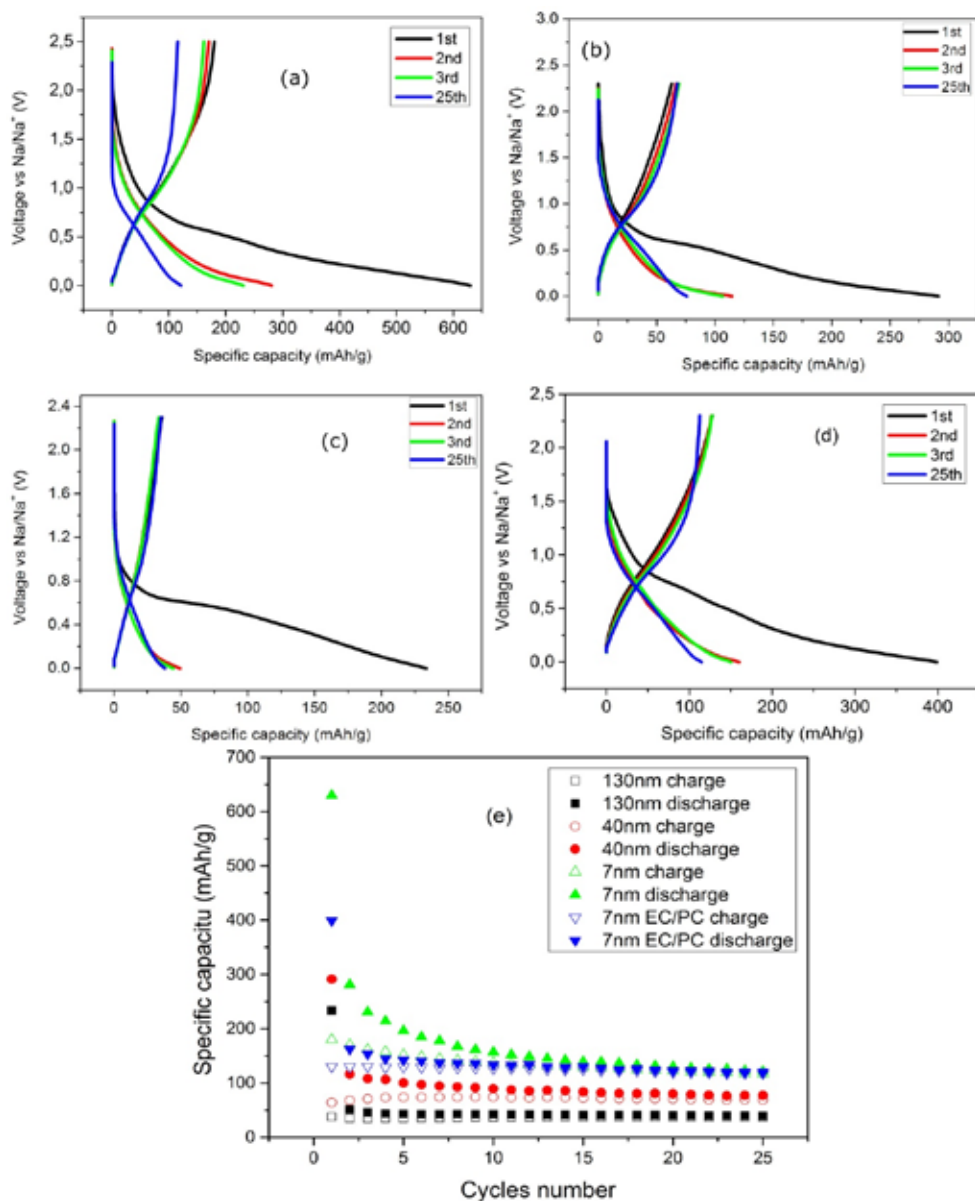


Figure 6.2 Electrochemical characterization of TiO_2 anatase vs Na/Na^+ . First three cycles and the 25th cycle of the Galvanostatic (dis)charging at $C/10$ rate (0.005 A/g) for TiO_2 electrodes with (a) 7 nm, (b) 40 nm, (c) 130 nm particles (d) 7 nm particles with EC/PC electrolyte. (e) Specific

(dis)charge capacity as a function of the number of cycles at C/10 rate for the different particle sizes.

Figure 6.2a-c show the voltage-capacity profiles collected for different particle sizes of TiO₂ anatase vs Na/Na⁺ cycling at c/10. The almost linear decrease in voltage for all three particle sizes is consistent with previous studies on Na storage in nanostructured TiO₂ anatase.^{25,26} The continued decrease in voltage appears to be a common feature in several negative Na-ion electrode materials, such as Na₂Ti₆O₁₃,¹⁸ Na₄Ti₅O₁₂,²⁹ amorphous TiO₂,²⁴ and carbon¹³. Both a solid solution reaction, as observed in Na₂Ti₆O₁₃¹⁸ and capacitive storage, as observed for hard carbons¹³, may explain this voltage behavior. It suggests that Na insertion in TiO₂ anatase does not cause the first order phase transition that is well known to occur upon Li insertion

^{30,31}. The most striking difference in the electrochemistry between the different particle sizes is the evolution of the specific capacities upon cycling, as shown in Figure 6.2d. The largest TiO₂ anatase particles (130 nm) achieve the lowest reversible capacity, 42 mAh/g, while it shows the best capacity retention, amounting more than 98% of the initial charge capacity after 25 cycles. The smallest TiO₂ particles (7 nm) exhibit a much higher initial reversible capacity, 170 mAh/g, during the first five cycles, however, decreasing dramatically to 58% after 25 cycles. A previous study about the influence of the electrolyte on the electrochemical behavior suggested that an EC:PC mixture is able to offer better cycling stability³²⁻³⁴. This is apparently because a more stable SEI can be formed in the EC:PC electrolyte as deduced from the electrochemical impedance spectroscopy study³³. Hence, 7nm TiO₂ particles are also tested in this electrolyte. The result shows that the capacity stability for the cell employing the EC:PC electrolyte is distinctly better than the cell with the pure PC electrolyte, but the reversible capacity is slightly lower, especially the first few cycles(see figure 6.2 d and e).

Ex-situ X-ray diffraction patterns on the pristine electrodes and the electrodes reduced to 0 V after 25 cycles are shown for the different particle sizes in Figure 6.3. For 130 nm and 40 nm particles, before and after cycling, the reflections hardly shift, whereas the anatase reflections of the 7 nm particles are significantly depressed after cycling. In addition, the intensities (compared to the background) of the main reflections of TiO₂ anatase significantly decrease after 25th discharge, especially for 130nm and 7nm particles. The lattice parameters and the domain sizes of the different particle sizes resulting from Rietveld refinement of the X-ray diffraction patterns collected at the end of the 25th discharge (Sodiated state, assuming all broadening is due to size broadening) are given in Table 1. Assuming the Na-ions intercalate, potentially via a solid solution reaction, the considerable reversible capacity in combination with the large ionic size of Na-ions is expected to lead to larger changes in unit cell parameters. In contrast, only very small changes in lattice parameters are observed in the XRD fitting results. This finding has a good agreement with the structural changes on anatase nanorod TiO₂ at the first cycle sodiation and desodiation³⁵. The magnitudes of variation on cell volumes and crystalline size in 7nm particles is much larger than 40nm and 130nm particles. In addition, a noticeable decrease on domain sizes of TiO₂ anatase is also shown in Table 1. Further structural characterizations with better resolution (like XPS, TEM) are required to study the interface reaction and sodium insertion mechanism.

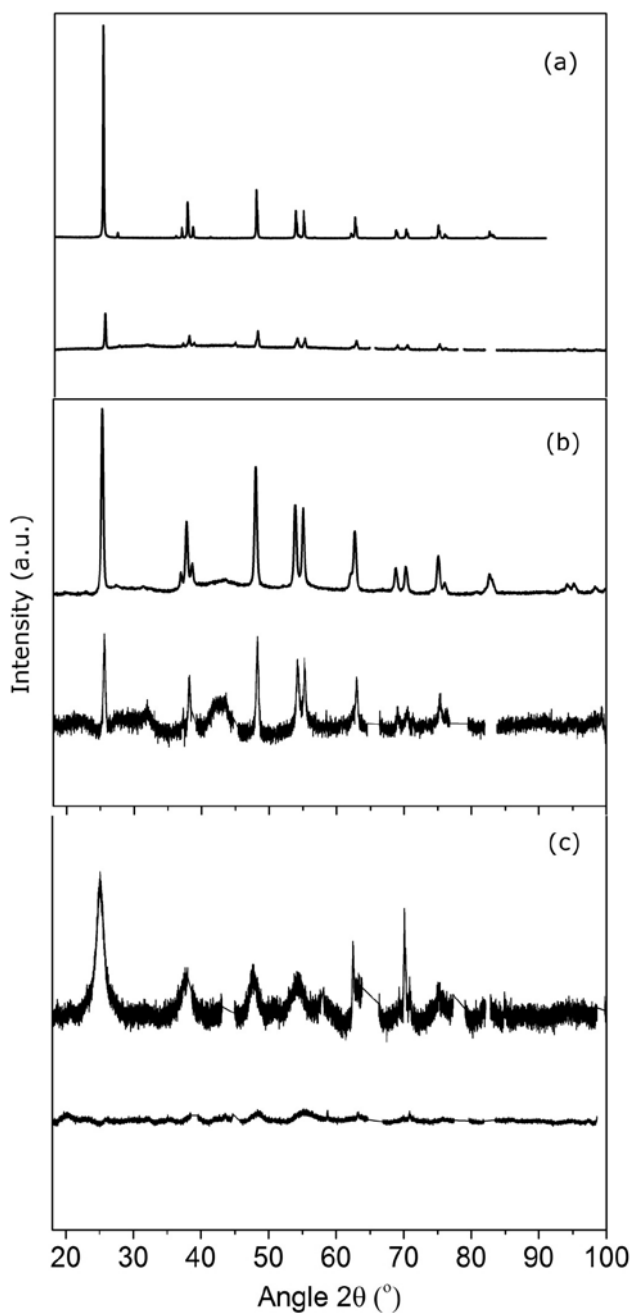


Figure 6.3. Ex-situ X-ray diffraction patterns of the pristine electrodes and the electrodes reduced to 0V after 25 cycles. Pristine particle sizes (a) 130 nm, (b) 40 nm, (c) 7 nm.

Table 1. Lattice parameters and domain size determined from Rietveld refinement for the pristine electrodes and the electrodes that were reduced to 0V after 25 cycles

materials	pristine			25 th discharged			Volume change	domain size change
	a [Å]	c [Å]	domain size [nm]	a [Å]	c [Å]	domain size [nm]		
130 nm	3.785	9.514	130	3.798	9.538	67.69	0.93%	50.7%
40 nm	3.787	9.516	38.1	3.801	9.515	36.1	0.76%	5.25%
7 nm	3.781	9.395	7.12	3.826	9.411	2.67	2.59%	62.5%

To investigate the thermodynamics of Na-ion insertion in anatase TiO₂ Density Functional Theory simulations were performed for the different Na-ion compositions within the unit cell. Quantum chemical calculations have indicated that like Li-ions, Na-ions occupy interstitial octahedral positions²⁷. At present the ground state structures at different Na compositions are identified by evaluating the formation energies (see figure 6.5) of all possible Na configurations over the octahedral interstitial sites in Na_xTiO₂ unit cell the results of which are shown in Figure 6.4. The only stable ground state structure is at x=0.5, with a formation energy of 5.56 meV only slightly more stable than a combination of the TiO₂ and NaTiO₂ end members. This may suggest that similar to Li_xTiO₂^{36,37} the Na_{0.5}TiO₂ is relative stable, displaying two first order phase transitions, between TiO₂ and Na_{0.5}TiO₂ and between Na_{0.5}TiO₂ and NaTiO₂. However, many more Na-ion configurations, in super cells of Na_xTiO₂ are required to establish this. Nevertheless, these calculations do give first insight in the thermodynamics and the structural changes of TiO₂ upon Na-ion insertion.

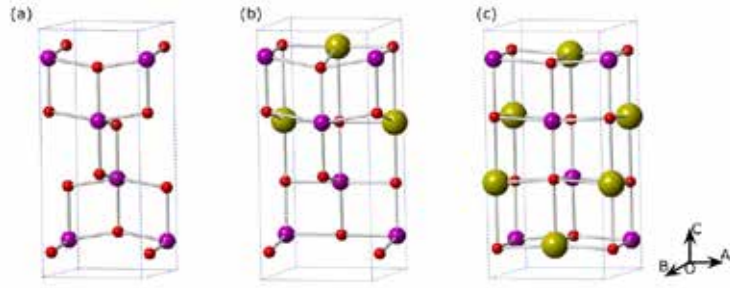


Figure 6.4. Ground state structures of (a) TiO_2 , (b) $\text{Na}_{0.5}\text{TiO}_2$ and (c) NaTiO_2 . Purple: Titanium, red: Oxygen, yellow: Sodium.

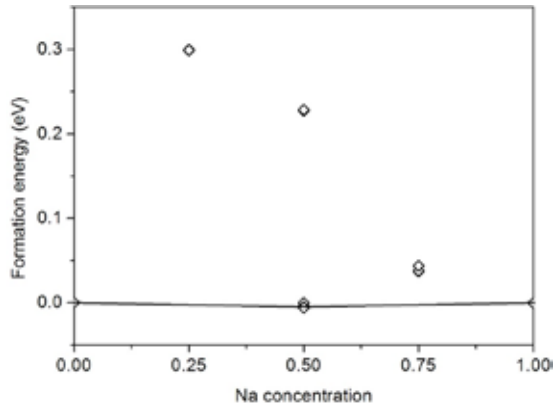


Figure 6.5 The formation energies of the different Na-ion configurations over the octahedral sites in the TiO_2 unit cell calculated by DFT.

Based on the ground state energies the average intercalation voltages between TiO_2 and $\text{Na}_{0.5}\text{TiO}_2$ and between $\text{Na}_{0.5}\text{TiO}_2$ and NaTiO_2 can be estimated³⁸:

$$V(x) = -\frac{E_{\text{Na}_x\text{TiO}_2} - E_{\text{TiO}_2} - x \cdot E_{\text{Na}}}{x \cdot e} \quad \text{Equation 6.1}$$

Where $E_{Na_xTiO_2}$, E_{TiO_2} and E_{Na} are the DFT calculated total energy of Na_xTiO_2 , TiO_2 and Na metal respectively. The result, referenced versus Na/Na^+ , is shown in Figure 6.6, indicating that thermodynamically Na-ion insertion can occur at a positive insertion potential (vs Na/Na^+) from $x = 0$ to $x = 1$ in Na_xTiO_2 . Therefore, the DFT energy calculations indicate that the Na storage in TiO_2 anatase is possible up to Na_1TiO_2 (334mAh/g). However, this theoretical capacity, and close to constant insertion voltage, are not observed applying galvanostatic (dis)charging as shown in Figure 6.2.

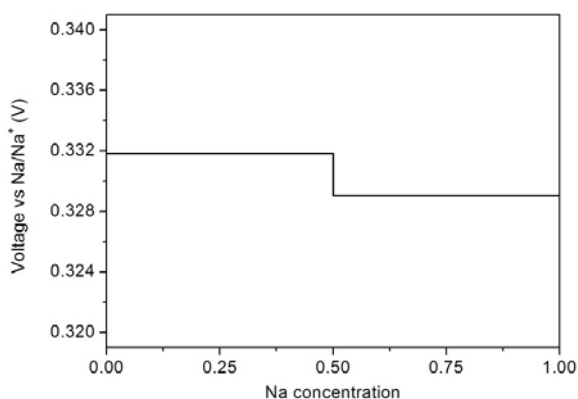


Figure 6.6 The calculated voltage profile based on the ground state energies as a function of sodium composition for Na_xTiO_2 .

In addition DFT predicts that the Na-ion insertion in TiO_2 leads to significant changes in lattice parameters (DV=10.08% TiO_2 to $Na_{0.5}TiO_2$), not reflected by the ex-situ XRD results, see Table 1. In fact, there appears to be no experimental proof that a significant concentration of Na-ions is inserted into the TiO_2 anatase lattice. This would imply that the electrochemical capacities, Figure 6.2, are solely due to storage of Na near the crystallite surface, and leading to X-ray amorphous surface area's on a reduced crystalline anatase core. Na insertion in the crystalline anatase core is further kinetically hindered by high diffusion barriers, in contrast with quantum chemical calculations that suggest that the diffusion barriers for Na-ions in anatase TiO_2 are comparable to that of Li-ions.²⁷

To investigate the kinetic properties of Na ions in bulk anatase, the nudged elastic band calculations, as implemented in VASP, are applied to calculate the energy barriers for Na diffusion in the dilute Na_xTiO_2 anatase structure. Based on the assumption that Na ions occupy the same octahedral sites as lithium ions, all the available Na interstitial sites and all Na ion hops between the adjacent octahedral sites are symmetrically equivalent. Similar to lithium diffusion in anatase TiO_2 , the strong electrostatic repulsion between sodium and the adjacent Ti force Na to travel through the shared octahedron edges.³⁹ In the $2 \times 2 \times 1$ ($axbxc$) supercell the two Na-O6 octahedrons suffer distinct distortion to allow the Na hops between the two adjacent octahedral sites, the shared edge of which varies between 3.56 Å to 4.02 Å (see Figure 6.7). This distortion causes the energy barrier upon Na diffusion shown in Figure 6.8. The large energy barrier for Na-ion diffusion compared to Li-ion diffusion^{39,40} indicates that Na-ion diffusion in $\text{Na}_{0.0625}\text{TiO}_2$ is kinetically hindered at room temperature, consistent with the experimental results that show no evidence for Na-ion insertion. Apparently, the high capacity, close to 170mAh/g, in the smallest particle size (7 nm) is due to a surface storage mechanism.

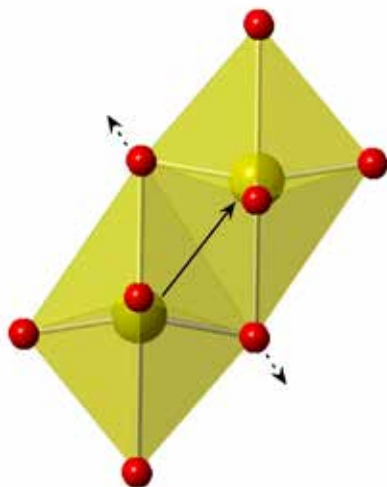


Figure 6.7 Schematic of the Na-O6 octahedra. Yellow atoms are sodium, and red atoms are oxygen.

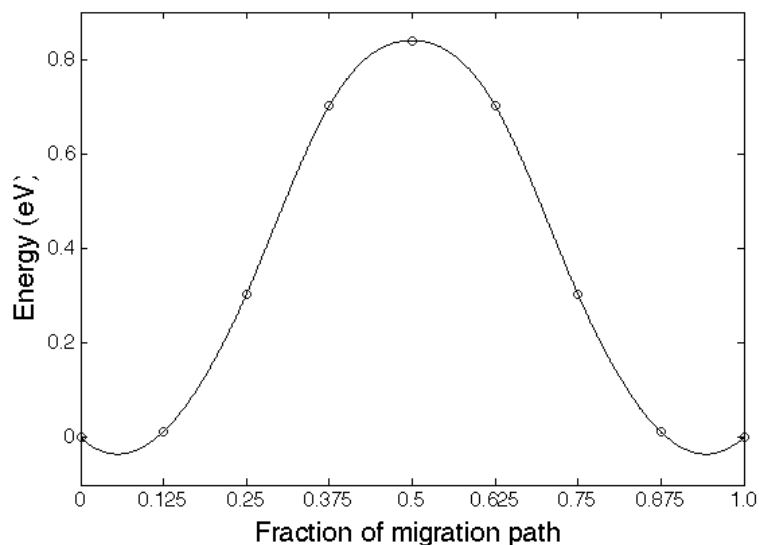


Figure 6.8 The energy barrier for Na-ion diffusion between neighboring octahedral positions in dilute Na_xTiO_2 ($\text{Na}_{0.0625}\text{TiO}_2$) calculated from Nudged Elastic Band calculations in a $2 \times 2 \times 1$ (axbxc) unit cell.

The only significant structural change observed by X-ray diffraction is the broadening of the TiO_2 reflections after 25 cycles as shown in Table 1. The potential origin for this is strain broadening or effective reduction of the crystalline domain size, induced by the loss of crystallinity of the outer shells of the TiO_2 anatase particles. Because the lattice parameters hardly change, which should happen upon Na-ion insertion as indicated by DFT, the broadening is most likely due to such partial loss of crystallinity. Furthermore, such crystallinity loss results in the loss of intensities of the anatase TiO_2 reflection proportional with the third power of the remaining observed crystalline domain size, which is excellent consistent with the observations in figure 6.3 for 130nm and 7nm particles. As the capacity increases with decreasing particle size, and Na-ion insertion is excluded, we suggest that the loss of crystallinity occurs at the surface of the particles due to large distortions initiated by the Na-

ion storage at the surface, although further structural characterizations with better resolution (like XPS, TEM) are required to further investigate this.

Partial loss of crystallinity indicates large structural changes at the surface which may also be the origin of the capacity fading that is much larger for smaller particles, as observed in Figure 6.2d. Another origin for the capacity fading may be electrolyte decomposition at the electrode electrolyte interface, which in lithium ion batteries is well known to result in the formation of a Solid Electrolyte Interface (SEI). This has been observed for hard carbon cycled to 0 V vs Na/Na⁺.^{13,41} In chapter 5, a continuous growing SEI by NaClO₄-PC electrolyte decomposition is suggested to be the main reason for the observed capacity fading in Na₂Ti₆O₁₃. Electrochemical study in this chapter exhibits that better cycling capacity stability can be obtained by employing the EC:PC mixture as electrolyte solvent than employing NaClO₄-PC electrolyte, because for negative Na-ion battery electrodes the mixture of EC and PC results in more stable SEI formation compared to PC.³³

The NEB calculation of the Na-ion energy barrier of diffusion indicates that poor kinetics of the Na insertion in TiO₂ anatase may be a main factor that is preventing the energetically achievable capacity of bulk TiO₂ to be useable, if it would be structurally stable. Although carbon coating and nanoarchitecturing are two powerful strategies to facilitate the kinetics of electrode materials in general, it is questionable whether this can compensate for the high intrinsic barrier for Na-ion diffusion through the anatase TiO₂ lattice. Nevertheless, a recent study reports carbon coated TiO₂ anatase nanorods demonstrating higher rate capacities for sodium ions insertion.²⁶ Another possibility to improve the reaction kinetics of TiO₂ by synthesis of materials with a higher surface area having more reactive surface facets. In this way the kinetics of lithium insertion in TiO₂ anatase were significantly enhanced by synthesis of crystalline anatase having a large fraction of {001} reactive facets.⁴²

6.4 Conclusions

Na-ion electrochemistry of anatase TiO_2 strongly depends on particle size. Particle size reduction leads to distinct increase in the reversible capacity at the expense of the cycling stability. 7 nm TiO_2 anatase particles exhibit the initially highest specific reversible capacity of 170 mAh/g reported for a transition metal oxide negative Na-ion battery electrode. DFT calculations predict that thermodynamically the theoretical capacity associated with the NaTiO_2 composition, 334 mAh/g, can be reached at approximately 0.3 V vs Na/Na^+ . However, structural characterization by XRD of reduced electrodes suggests that Na ions do not intercalate in the bulk TiO_2 anatase lattice, but instead appear to react at the surface of the particles, leading to a loss of crystallinity. Such surface reconstruction reaction is consistent with the increasing capacity with decreasing particle size. The absence of capacity based on bulk Na-ion insertion is suggested to be the consequence of the relatively high activation barrier for the Na ion diffusion through the TiO_2 anatase lattice as predicted by NEB calculations. Therefore, improvement of the reversible Na-ion capacity in anatase TiO_2 should focus on the stability of the surface and SEI formation.

References

- (1) Whittingham, M. S. *Progress in Solid State Chemistry* **1978**, *12*, 44–99.
- (2) Nagelberg, A. S.; Worrell, W. L. *Journal of Solid State Chemistry* **1979**, *29*, 345–354.
- (3) Molenda, J.; Delmas, C.; Hagenmuller, P. *Solid State Ionics* **1983**, *9&10*, 431–436.
- (4) Delmas, C.; Braconnier, J.-J.; Fouassier, C.; Hagenmuller, P. *Solid State Ionics* **1981**, *3-4*, 165–169.
- (5) Tarascon, J. M.; Hull, G. W. *Solid State Ionics* **1986**, *22*, 85–96.
- (6) Abraham, K. M. *Solid State Ionics* **1982**, *7*, 199–212.
- (7) Chevrier, V. L.; Ceder, G. *Journal of the Electrochemical Society* **2011**, *158*, A1011–A1014.
- (8) Palomares, V.; Serras, P.; Villaluenga, I.; Hueso, K. B.; Carretero-González, J.; Rojo, T. O. F. *Energy & Environmental Science* **2012**, *5*, 5884–5901.
- (9) Ong, S. P.; Chevrier, V. L.; Hautier, G.; Jain, A.; Moore, C.; Kim, S.; Ma, X.; Ceder, G. *Energy & Environmental Science* **2011**, *4*, 3680–3688.
- (10) Alcántara, R.; Jiménez-Mateos, J. M.; Lavela, P.; Tirado, J. L. *Electrochemistry Communications* **2001**, *3*, 639–642.
- (11) Stevens, D. A.; Dahn, J. R. *Journal of the Electrochemical Society* **2000**, *147*, 1271–1273.
- (12) Wenzel, S.; Hara, T.; Janek, J. U. R.; Adelhelm, P. *Energy & Environmental Science* **2011**, *4*, 3342–3345.
- (13) Komaba, S.; Murata, W.; Ishikawa, T.; Yabuuchi, N.; Ozeki, T.; Nakayama, T.; Ogata, A.; Gotoh, K.; Fujiwara, K. *Advanced Functional Materials* **2011**, *21*, 3859–3867.
- (14) Cabana, J.; Monconduit, L.; Larcher, D.; Palacin, M. R. *Advanced Materials* **2010**, *22*, E170–E192.
- (15) Didier, C.; Guignard, M.; Denage, C.; Szajwaj, O.; Ito, S.; Saadoune, I.; Darriet, J.; Delmas, C. *Electrochemical and Solid State Letters* **2011**, *14*, A75–A78.
- (16) Hamani, D.; Ati, M.; Tarascon, J.-M.; Rozier, P. *Electrochemistry Communications* **2011**, *13*, 938–941.
- (17) Senguttuvan, P.; Rouse, G.; Seznec, V.; Tarascon, J.-M.; Palacin, M. R. *Chem. Mater.* **2011**, *23*, 4109–4111.

- (18) Rudola, A.; Saravanan, K.; Devaraj, S.; Gong, H.; Balaya, P. *Chemical communications (Cambridge, England)* **2013**, 49, 7451–7453.
- (19) Bonino, F.; Busani, L.; Lazzari, M.; Manstretta, M.; Rivolta, B.; Scrosati, B. *Journal of power sources* **1981**, 6, 261–270.
- (20) Cava, R. J.; Murphy, D. W.; Zahurak, S.; Santoro, A.; Roth, R. S. *J. Solid State Chem.* **1984**, 53, 64–75.
- (21) Jamnik, J.; MAIER, J. *Phys. Chem. Chem. Phys.* **2003**, 5, 5215–5220.
- (22) Deng, D.; Kim, M. G.; Lee, J. Y.; Cho, J. *Energy & Environmental Science* **2009**, 2, 818–837.
- (23) Wagemaker, M.; Kearley, G. J.; Van Well, A. A.; Mutka, H.; Mulder, F. M. *J. AM. Chem. Soc.* **2003**, 125, 840–848.
- (24) Xiong, H.; Slater, M. D.; Balasubramanian, M.; Johnson, C. S.; Rajh, T. *The Journal of Physical Chemistry Letters* **2011**, 2, 2560–2565.
- (25) Xu, Y.; Memarzadeh Lotfabad, E.; Wang, H.; Farbod, B.; Xu, Z.; Kohandehghan, A.; Mitlin, D. *Chemical communications (Cambridge, England)* **2013**, 49, 8973–8975.
- (26).
- (27) Lunell, S.; Stashans, A.; Ojamae, L.; Lindstrom, H.; Hagfeldt, A. *J. AM. Chem. Soc.* **1997**, 119, 7374–7380.
- (28) Borghols, W. J. H.; Lu tzenkirchen-Hecht, D.; Haake, U.; van Eck, E. R. H.; Mulder, F. M.; Wagemaker, M. *Physical chemistry chemical physics : PCCP* **2009**, 11, 5742.
- (29) Woo, S. H.; Park, Y.; Choi, Y.; Choi, N.-S.; Nam, S.; Tae, K. *J. Electrochem. Soc.* **2012**, 200, A2016–A2023.
- (30) Tarascon, J. M.; Poizot, P.; Laruelle, S.; Grugeon, S.; Dupont, L. *Nature* **2000**, 407, 496–499.
- (31) Tarascon, J. M.; Armand, M. *Nature* **2001**, 414, 359–367.
- (32) Wu, L.; Buchholz, D.; Bresser, D.; Gomes Chagas, L.; Passerini, S. *Journal of power sources* **2014**, 251, 379–385.
- (33) Ponrouch, A.; Marchante, E.; Courty, M.; Tarascon, J.-M.; Palacin, M. R. *Energy & Environmental Science* **2012**, 5, 8572–8583.
- (34) Ponrouch, A.; Dedryvère, R.; Monti, D.; Demet, A. E.; Ateba Mba, J. M.; Croguennec, L.; Masquelier, C.; Johansson, P.; Palacin, M. R. *Energy & Environmental Science* **2013**, 6, 2361.
- (35) Kim, K.-T.; Ali, G.; Chung, K. Y.; Yoon, C. S.; Yashiro, H.; Sun, Y.-K.; Lu, J.; Amine, K.; Myung, S.-T. *Nano Letters* **2014**, 14, 416–422.

- (36) Macklin, W. J.; Neat, R. J. *Solid State Ionics* **1992**, 53-56, 694-700.
- (37) Wagemaker, M.; Borghols, W. J. H.; Mulder, F. M. *Journal of the American Chemical Society* **2007**, 129, 4323-4327.
- (38) Aydinol, M. K.; Kohan, A. F.; Ceder, G.; Cho, K. *Physical Review B* **1997**, 56, 1354-1365.
- (39) Belak, A. A.; Wang, Y.; Van der Ven, A. *Chemistry of Materials* **2012**, 24, 2894-2898.
- (40) Morgan, D.; Van der Ven, A.; Ceder, G. *Electrochemical and Solid State Letters* **2004**, 7, A30-A32.
- (41) Gotoh, K.; Ishikawa, T.; Shimadzu, S.; Yabuuchi, N.; Komaba, S.; Takeda, K.; Goto, A.; Deguchi, K.; Ohki, S.; Hashi, K.; Shimizu, T.; Ishida, H. *Journal of power sources* **2013**, 225, 137-140.
- (42) Sun, C. H.; Yang, X. H.; Chen, J. S.; Li, Z.; Lou, X. W.; Li, C.; Smith, S. C.; Lu, G. Q. M.; Yang, H. G. *Chemical communications (Cambridge, England)* **2010**, 46, 6129-6131.

Summary

Nanostructured materials are featured by providing a variety of favourable electrical properties, as the reduced ion and electron transport paths enable significant enhancement on (de)intercalation rates and hence high power. For TiO_2 anatase, nano-sizing results in a curved open cell voltage profile with a much shorter plateau region in comparison with that of micron sized materials. The main objective of this thesis is to gain insight in the impact of particle size on the Li-ion storage and Na-ion storage in anatase TiO_2 using a combined experimental, theoretical approach. In addition a novel Na-ion titanium oxide storage compound is tested and characterized.

Nanostructuring has a striking influence on the thermodynamics and kinetics of Li-ion insertion reactions in anatase TiO_2 . The particle size dependent phase transformations in anatase TiO_2 upon lithiation are systematically studied. The equilibrium voltage measured by galvanostatic intermittent titration technique decreases progressively with particle size reduction, which is attributed to the difference in surface energy of the pristine and lithiated phases. Based on the evolution of domain size and phase fraction of the two phases, it is concluded that the first-order phase transition proceeds by continuous nucleation upon lithium insertion. For all particle sizes the phase boundary is found to migrate under non-equilibrium conditions even under very slow

(dis)charge conditions. Remarkably, the degree of non-equilibrium condition increases with particle size decreasing, which is rationalized by the difference in the observed phase transition behaviour between small and large particles. The absence of phase coexistence in smaller particles in combination with the sluggish ionic transport rationalizes the better electrochemical performance of the nano-structured anatase TiO_2 as compared to the micro sized material. These results suggest a very low nucleation barrier for the formation of new phases and a sluggish ionic migration during phase boundary movement. Therefore strategies to improve the rate performance of nano structured anatase TiO_2 should concentrate on improving the interstitial diffusion, for instance by appropriate doping with Nb or Zn.

Based on the experimental study on the particle size dependent phase transition behaviour, the impact of particle size and surface orientation on the lithium ion insertion in anatase TiO_2 is systematically investigated by using DFT first-principles calculations and surface cluster expansion. Nano-sized TiO_2 is modelled by surface slabs with two thermodynamically stable orientations $\{101\}$ and $\{001\}$. The calculated formation energies for bulk and surface structures suggest that the stable Li configuration of $\text{Li}_{0.5}\text{TiO}_2$ titanate phase depends on the surface orientation. For the Li composition below $\text{Li}_{0.5}\text{TiO}_2$, the calculated size dependent voltage curves are in qualitative agreement with the experimental results. The calculations show that the voltage difference between the different surface orientations is due to the different Li-O and Ti-O bond length in the surface region. For the Li composition above $\text{Li}_{0.5}\text{TiO}_2$, the relative magnitudes of the voltage profiles between different surface directions and particle sizes are not consistent with the experimental observations. This is suggested to be the consequence of the stoichiometric surface slabs. A surface excess of oxygen is

shown to explain the larger intercalation voltages in smaller particles with the composition above $\text{Li}_{0.5}\text{TiO}_2$.

The demand for renewable energy resources has initiated the search for high performance and cost effective battery systems. Na-ion as a charge carrier is one of the most promising alternatives to Li-ions due to its high abundance, low cost, and comparable high cell potential. Rudola et al. explored Na-ion storage in a novel compound $\text{Na}_2\text{Ti}_6\text{O}_{13}$, demonstrating a reversibly uptake of 1 Na ion per formula unit (49.5 mAh/g) by a solid solution mechanism at an average potential of 0.8 V. In this thesis it is shown that by lowering the cut-off voltage from 0.3 V to 0 V vs Na/Na⁺ the capacity of the layered $\text{Na}_2\text{Ti}_6\text{O}_{13}$ negative electrode material can be enhanced from 49.5 mAh/g ($\text{Na}_{2+1}\text{Ti}_6\text{O}_{13}$) to a promising 196 mAh/g ($\text{Na}_{2+4}\text{Ti}_6\text{O}_{13}$) for at least 10 cycles, after which it gradually reduces. To understand the structural changes in-situ X-ray diffraction is performed and compared with Density Functional Theory calculations. A consistent evolution of the lattice parameters and Na-ion positions is observed. The results show that Na-ion intercalation in the $\text{Na}_{2+x}\text{Ti}_6\text{O}_{13}$ host structure is limited to $\text{Na}_{2+2}\text{Ti}_6\text{O}_{13}$ in a solid solution reaction. Only small changes in lattice parameters indicate that the insertion reaction is highly reversible. Further increasing the Na composition below 0.3 V appears to lead to loss in crystallinity, which in combination with solid electrolyte interface formation is suggested to be the origin of the gradually reducing reversible capacity.

The promising Li-ion storage properties of TiO_2 anatase provide the motivation to embark on the study of Na-ion insertion in anatase TiO_2 . Electrochemical and X-ray experiments and DFT calculations are performed to improve the understanding about

the particle size dependent electrochemical Na-ion storage in the TiO_2 anatase. Reducing the particle size results in a distinct increase of the reversible capacity, also introducing stronger degradation of the cycling stability. The highest specific reversible capacity (210mAh/g) was found for 7 nm TiO_2 anatase, which is among the largest reported in literature. Although bulk storage is generally assumed, X-ray diffraction on the electrodes after discharge and charge shows negligible changes on the lattice parameters, indicating that Na-ion insertion in the TiO_2 lattice does not occur significantly. Nevertheless DFT calculation predicts that the fully occupied Na_1TiO_2 (capacity 334mAh/g) can be thermodynamically achieved at a positive voltage (0.3V). The fact that Na-ion insertion does not occur is most likely due to the large energy barrier for Na-ion diffusion which is calculated to be $\sim 0.84\text{eV}$ at the dilute limit. These results indicate that the inserted sodium ions are mainly accommodated at the surface region. Therefore strategies to improve the electrochemical performance of Na storage by TiO_2 anatase should focus on improving the surface and electrolyte stability.

Samenvatting

Materialen met een nanostructuur kenmerken zich door een verscheidenheid aan gunstige elektrische eigenschappen, zoals de kortere transportpaden voor ionen en elektronen die een significante toename van de (de)intercalatiesnelheden toelaten en daarmee een groot elektrisch vermogen. Voor TiO_2 in de anatase vorm, resulteren nano-afmetingen in een gebogen open-cel spanningsprofiel met een veel korter plateau in vergelijking tot dat van materialen van microafmeting. Het hoofddoel van dit proefschrift is het verwerven van inzicht in de invloed, die de grootte van de deeltjes heeft op de opslag van Li-ionen en Na-ionen in anatase TiO_2 met een aanpak die bestaat uit een combinatie van experimentele en theoretische methoden. Bovendien is een nieuw titaniumoxide materiaal voor opslag van Na-ionen getest en gekarakteriseerd.

Nanostructurering heeft een frappante invloed op de thermodynamica en kinetica van Li-ion insertiereacties in anatase TiO_2 . De deeltjesgrootte afhankelijke faseveranderingen in anatase TiO_2 na lithiëring zijn systematisch bestudeerd. Het evenwichtsvoltage gemeten met een galvanostatische intermitterende titratietechniek neemt progressief af met de verkleining van de deeltjesgrootte, wat wordt toegeschreven aan het verschil in oppervlakte-energie tussen de maagdelijke en de gelithieerde fase. Op grond van de evolutie van domeingrootte en fasefractie van de

twee fasen, wordt geconcludeerd dat de eerste-orde faseovergang zich voltrekt door continue nucleatie na lithiumopname. Voor alle deeltjesgrootten wordt gevonden dat de fasegrens migreert onder niet-evenwicht condities zelfs bij zeer trage (ont)ladingscondities. Opmerkelijk is dat de mate van niet-evenwicht toeneemt als de deeltjesgrootte afneemt, wat begrepen kan worden uit het verschil in het waargenomen faseovergangsgedrag tussen kleine en grote deeltjes. De afwezigheid van fase-coexistentie in kleinere deeltjes in combinatie met het trage ionentransport verklaart de betere elektrochemische prestatie van anatase TiO_2 met nanostructuur in vergelijking tot het materiaal op microgrootte. Deze resultaten suggereren een zeer lage nucleatiedrempel voor de vorming van nieuwe fasen en een trage ionenmigratie gedurende de beweging van de fasegrens. Daarom zouden strategieën om de snelheidsprestatie van anatase TiO_2 met nanostructuur te verbeteren zich moeten concentreren op het verbeteren van de interstitiële diffusie, bij voorbeeld door geschikte doping met Nb of Zn.

Op basis van de experimentele studie van de afhankelijkheid van deeltjesgrootte voor het faseovergangsgedrag, is de invloed van deeltjesgrootte en oppervlakte-oriëntatie op de lithium-ion insertie in anatase TiO_2 systematisch onderzocht met DFT first-principles berekeningen en oppervlakte clusterexpansie. TiO_2 van nano-afmetingen is gemodelleerd met oppervlaktelagen met twee thermodynamisch stabiele oriëntaties $\{101\}$ en $\{001\}$. De berekende vormingsenergieën voor bulk en oppervlaktestructuren suggereren dat de stabiele Li configuratie van de $\text{Li}_{0.5}\text{TiO}_2$ titanaatfase afhangt van de oppervlakteoriëntatie. Als het Li gehalte beneden dat van $\text{Li}_{0.5}\text{TiO}_2$ ligt, komen de berekende grootteafhankelijke spanningskrommen kwalitatief overeen met de experimentele resultaten. De berekeningen tonen aan dat het spanningsverschil tussen

de verschillende oppervlakteoriëntaties te danken is aan de verschillen in Li-O en Ti-O bindingslengte nabij het oppervlak. Voor het Li gehalte boven dat van $\text{Li}_{0.5}\text{TiO}_2$, zijn de relatieve grootten van de spanningsprofielen tussen verschillende oppervlakterichtingen en deeltjesgrootten niet consistent met de experimentele waarnemingen. Dit wordt verondersteld het gevolg te zijn van de stoichiometrische oppervlaklagen. Een verhoogde concentratie van zuurstof aan het oppervlak verklaart de grotere intercalatievoltages in kleinere deeltjes met het gehalte boven dat van $\text{Li}_{0.5}\text{TiO}_2$.

De vraag naar bronnen van hernieuwbare energie en energieopslag heeft de aanzet gegeven voor de zoektocht naar hoog presterende kosteneffectieve batterijsystemen. Het Na-ion als ladingsdrager is een van de meest belovende alternatieven voor Li-ionen dankzij zijn hoge abundantie, lage kosten, en vergelijkbaar hoge cel potentiaal. Rudola et al. onderzochten de opslag van Na-ionen in een nieuwe stof $\text{Na}_2\text{Ti}_6\text{O}_{13}$, waarbij zij een reversibele opname aantoonden van 1 Na ion per formule eenheid (49,5 mAh/g) via een mechanisme van oplossing in de vaste stof bij een gemiddelde potentiaal van 0,8 V. In dit proefschrift wordt aangetoond dat door het afsnijdingsvoltage te verlagen van 0,3 V naar 0 V vs Na/Na⁺ de capaciteit van het gelaagde $\text{Na}_2\text{Ti}_6\text{O}_{13}$ materiaal voor de negatieve electrode verhoogd kan worden van 49,5 mAh/g ($\text{Na}_{2+1}\text{Ti}_6\text{O}_{13}$) tot een veelbelovend 196 mAh/g ($\text{Na}_{2+4}\text{Ti}_6\text{O}_{13}$) gedurende tenminste 10 cycli, waarna dit langzaam afneemt. Om de structurele veranderingen te begrijpen is in-situ Röntgenverstrooiing uitgevoerd en de resultaten zijn vergeleken met berekeningen met Density Functional Theory. Een consistente verandering van de roosterparameters en Na-ion posities is waargenomen. De resultaten laten zien dat intercalatie van Na-ionen in de $\text{Na}_{2+x}\text{Ti}_6\text{O}_{13}$ gastheerstructuur beperkt is tot $\text{Na}_{2+2}\text{Ti}_6\text{O}_{13}$.

in een vaste-stof oplossingsreactie. De zeer kleine veranderingen in de roosterparameters wijzen er op dat de insertiereactie in hoge mate reversibel is. Verder verhogen van het Na gehalte beneden 0,3 V lijkt tot een verlies van kristalliniteit te leiden, wat in samenhang met de vorming van het interface tussen vaste-stof en elektrolyt is voorgesteld als oorzaak voor de geleidelijk afnemende reversibele capaciteit.

De veelbelovende opslageigenschappen voor Li-ionen van TiO_2 anatase verschaffen de motivatie om de studie van Na-ion insertie in anatase TiO_2 aan te vangen. Elektrochemische en Röntgen experimenten en DFT berekeningen zijn uitgevoerd om het begrip van de afhankelijkheid van deeltjesgrootte voor de elektrochemische opslag van Na-ionen in TiO_2 anatase te vergroten. Verkleining van de grootte van de deeltjes resulteert in een markante toename van de reversibele capaciteit, waarbij een sterkere vermindering van de stabiliteit onder herhaling van cycli wordt geïntroduceerd. De hoogste specifieke reversibele capaciteit (210 mAh/g) werd gevonden voor 7 nm TiO_2 anatase, wat behoort tot de grootste onder de waarden, die in de literatuur worden gerapporteerd. Hoewel opslag in de bulk algemeen wordt aangenomen, laat Röntgenverstrooiing aan de elektroden na ontlading en lading verwaarloosbaar kleine veranderingen in de roosterparameters zien, wat een aanwijzing is dat Na-ion insertie in het TiO_2 rooster niet significant plaats vindt. Desalniettemin voorspelt berekening met DFT dat het volledig bezette Na_xTiO_2 (capaciteit 334 mAh/g) thermodynamisch bereikt kan worden bij een positief voltage (0,3 V). Het feit dat Na-ion insertie niet plaatsvindt is hoogstwaarschijnlijk te wijten aan de hoge energiebarrière voor Na-ion diffusie die is berekend als $\sim 0,84$ eV in de verdunde limiet. Deze resultaten wijzen er op dat de opgenomen natriumionen hoofdzakelijk ondergebracht worden nabij het

oppervlak. Daarom zouden strategieën om de elektrochemische prestatie van Na opslag door TiO_2 anatase te verhogen zich moeten toespitsen op de verbetering van oppervlak en elektrolyt stabiliteit.

Acknowledgements

In the past 5 years, I have a lot of good memories in Delft.

First of all, I would like to thank my daily supervisor, Dr. Marnix Wagemaker, for his remarkable support and guidance throughout my Ph.D study. Besides you always giving valuable suggestion and encouragements for research, I have been inspired by your vision and rigorous attitude in scientific pursuit. Thank you Marnix!

I would like to express my gratitude to my promotor Prof. Fokko. M. Mulder for stimulating discussion in progress meeting and many helpful advice in experiments.

I am very grateful to people in battery group: Dr. Swapna Ganapathy, Dr. Deepak Singh, Xiaoyu Zhang, Alexandros, Frits Klaver, Chuang Yu. Most of work in this thesis would not be possible without your contributions. Three members in particular, Swapna is very friendly and supportive to me! You always provide indispensable advice and guidance on both calculation and experimental work at the critical stage of my research. I really benefited a lot. Xiaoyu is always very kind to give me help for both research and life. I also would like to acknowledge Alexandros (who joined the group in my last year) for the great contribution in chapter 6.

A special thanks goes to Dr. Jouke Heringa. He was an invaluable resource for his coding expertise. He always gave me a hand when I need help, not only for work, but also for some problems in life. He was also very kind to help me translate the summary and propositions. Thank you very much Jouke!

I would like to thank Michel Steenvoorden, Kees Goubitz, and Anton Lefering for their technical support. I am also grateful to Nicole and Ilse for their constant support and help in the past five years.

I would like to take this opportunity to thank Dr. Peter Klaver for his help in VASP calculation. I am also grateful to Dr. Anton van der Ven for providing us the cluster expansion code and very helpful suggestions.

My sincere acknowledgement also goes to other colleagues in FAME group. This is a wonderful group, and everyone here is always nice and helpful. For my three year officemate, Anca Anastasopol, and Dr. Anna Grzech, the time we spent with is pleasant and memorable. Thank you for creating such nice work atmosphere! And in my last year, Fengjiao, Chuang and Alexander moved in the office, bringing a nice period of hard work and laughter. Thank you guys! I also would like to thank Dr. Zhiqiang Ou, Thang Nguyen, Shasha Zhang, Zhou Zhou, Wenqin Shi, Romain Blonde, Yibole, Bouwer Huang, Lei Ma, Yaolin Xu, Dr. Luana Caron, Xuefei Miao and all other current members and alumni of FAME for making my PhD life fun and interesting.

Special thanks go to Dr. Jie Yang and Dr. Ming Ding, who gave a lot of help and encouragement to me in the life.

Over the past five years, my parents are always there to care my health and encourage whatever I do. Mum and Dad, thank you for your love and support!

Finally I would like to thank my beloved husband, Hao Chen, for always being there with me in all the happy and hard days. Your love, understanding and encouragement are the source of my energy and inspiration forever.

Vancouver, September, 2014

Curriculum Vitae

Kun Shen was born on 20th of February 1984 in Harbin, China. Her family moved to Langfang when she was one. In 2003, She graduated high school in Langfang and entered Central South University, majored in Materials Science and Engineering and minored in Applied Physics. In 2007, she obtained her Bachelor degree with honor. Due to the good performance on her grades, she was admitted to graduate school without entrance examination. She started her Master study in Materials Physics. In June of 2009, she graduated on microstructure and properties study of copper matrix composite. Then she moved to The Netherlands, to start PhD study at the group of Fundamental Aspects of Materials and Energy (FAME) at Delft University of Technology from which this thesis resulted.

